Analysis of Interfacial Processes and Fabrication of Catalytic Electrodes for Hydrogen Evolution Reaction in Water Electrolysis Process

水電解反応における界面反応プロセスの解析と
水素発生反応用触媒電極の形成

February, 2021

Tatsuki FUJIMURA

藤村　樹

Analysis of Interfacial Processes and Fabrication of Catalytic Electrodes for Hydrogen Evolution Reaction in Water Electrolysis Process

水電解反応における界面反応プロセスの解析と
水素発生反応用触媒電極の形成

February, 2021

Waseda University

Graduate School of Advanced Science and Engineering

Department of Advanced Science and Engineering

Research on Applied Chemistry A

Tatsuki FUJIMURA

藤村　樹

Contents

Chapter 1:

General Introduction

1.1. Issues toward the introduction of renewable energy

Renewable energy, such as solar and wind power, is an energy source that is independent on limited resources such as fossil fuels and, thus, causes reduced CO_2 emissions. The use of renewable energy has increased worldwide. In the photovoltaic system, the generation capacity of photovoltaic cells increased from <10 GW in 2012 to ~40 GW in 2016 [1]. The generation capacity of photovoltaics (PV) has annually increased by 30% because of governmental support. The Japanese government also claimed that the target value for the introduction of renewable energy was set to 22–24% in the electric power supply system by 2030 FY in the 5th Strategic Energy Plan enacted in 2018 [2]. Moreover, the use of renewable energy as the primary source of power supply should be increased to >50%.

Despite the critical requirements of society, some potential issues need to be addressed. As renewable energy is intermittent and fluctuating because of its dependence on uncontrollable natural conditions, the power supply is unstable [3,4], which causes a gap between power supply and demand. Moreover, to maintain a stable supply of electricity, an excess amount of renewable energy is sometimes wasted. Thus, additional electricity should be supplied by other processes such as thermal power generation when the electric power supply decreases. To realize renewable energy as the primary source of power supply, processes to efficiently utilize intermittent and fluctuating renewable energy are highly desired.

1.2. Large-scale energy storage process using hydrogen as the energy carrier

A large-scale energy storage process is a promising solution to prevent the unbalanced power supply and efficiently utilize renewable energy. This process controls the unbalanced demand and supply of energy by harvesting excess energy and providing stored energy, for which batteries are promising candidates. Excess energy is harvested as the electrochemical energy for charging and providing the stored energy as a discharging process [5]. This process has advantages such as rapid response and low conversion loss of stored energy. However, storing energy for a longer duration is not suitable [6] because of the self-discharge process. Therefore, an alternative approach suitable for a longer duration is highly required.

The energy storage process in which electric energy is converted to chemical energy by electrochemical reactions and stored as chemical compounds is an alternative to batteries. This produced material is called energy carrier [7]. The storage process using H_2 as an energy carrier is a promising alternative process, as the conversion of chemical to electric energy from H_2 does not emit CO_2 [3,4,7-9]. Hydrogen is widely utilized in industrial processes such as the ammonia synthesis process [8,10] and fuel cell systems widely applied to generate electricity to fuel cell vehicles. Many hydrogen production processes such as steam reforming from fossil fuels [11] and the industrial NaCl electrolysis process are available. Figure 1.1 shows the potential applications of hydrogen and potential processes for hydrogen production.

The use of hydrogen as the energy carrier for large-scale energy storage requires a production process without CO_2 emission. Water electrolysis has been focused as a hydrogen production process for energy carriers because it produces highly pure hydrogen without CO_2 emission [7-10,12]. Furthermore, this process can utilize water, which abundantly exists on the surface, as the reactant.

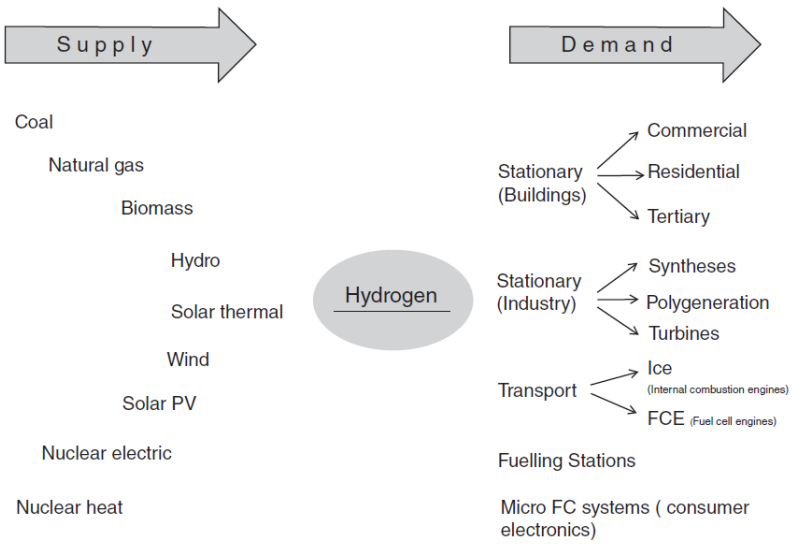

Figure 1.1 Potential hydrogen supply and applications [10] (Hydrogen Storage Technologies: New Materials, Transport and Infrastructure, A. G-Jopek, W. Jehle, J. Wellnitz, Chapter 2 Copyright © (2014) [John Wiley and Sons])

Therefore, a large-scale energy storage process using hydrogen is an alternative and water electrolysis is critical for its realization as a production process of hydrogen.

1.3. Water Electrolysis Processes in Alkaline Conditions

As described in Section 1.2, among the several processes investigated for hydrogen production, water electrolysis is promising because it uses renewable energy. For practical applications, a suitable process should be selected on the basis of the purposes or conditions for utilizing water electrolysis.

For industrial and large-scale energy storage processes, water electrolysis processes that can produce large amounts of hydrogen at lower costs are required [3, 13]. Alkaline (solution) water electrolysis is a candidate because it has a simple system suitable for larger-scale processes and utilizes low-cost materials as electrolyzers [3, 9, 14].

In contrast, a small-size water electrolysis process with higher efficiency and quick response is desired for small-scale energy storage used in small grid or isolated systems [3, 13]. Solid polymer electrolyte water electrolysis such as proton exchange membrane (PEM) water electrolysis, has been widely investigated for their application in water electrolysis because it exhibits high performance and quick response for the intermittent change of power supply [14, 15]. Recently, anion exchange membranes (AEM) have emerged as a new candidate because it can utilize lower-cost materials (compared to PEM water electrolysis) and its use benefits from the advantages of PEM water electrolysis [15-17]. This AEM process is expected to be a next-generation, higher-performance water electrolysis process at a lower cost.

Because of the different purposes, both alkaline and AEM water electrolysis processes are essential for hydrogen production processes using renewable energy, and further improvement is necessary.

In this section, the essential characteristics and issues of the alkaline and AEM water electrolysis processes, mainly focusing on the cathode that directly influences hydrogen evolution, are briefly introduced.

1.3.1. Alkaline (solution) water electrolysis process

1.3.1.1. Basic characteristics

The alkaline water electrolysis process is a historical process for hydrogen production, known for more than 200 years [18], and first demonstrated by Nicholson and Carlisle [19]. A schematic of this process is shown in Figure 1.2.

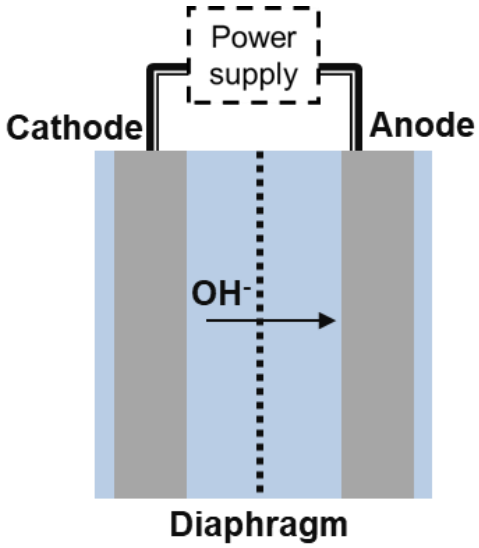

Figure 1.2 Schematic of alkaline water electrolysis process based on [8] (H. A. Miller, K. Bouzek, J. Hnat, S. Loos, C. I. Bernäcker, T. Weißgärber, L. Röntzsch and J. Meier-Haack, Sustainable Energy Fuels, 2020, 4, 2114- Published by The Royal Society of Chemistry.)

In general, an alkaline water electrolysis process is composed of a cathode, an anode, an electrolyte, and a power supply unit, as shown in Figure 1.2. By applying direct current, H_2 is generated on the cathode, and oxygen is generated on the anode. The reactions at the cathode and anode are described in Eqs. (1.1) and (1.2), respectively.

$$\text{Cathode:} \qquad 2H_2O\ 2e^- \rightarrow H_2 + 2OH^- \tag{1.1}$$

$$\text{Anode:} \qquad 4OH^- \rightarrow O_2 + 2H_2O + 4e^- \tag{1.2}$$

The cathode reaction in Eq. (1.1) is called the hydrogen evolution reaction (HER), and the anode reaction in Eq. (1.2) is called the oxygen evolution reaction (OER). As described in Eqs. (1.1) and (1.2), the electrolyte is generally utilized under alkaline solutions because the strongly acidic electrolyte causes severe corrosion, leading to the degradation of electrodes and cell materials [20,21]. A higher concentration of ~30 wt% KOH solution is commonly utilized as the electrolyte for alkaline water electrolysis because of its higher electronic conductivity [8,20]. The diaphragm was also installed to prevent mixing of the hydrogen and oxygen gases and to maintain the insulating conditions of the cathode and anode.

These fundamental characteristics of the alkaline water electrolysis process provide the following advantages: the simplicity of the electrolyzer configuration enables the realization of a large-scale electrolyzer system. Large-scale electrolyzers of >100 MW are commercially available [21], and non-noble-metal-based materials can be used as both the cathode and anode materials [8, 20, 22, 23]. Especially for the cathode, carbon-based materials are paid attention to transition metal-based materials [24]. Therefore, the alkaline water electrolysis process is suitable for large-scale hydrogen production processes.

Nevertheless, the lower efficiency of the process limits its practical applications [8, 14]. To realize large-scale water electrolysis, the efficiency should be improved. Figure 1.3 shows the correlation between the cell voltage and current density [25].

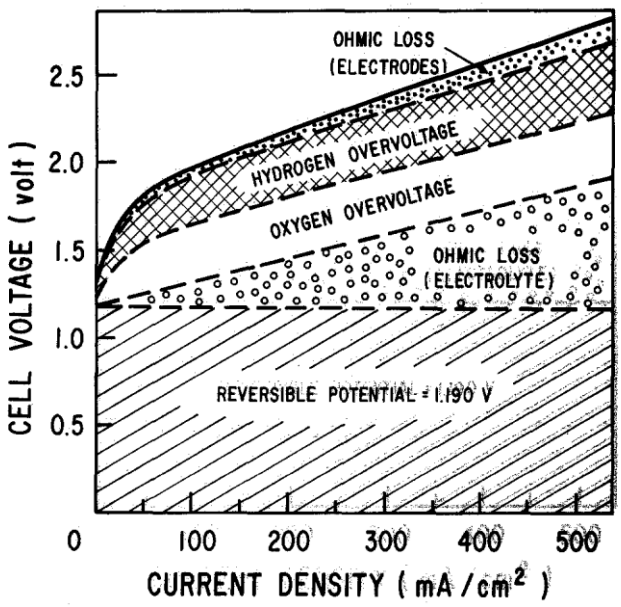

Figure 1.3 Voltage–current performance of an unactivated unipolar electrolyzer [25] (Copyright 1976 by JES. Reproduced with permission of JES. By Copyright Clearance Center's RightsLink® service)

As shown in Figure 1.3, the water electrolysis process requires a larger cell voltage than the theoretical overvoltage (1.23 V at 298 K). To improve the efficiency of the entire process, the voltage of each component shown in Figure 1.3 must be reduced. The voltage derived from the reactions on the cathode (hydrogen overpotential) and the anode (oxygen overpotential) significantly influences the voltage of the entire cell. Therefore, the improvement of the hydrogen and oxygen overpotentials is essential for realizing an efficient process.

1.3.1.2. Issues on HER electrodes

Focusing on the hydrogen potential that directly influences the HER, a larger overpotential is required to proceed with the cathode reaction [25]. The following process can be considered: first, the HER proceeds, and a water molecule is reduced to generate molecular hydrogen. Second, hydrogen bubbles evolve and grow on the electrode surface, eventually detaching from the electrode. Considering this process, two possible

limitations that restrict the achievement of low overpotentials are identified.

The first is the scarcity of catalyst materials with higher HER activity, which reduces the overpotential for the HER. It is well known that Pt is a state-of-the-art catalyst material for the HER [26, 27]. However, the scarcity and expensiveness of Pt limit its large-scale applications. In commercial applications, Ni-based materials are utilized as the cathode [7,8]. They exhibit larger overpotentials because of their lower inherent HER activity. New cathode materials with higher HER activity have been widely investigated [22, 28], such as Ni-Mo-based materials [29].

The other factor is the degradation of the efficiency by bubble behavior during electrolysis. As the reaction proceeds, hydrogen bubbles evolve on the electrode surface. These bubbles become larger and cover the electrode surface, preventing H_2O from accessing the reaction sites for the HER, which leads to an increase in ohmic resistance [9,30, 31]. The bubbles on the surface also contribute to changes in the current distribution in the electrode surface because of the bubbles' insulating characteristics [32]. Furthermore, the bubbles between the cathode and anode contribute to the increase in the resistance between the electrodes. Therefore, controlling the bubble behavior on the electrode surface is critical for reducing the overpotential for the HER, improving the efficiency of the process on the cathode, facilitating the development of new materials with higher HER activity.

Many processes have been investigated and proposed to eliminate the effect of bubbles. These processes are mainly categorized into two different approaches: (i) introduction of an external field and (ii) modification of the surface nano/microstructures on the electrode surface. Examples of bubble effect control are briefly introduced as follows.

(i) Bubble behavior control by introduction of the external environment

The purpose of introducing the external environment is to quickly remove the bubbles from the electrode surface, which enables the suppression of the ohmic voltage drop, reduction of the resistance between the cathode and the anodes, and improvement of mass transfer to the electrode surface [33, 34]. Several factors, such as the electrolyte flow, magnetic field, and ultrasonic field, have been employed as external environments

to enhance bubble behaviors.

Electrolyte flow

The use of a circulating electrolyte for introduction of electrolyte flow is one of the most common processes to introduce an external field and is utilized in the commercial water electrolysis process [34]. The circulating electrolyte enhances bubble detachment. J. Eigeldinger et al. demonstrated that the introduction of the electrolyte flow improved the bubble coverage on the electrode surface, which was 10 times lower than that in stagnant flow during electrolysis [35]. D. Zhang et al. also observed that the circulation of the electrolyte decreased the diameter of bubbles departing from the electrode, as shown in Figure 1.4 [36].

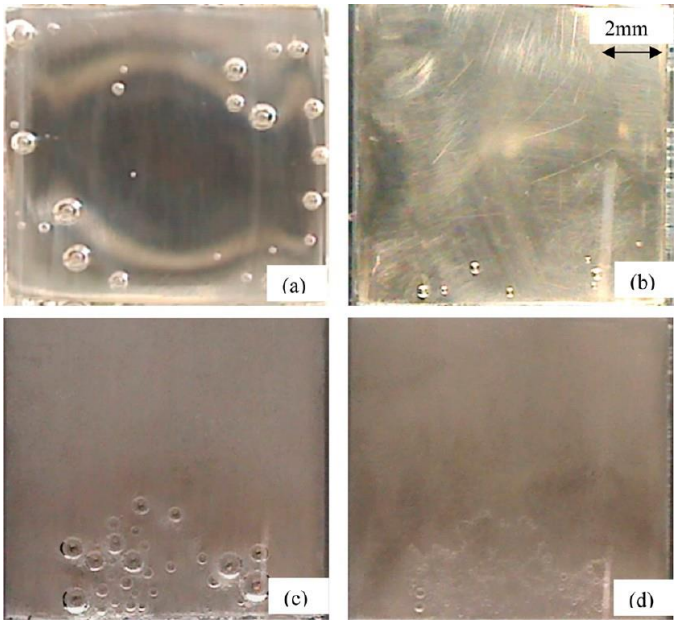

Figure 1.4 Representative images of hydrogen bubbles during the electrolysis in 0.5 M KOH at −0.75 mA cm^{-2} (a) without and (b) with electrolyte circulation; at −200 mA cm^{-2} (c) without and (d) with circulation (Reynolds number for electrolysis at −0.75 mA cm^{-2} and −200 mA cm^{-2} was 2521) [36] (Reprinted with permission from D. Zhang, K. Zeng, Industrial & Engineering Chemical Research, 51(42), pp. 13825-13832. Copyright (2012) American Chemical Society)

However, this process can be effective under limited conditions [34]. The combination of

this and other processes is highly desired to achieve higher efficiency.

Magnetic field

The introduction of a magnetic field is one of the alternative processes to enhance bubble detachment from the electrode surface. It is well known that the magnetic field produces convection by the Lorentz force, described by Eq. (1.3).

$$F_L = \boldsymbol{j} \times \boldsymbol{B} \tag{1.3}$$

where $\boldsymbol{j}$ is the current density and $\boldsymbol{B}$ is the magnetic field. This induced convection, called magnetohydrodynamic (MHD) convection, enhances bubble detachment [37–39]. J. A. Koza et al. reported that the introduction of the magnetic field reduced the diameter of bubbles on the electrode surface in a 0.1 mol dm^{-3} Na_2SO_4 solution, as shown in Figure 1.5. The authors also indicated that the MHD convection introduced by the Lorentz force was directly enhanced by bubble desorption from the surface [40]. T. Iida et al. also reported that applying a high magnetic field reduced the ohmic voltage drop under acidic and alkaline conditions during water electrolysis [37]. This phenomenon was significantly observed at higher current densities. They also reported that the MHD convection triggered bubble detachment from the surface, which led to the reduction of the void fraction in the bubble dispersion layer.

Therefore, it is considered that the magnetic field can improve the efficiency of water electrolysis by reducing the ohmic voltage drop and overpotentials of the electrodes. These improvements are caused by the rapid desorption and diffusion of bubbles from the electrolyte by the MHD convection.

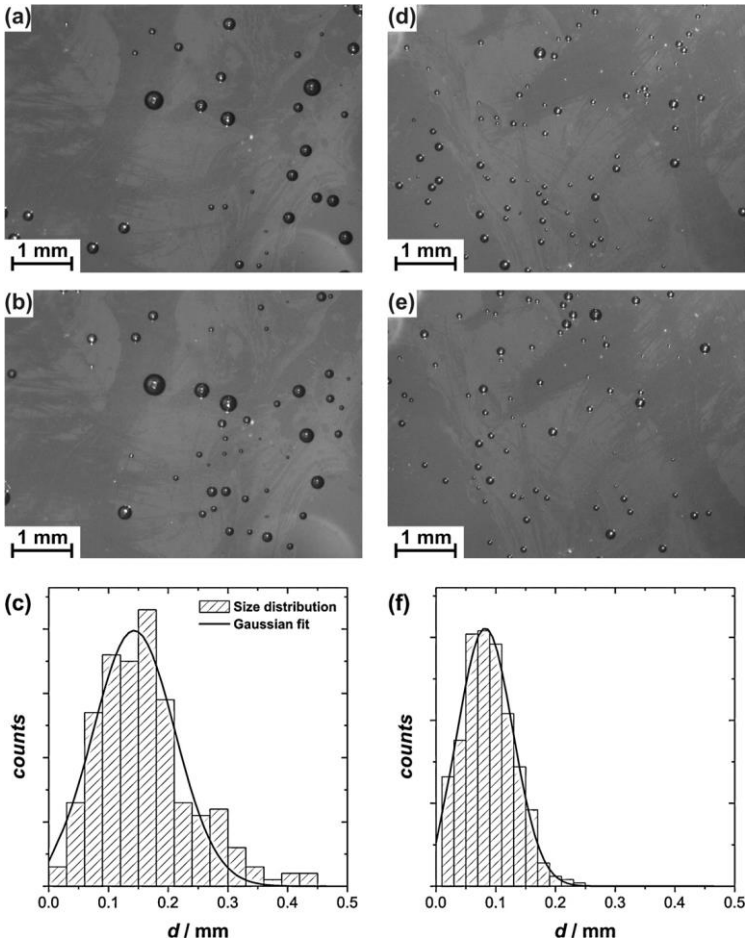

Figure 1.5 Hydrogen bubbles on the electrode surface in the stationary regime observed (a) and (b): without a magnetic field, (d) and (e): parallel to the electrode magnetic field (***B*** = 750 mT) ((b) and (e) are observed after 60 s from (a) and (d)). Distribution of the bubble size (c) without and (f) with magnetic field [40] (Reprinted from Electrochimica Acta, 56, J. A. Koza, S. Mühlenhoff, P. Żabiński, P. A. Nikrityuk, K. Eckert, M.Uhlemann, A. Gebert, T. Weier, L. Schultz, S. Odenbach, Hydrogen evolution under the influence of a magnetic field, 2670, Copyright (2011), with permission from Elsevier.)

Ultrasonic field

The ultrasonic field is another process to enhance bubble detachment from the electrode surface. The cavitation effect produced by the introduction of an ultrasonic field in the water electrolysis process causes the formation of small bubbles [34, 41]. S. D. Li et al. reported that the overpotential of electrolysis decreased in the ultrasonic field by the

formation of cavitation bubbles. In this report, the effect of the ultrasonic field was enhanced under higher current density conditions [42]. M. Y. Lin et al. also demonstrated that the bubbles' diameter was reduced because of the ultrasonic field (Figure 1.6), and the efficiency was improved [43].

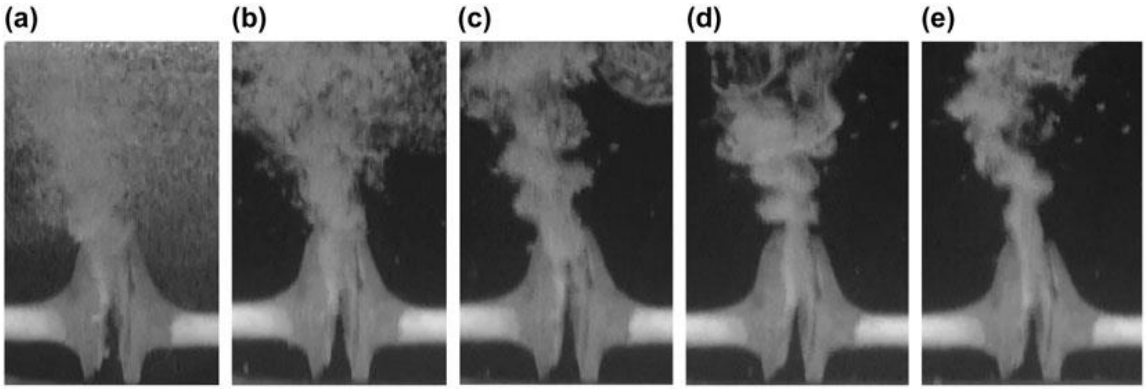

Figure 1.6 Bubble behavior during electrolysis at 4.0 V in 40 wt% KOH under different ultrasonic conditions: (a) 0 W (without ultrasonic field), (b) 225 W, (c) 450 W, (d) 675 W, and (e) 900 W [43] (Ultrasonic wave field effects on hydrogen production by water electrolysis, M-Y Lin, L-W Hourng, Journal of the Chinese Institute of Engineers Copyright © (2014) [Taylor & Francis])

However, several reports have revealed that the effect of the ultrasonic field was weakened to oxygen bubbles due to stronger adsorption on the electrode surface [43].

From these previous researches, the ultrasonic field is also considered a promising candidate to control the hydrogen bubble behavior.

(ii) Bubble behavior control by modification of electrode surface structures

Modification of electrode surface structures, particularly nano/microstructures of the electrode surface, has been considered as a promising approach for controlling bubble behavior. In this approach, surface wettability is critical for enhancing bubble detachment from the surface [44, 45]. On an electrode surface with lower surface wettability, that is, hydrophobic characteristics, the interface between the bubbles and the

electrode surface is stabilized, which causes bubbles to become larger and detach from the electrode with a larger diameter. H. Matsuhisma et al. demonstrated that bubbles tended to be larger on the electrode with a hydrophobic electrolyte under microgravity conditions [46] because of the stabilization of the bubble–electrode interface. Another method to control surface wettability is to modify the nano/microstructures on the surface. Modification of the surface structures to control surface wettability is categorized into two different processes: modification by surfactants and modification of the surface nano/microstructures.

Modification by surfactants

The addition of surfactants is a typical process to change the surface wettability by controlling the surface tension of the bubbles and the electrolyte [47-49]. D. Fernández et al. demonstrated that bubble detachment with a smaller diameter was enhanced on hydrophobic surfaces modified by a high sodium dodecyl sulfate (SDS) concentration (Figure 1.7).

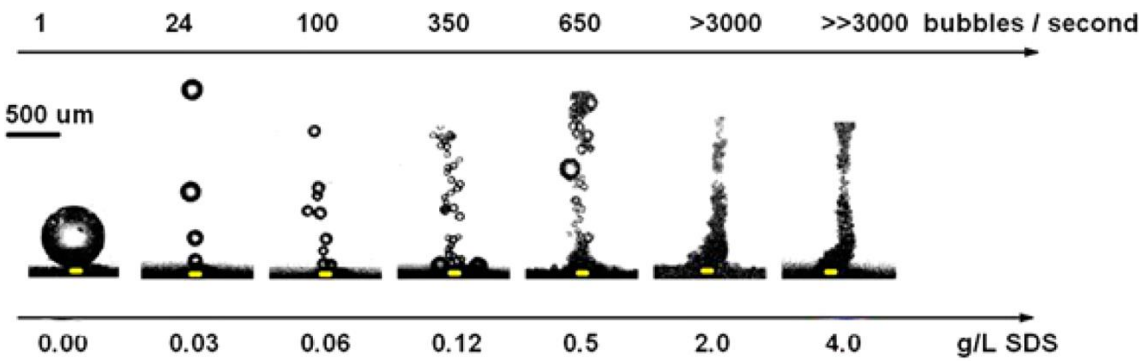

Figure 1.7 Variation of the frequency of bubble detachment with control in the surface tension by SDS addition [47] (Reprinted with permission from D. Fernández, P. Maurer, M. Martine et al., Langmuir, 30, 43, 13065–13074. Copyright (2014) American Chemical Society)

However, the surfactant directly influences the bubble behavior on the surface and also the reactions such as the HER and OER. The surfactant decreases the HER efficiency. Z. D. Wei et al. revealed that hexadecyltrimethylammonium bromide suppressed the HER

on the cathode [49].

Modification of surface nano/microstructures

Another process to control surface wettability is the modification of surface nano/microstructures. Modifying the surface nano/microstructures controls the interfaces among the gas bubbles, electrolyte, and electrode surface, inducing a change in surface tension. This control contributes to surface wettability characteristics, that is, hydrophobic and hydrophilic surfaces [50]. Surface wettability is one of the critical factors influencing the HER activity [51] and bubble behavior. In particular, the hydrophobic surface enhances bubble detachment.

Many surface nano/microstructures have been proposed and mainly separated into pillar-like (including dendritic) and sheet-like structures, which are briefly introduced.

The pillar-like structures show a higher hydrophobic surface by reducing the interface between the bubble and the electrode surface. This induces bubble detachment with a smaller size. S. H. Ahn et al. demonstrated that HER efficiency improved by suppressing bubble adhesion on the surface during the OER on Ni-based electrodes with dendritic morphologies and having a hydrophobic nature [52]. Nano-corn-based structures were also employed as surface structures of the electrodes [53-55]. Y. Li et al. demonstrated that the population of larger bubbles on the surface decreased with a smaller interface area between the bubbles and the surface during potentiostatic electrolysis, as shown in Figure 1.8.

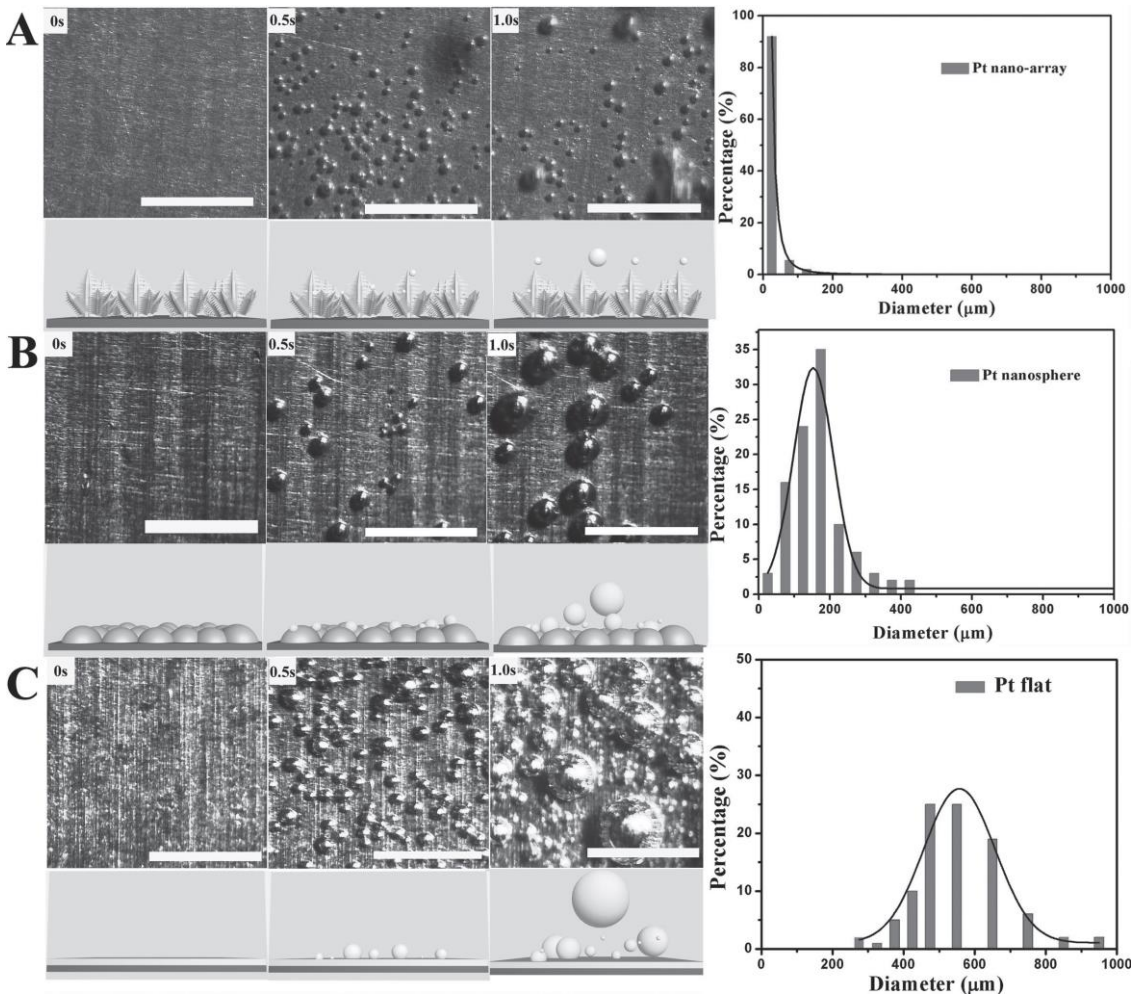

Figure 1.8 Bubble nucleation and growth during water electrolysis in 0.5 M H_2SO_4 and the corresponding distribution of bubble diameter on the electrode with (A) nanoarray Pt, (B) nanosphere Pt, and (C) flat Pt [53] (Under-Water Superaerophobic Pine-Shaped Pt Nanoarray Electrode for Ultrahigh-Performance Hydrogen Evolution, Y. Li, H. Zhang, T. Xu, et al., Advanced Functional Materials Copyright © (2015) [John Wiley and Sons])

G. B. Darband also demonstrated that bubble-induced ohmic potential increase was suppressed by releasing bubbles with a smaller diameter on pillar-like surface nanostructures [55].

The sheet-like structure can enhance bubble detachment because of hydrophobic surface characteristics [56–58]. Z. Lu et al. demonstrated that the MoS_2 nanosheet structure enabled the evolution of smaller bubbles on the surface during electrolysis in

0.5 M H_2SO_4, and HER efficiency was improved by this bubble behavior, as shown in Figure 1.9.

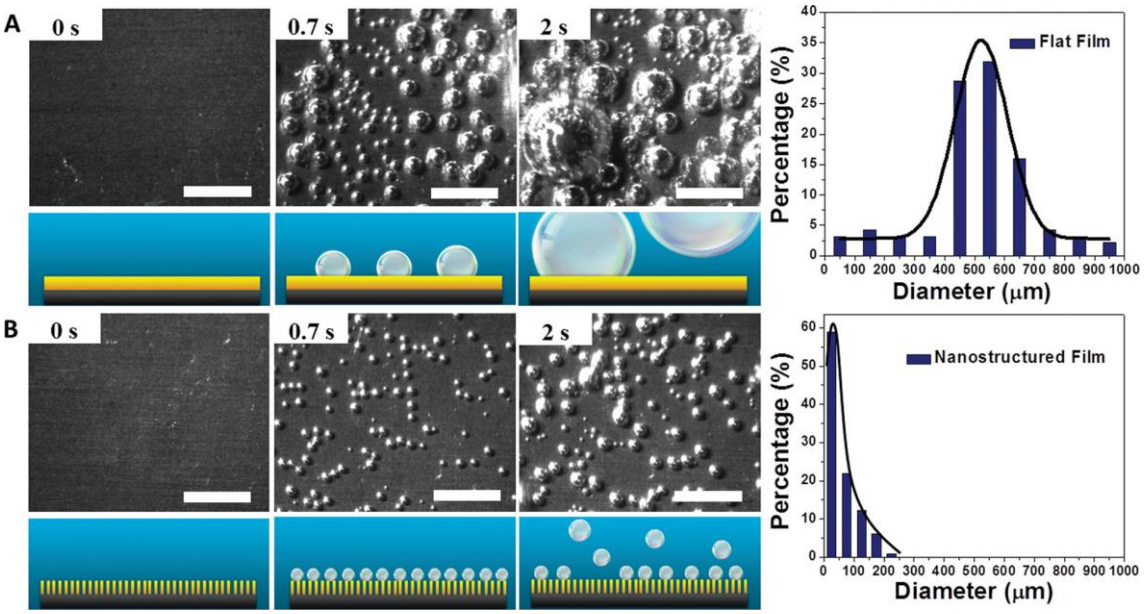

Figure 1. 9 Bubble nucleation and growth during the electrolysis in 0.5 M H_2SO_4 and the corresponding distribution of bubble diameter on (A) flat MoS_2 and (B) nanosheet MoS_2 [56] (Ultrahigh Hydrogen Evolution Performance of Under-Water "Superaerophobic" MoS2 Nanostructured Electrodes, Z. Lu, W. Zhu, X. Yu, et al., Advanced Materials Copyright © (2014) [John Wiley and Sons])

This tendency was also reported on the electrode surface of Ni-Mo alloy nanosheets by Q. Zhang et al. [57] and of Co-B-P alloy nanosheets by H. Sun et al. [58].

From these previous studies, the modification of the surface nano/microstructures can cause the improvement of HER efficiency. This improvement is induced by bubble nucleation and growth on the surface and control of the interface among the bubbles, electrolytes, and electrode surface. Hence, the correlation between bubble behavior and surface structures must be further investigated to propose the design of a highly efficient electrode surface for the HER.

1.3.2. Anion exchange membrane (AEM) water electrolysis process

1.3.2.1. Basic characteristics

The AEM water electrolysis process is a new hydrogen production process [15, 16]. A schematic of this process is shown in Figure 1.10.

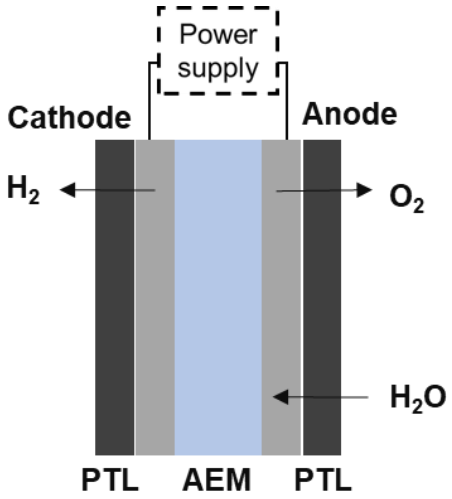

Figure 1.10 Schematic of AEM water electrolysis process based on [16]. PTL: porous transport layer (H. A. Miller, K. Bouzek, J. Hnat, S. Loos, C. I. Bernäcker, T. Weißgärber, L. Röntzsch and J. Meier-Haack, Sustainable Energy Fuels, 2020, 4, 2114- Published by The Royal Society of Chemistry.)

An AEM water electrolysis process consists of a cathode, an anode, a polymer electrolyte, a porous transport layer (PTL), and a power supply unit (Figure 1.4). The electrolyzer configuration is similar to that of a PEM water electrolyzer. The reactions at the cathode and anode are described in Eqs. (1.4) and (1.5), respectively.

$$\text{Cathode:} \qquad 2H_2O + 2e^- \rightarrow H_2 + 2OH^- \tag{1.4}$$

$$\text{Anode:} \qquad 4OH^- \rightarrow O_2 + 2H_2O + 4e^- \tag{1.5}$$

As shown in Eqs. (1.4) and (1.5), the reactions on the cathode and anode are identical to those involved in the alkaline water electrolysis process. H_2O is supplied from the anode

side and diffuses to the cathode side through the AEM. On the cathode side, H_2O is reduced to hydrogen and OH^- ions. The generated OH^- ions migrate to the anode side because of the positive attraction of the anode [59]. KOH or K_2CO_3 are commonly employed as electrolytes, and their concentration is considerably lower than the electrolytes utilized in the alkaline water electrolysis process [15, 16]. The PTL that faces both sides functions as the gas diffusion layer that provides the pathway for the evolved gas and circulating electrolyte and as the current collector.

These fundamental features of the AEM water electrolysis process provide the following advantages: non-noble transition-metal-based materials can be utilized as both cathode and anode materials, because they exhibit a similar reaction mechanism in the AEM and alkaline water electrolysis processes [15, 60], and a lower concentration electrolyte can be used instead of a concentrated KOH solution in an alkaline water process, which enables the use of lower corrosion resistivity materials such as stainless steel in the cell systems [16, 17]. Furthermore, higher efficiency can be achieved by applying a high current density, similar to the PEM electrolysis process [14]. Therefore, this AEM water electrolysis process is promising for next-generation water electrolysis processes.

Despite these strong motivations, few studies have been reported related to commercial applications [61]. The limited application scope is attributed to the low durability of the membrane electrode assembly (MEA) [15, 62] as well as the AEM itself [60]. Furthermore, other components of the AEM electrolysis process, such as PTLs, must be optimized. Thus, the optimization of the MEA will primarily facilitate the realization of the practical applications of the AEM water electrolysis process.

1.3.2.2. Issues on HER electrodes

Regarding the issues on HER electrodes, the low durability of the MEA is one of the most significant problems that must be resolved to achieve higher efficiency. The MEA is divided into two different configurations on the basis of the substrate used to fabricate the catalysts: the catalyst-coated substrate (CCS) and the catalyst-coated

membrane (CCM) processes.

In the CCS process, the electrodes are fabricated onto the substrate, such as PTL. This CCS functions as an electron transfer pathway, a support of the fabricated catalysts, and a pathway to remove gas products such as hydrogen [15]. The CCS process improves the stability of the MEA. Moreover, many fabrication processes for catalysts such as electrodeposition [63, 64], electroless deposition [65], and spray [62, 66], which is the conventional process, are applicable.

In contrast, the CCM process prepares the electrode onto the AEM surface, which enables strong adherence of the electrode on the AEM surface. This strong adhesion results in high ionic conductivity, which is one advantage. Moreover, this process can reduce the amount of catalyst loading without any significant degradation of performance [67]. IH. to et al. demonstrated that the MEA fabricated by the CCM process exhibited higher performance than that by the CCS process because of the improved mass transport of ions such as OH^- [62]. J. E. Park et al. also revealed that CCM-based MEA exhibited high performance because of the decrease in ohmic, charge transfer, and mass transport resistances [68]. Therefore, the CCM process is an effective process for fabricating MEA.

However, the durability of the MEA fabricated by the CCM process must be improved. In the CCM process, the spray process is commonly utilized because of the precise control of the loading amount of the catalyst and ionomers [69]. X. Lu et al. reported that degradation of the ionomer, which causes the deterioration of CCM, was one factor contributing to performance degradation [70]. The carbon-based support used in MEA also degrades under alkaline conditions [60, 71] because of carbon instability. Furthermore, the electrode structures are difficult to control because they are sprayed on AEM using ink containing ionomers and support materials.

From previous studies, a fabrication process for the electrode that can modify the structures without ionomers must be developed to realize high-performance CCM-based MEA in the AEM process. In addition, understanding the effect of electrode structures on HER is essential to improve the HER performance.

1.4. Strategy of this study

As described in this chapter, both alkaline and AEM water electrolysis processes have crucial roles in hydrogen production for large-scale energy storage processes because of the characteristics described in previous chapters. Despite the potential of these processes, their HER performance must be improved for their widening their application scope. In particular, focusing on the catalytic electrodes for HER, which directly produce hydrogen, different issues must be addressed to improve the HER performance of the electrodes for alkaline and AEM water electrolysis processes.

In the case of alkaline water electrolysis, control of the bubble behavior on the electrode surface is a vital issue to improve the electrode performance. Previous studies have indicated that surface nano/microstructures significantly influence bubble behavior, and modification of the surface structures is effective for improving the HER performance. However, the detailed correlation between the surface microstructures on bubble behavior during HER is still unclear.

In the case of AEM water electrolysis, the direct fabrication of the electrode on the AEM results in a lower resistance between the electrodes, improving the HER performance. Previous reports have indicated that the electrodes fabricated by the conventional process exhibit lower durability because of the instability of materials for fabrication. The structures of the electrode are also difficult to control through conventional processes. Thus, a new fabrication process that can modify the surface structures must be investigated. Understanding the effect of surface structures on HER performance is essential to improve the electrode efficiency.

Based on this background, this thesis study aims to propose strategies for highly efficient electrodes in both alkaline and AEM water electrolysis processes.

In Chapters 2 and 3, the effects of surface microstructures and wettability governed by these structures on bubble behavior in alkaline water electrolysis are investigated using surface-modified electrodes. For this, Ni micropatterned and Pt (111) microfacet electrodes were employed as the model electrodes. The micropatterned structures are suitable for quantitative analysis because of their advantages. A Pt (111) microfacet electrode was also employed to analyze the effect of well-defined surfaces.

Through these analyses, the guidelines for the design of surface nano/microstructures for highly efficient catalytic electrodes are proposed.

Chapter 4 focuses on the fabrication of the electrodes on the AEM, and a new fabrication process that can control the surface structures based on electroless deposition is investigated. The effect of the electrodes fabricated by the new process on HER performance is also analyzed in Chapter 5, and the strategy for the design of the surface structures is discussed.

References

[1] Agency for Natural Resources and Energy, http://www.enecho.meti.go.jp/about/special/tokushu/saiene/saienecost.html, (Accessed on November 18th, 2020).

[2] Agency for Natural Resources and Energy, 5th Strategic Energy Plan, http://www.enecho.meti.go.jp/en/category/others/basic_plan/5th/pdf/strategic_energy_plan.pdf, (Accessed on November 19th, 2020).

[3] A. Buttlera, H. Spliethof, Current status of water electrolysis for energy storage, grid balancing and sector coupling via power-to-gas and power-to-liquids: A review, *Renewable Sustainable Energy Rev.*, **82** (2018) 2440.

[4] M. Gotz, J. Lefebvre, F. Mors, A. M. Koch, F Graf, S. Bajohr, R. Reimert, T. Kolb, Renewable Power-to-Gas: A technological and economic review, *Renewable Energy*, **85** (2016) 1371.

[5] M. Kanda, F. Ueno, Market and Technology Trends in Batteries, *Toshiba Review*, **56**(2) (2001) 2.

[6] Ministry of Economy, Trade, and Industry, Report of CO_2 free hydrogen working group, https://www.meti.go.jp/report/whitepaper/data/pdf/20170307001_01.pdf (Accessed on November 19th, 2020).

[7] S. E. Hosseini, M.A. Wahid, Hydrogen production from renewable and sustainable energy resources: Promising green energy carrier for clean development, *Renewable Sustainable Energy Rev*., **57** (2016) 850.

[8] N. Guillet, P. Millet, Hydrogen Production: By Electrolysis, in: A. Gidula, D. Stolten (Eds.), Wiley, Hoboken, 2015.

[9] K. Zeng, D. Zhang, Recent progress in alkaline water electrolysis for hydrogen production and applications, *Prog. Energy Combust. Sci.* **36** (2010) 307.

[10] A. G-Jopek, W. Jehle, J. Wellnitz, Hydrogen Storage Technologies: New Materials, Transport and Infrastructure, Wiley, Hoboken, 2012.

[11] Mueller-Langer F, Tzimas E, Kaltschmitt M, Peteves S. Techno-economic assessment of hydrogen production processes for the hydrogen economy for the short and medium term. *Int. J. Hydrogen Energy* **32** (2007) 3797.

[12] A. Buttler, Hartmut Spliethoff, Current status of water electrolysis for energy storage, grid balancing and sector coupling via power-to-gas and power-to-liquids: A review, *Renewable Sustainable Energy Rev.*, **82** (2018) 2440.

[13] H. Ito, N. Kawaguchi, S. Someya, T. Munakata, N. Miyazaki, M. Ishida, A. Nakano, Experimental investigation of electrolytic solution for anion exchange membrane water electrolysis, *Int. J. Hydrogen Energy*, **43** (2018) 17030.

[14] M. Carmo, D.L. Fritz, J. Mergel, D. Stolten, A comprehensive review on PEM water electrolysis, *Int. J. Hydrogen Energy* **38** (2013) 4901.

[15] H.A. Miller, K. Bouzek, J. Hnat, S. Loos, C.I. Bernäcker, T. Weißgärber, L. Röntzsch, J. Meier-Haack, Green hydrogen from anion exchange membrane water electrolysis: A review of recent developments in critical materials and operating conditions, *Sustain. Energy Fuels* **4** (2020) 2114.

[16] I. Vincent, D. Bessarabov, Low cost hydrogen production by anion exchange membrane electrolysis: A review, *Renewable Sustainable Energy Rev.* **81** (2018) 1690.

[17] S. Marini, P. Salvi, P. Nelli, R. Pesenti, M. Villa, M. Berrettoni, G. Zangari, Y. Kiros, Advanced alkaline water electrolysis, *Electrochim. Acta* **82** (2012) 384.

[18] S. Trasatti, Water electrolysis; Who first?, *J. Electroanal. Chem.* **476** (1999) 90.

[19] Granovskii M, Dincer I, Rosen MA, Environmental and economic aspects of hydrogen production and utilization in fuel cell vehicles. *J. Power Sources* **157** (2006) 411.

[20] R. L. ReLoy, Industrial Water Electrolysis: Present and Future, *Int. J. Hydrogen Energy* **8** (1983) 401.

[21] S. Mitsushima, K. Matsuzawa, Present technologies and subjects of water electrolysis, *Hydrogen Energy System* **36** (2011) 11.

[22] Z. Chen, X. Duan, W. Wei, S. Wang, B. Ni, Recent advances in transition metal-based electrocatalysts for alkaline hydrogen evolution, *J. Mater. Chem. A* **7** (2019) 14971.

[23] X. Zou, Y. Zhang, Noble metal-free hydrogen evolution catalysts for water splitting, *Chem. Soc. Rev.* **44** (2015) 5148.

[24] W. Zhou, J. Jia, J. Lu, L. Yang, D. Hou, G. Li, S. Chen, Recent developments of carbon-based electrocatalysts for hydrogen evolution reaction, *Nano Energy* **28** (2016) 29.

[25] R. L. LeRoy, M. B. I. Janjua, R. Renaud, U. Leuenberger, Analysis of Time-Variation Effects in Water Electrolyzers, *J. Electrochem. Soc.* **126** (1976) 1674.

[26] S. Trasatti, Work Function, Electronegativity, and Electrochemical Behaviour of Metals III. Electrolytic hydrogen evolution in acid solutions, *J. Electroanal. Chem. Interfacial Electrochem.* **39** (1972) 163.

[27] X. Wang, Y. Zheng, W. Sheng, Z. J. Xu, M. Jaroniec, S. Qiao, Strategies for design of electrocatalysts for hydrogen evolution under alkaline conditions, *Mater. Today* **36** (2020) 125.

[28] Y. Yan, B. Xia, Z. Xu, X. Wang, Recent Development of Molybdenum Sulfides as Advanced Electrocatalysts for Hydrogen Evolution Reaction, *ACS Catal.* **4** (2014) 1693.

[29] M. J. Jaksic, M. V. Mojnovic, N. V. Krstajic, Kinetic analysis of hydrogen evolution at Ni-Mo alloy electrodes. *Electrochim. Acta* **45** (2000) 4151.

[30] K. Aldas, Application of a two-phase flow model for hydrogen evolution in an electrochemical cell, *Applied Mathematics and Computation* **154** (2004) 507.

[31] H. Vogt, R. J. Balzer, The bubble coverage of gas-evolving electrodes in stagnant electrolytes, *Electrochim. Acta* **50** (2005) 2073.

[32] P. J. Sides, C. W. Tobias, Resistance of a Planar Array of Spheres: Gas Bubbles on Electrode, *J. Electrochem. Soc.* **129** (1982) 2715.

[33] S. D. Li, C. C. Wang, C. Y. Chen, Water electrolysis in the presence of an ultrasonic field, *Electrochim. Acta* **54** (2009) 3877.

[34] M. Wang, Z. Wang, X. Gong, Z. Guo, The intensification technologies to water electrolysis for hydrogen production – A review, *Renewable Sustainable Energy Rev.* **29** (2014) 573.

[35] J. Eigeldinger, H. Vogt, The bubble coverage of gas-evolving electrodes in a flowing electrolyte, *Electrochim. Acta* **45** (2000) 4449.

[36] D. Zhang, K. Zeng, Evaluating the Behavior of Electrolytic Gas Bubbles and Their Effect on the Cell Voltage in Alkaline Water Electrolysis, *Ind. Eng. Chem. Res.* **51** (2012)13825.

[37] T. Iida, H. Matsushima, Yasuhiro Fukunaka, Water Electrolysis under a Magnetic Field, *J. Electrochem. Soc.* **154** (2007) E112.

[38] H. Matsushima, D. Kiuchi, Y. Fukunaka, Measurement of dissolved hydrogen supersaturation during water electrolysis in a magnetic field, *Electrochim. Acta* **54** (2009) 5858.

[39] D. Fernández, M. Martine, A. Meagher, M. E. Möbius, J. M. D. Coey, Stabilizing effect of a magnetic field on a gas bubble produced at a microelectrode, *Electrochem. Commun.* **18** (2012) 28.

[40] J. A. Koza, S. Mühlenhoff, P. Zabinski, P. A. Nikrityuk, K Eckert, M. Uhlemanna, A. Geberta, T. Weiere, L. Schultza, S. Odenbach, Hydrogen evolution under the influence of a magnetic field, *Electrochim. Acta* **56** (2011) 2665.

[41] N. A. Burton, R. V. Padilla, A. Rose, H. Habibullah, Increasing the efficiency of hydrogen production from solar powered water electrolysis, *Renewable Sustainable Energy Rev.* **135** (2021) 110255.

[42] S-D. Li, C-C. Wang, C.-Y. Chen, Water electrolysis in the presence of an ultrasonic field, *Electrochim. Acta* **54** (2009) 3877.

[43] M-Y. Lin, L-W. Hourng, Ultrasonic wave field effects on hydrogen production by water electrolysis, *Journal of the Chinese Institute of Engineers* **37** (2014) 1080.

[44] D. B. Darband, M. Aliofkhazraei, S. Shanmugam, Recent advances in methods and technologies for enhancing bubble detachment during electrochemical water splitting, *Renewable Sustainable Energy Rev.* **114** (2019) 109300.

[45] D. Zhou, P. Li, W. Xu, S. Jawaid, J. Mohammed-Ibrahim, W. Liu, Y. Kuang, X. Sun, Recent Advances in Non-Precious Metal-Based Electrodes for Alkaline Water Electrolysis, *ChemNanoMat* **6** (2020) 336.

[46] G. Sakata, Y. Fukunaka, H. Matsushima, Nucleation and growth of electrolytic gas bubbles under microgravity, *Int. J. Hydrogen Energy* **39** (2014) 7638.

[47] D. Fernández, P. Maurer, M. Martine, J. M. D. Coey, M. E. Möbius, Bubble Formation at a Gas-Evolving Microelectrode, *Langmuir* **30** (2014) 13065.

[48] S. Lubetkin, The motion of electrolytic gas bubbles near electrodes, *Electrochim. Acta* **48** (2002) 357.

[49] Z. D. Wei, M. B. Ji, S. G. Chen, Y. Liu, C. X. Sun, G. Z. Yin, P. K. Shen, S. H. Chan, Water electrolysis on carbon electrodes enhanced by surfactant, *Electrochim. Acta* **52** (2007) 3323.

[50] T. Darmanin, E. T. de Givenchy, S. Amigoni, F. Guittard, Superhydrophobic Surfaces by Electrochemical Processes, *Adv. Mater.* **25** (2013) 1378.

[51] L. Wang, F. Xiao, The Importance of Catalyst Wettability, *ChemCatChem* **6** (2014) 3048.

[52] S. H. Ahn, I. Choi, H-Y Park, S. J. Hwang, S. J. Yoo, E. Cho, H-J Kim, D. Henkensmeier, S. W. Nam, S-K. Kim, J. H. Jang, Effect of morphology of electrodeposited Ni catalysts on the behavior of bubbles generated during the oxygen evolution reaction in alkaline water electrolysis, *Chem. Commun.* **49** (2013) 9323.

[53] Y. Li, H. Zhang, T. Xu, Z. Lu, X. Wu, P. Wan, X. Sun, L. Jiang, Under-Water Superaerophobic Pine-Shaped Pt Nanoarray Electrode for Ultrahigh-Performance Hydrogen Evolution, *Adv. Funct. Mater.* **25** (2015) 1737.

[54] G. B. Darband, M. Aliofkhazraei, A. S. Rouhaghdam, Three-dimensional porous Ni-CNT composite nanocones as high performance electrocatalysts for hydrogen evolution reaction, *J. Electroanal. Chem.* **829** (2018) 194.

[55] G. B. Darband, M. Aliofkhazraei, S. Hyun, A. S. Rouhaghdam, S. Shanmugam, Electrodeposited NiCoP hierarchical nanostructure as a cost-effective and durable electrocatalyst with superior activity for bifunctional water splitting, *J. Power Sources* **429** (2019) 156.

[56] Z. Lu, W. Zhu, X. Yu, H. Zhang, Y. Li, X. Sun, X. Wang, H. Wang, J. Wang, J. Luo, X. Lei, L. Jiang, Ultrahigh Hydrogen Evolution Performance of Under-Water "Superaerophobic" MoS_2 Nanostructured Electrodes, *Adv. Mater.* **26** (2014) 2683.

[57] Q. Zhang, P. Li, D. Zhou, Z. Chang, Y. Kuang, X. Sun, Superaerophobic Ultrathin Ni–Mo Alloy Nanosheet Array from In Situ Topotactic Reduction for Hydrogen Evolution Reaction, *Small* **13** (2017) 1701648.

[58] H. Sun, W. Xi, G. Yan, H. Tan, L. Xiao, S. Cheng, S. U. Khan, Y. Wang, Y. Li, Superaerophobic P-doped $Ni(OH)_2/NiMoO_4$ hierarchical nanosheet arrays grown on Ni foam for electrocatalytic overall water splitting, *Dalton Trans.* **47** (2018) 8787.

[59] Y. Leng, G. Chen, A. J. Mendoza, T. B. Tighe, M. A. Hickner, C-Y. Wang. Solid-state water electrolysis with an alkaline membrane. *J. Am. Chem. Soc.* **134** (2012) 9054.

[60] J. R. Varcoe, P. Atanassov, D. R. Dekel, A. M. Herring, M. A. Hickner, P. A. Kohl, A. R. Kucernak,

W. E. Mustain, K. Nijmeijer, K. Scott, T. Xu, L. Zhuang, Anion-exchange membranes in electrochemical energy systems, *Energy Environ. Sci.* **7** (2014) 3135.

[61] C. C. Pavel, F. Cecconi, C. Emiliani, S. Santiccioli, A. Scaffidi, S. Catanorchi, M. Comotti, Highly Efficient Platinum Group Metal Free Based Membrane-Electrode Assembly for Anion Exchange Membrane Water Electrolysis, *Angew. Chem. Int. Ed.* **53** (2014) 1378.

[62] H. Ito, N. Miyazaki, S. Sugiyama, M. Ishida, Y. Nakamura, S. Iwasaki, Y. Hasegawa, A. Nakano, Investigation on electrode configurations for anion exchange membrane electrolysis, *J. Appl. Electrochem.* **48** (2018) 305.

[63] N. V. Kuleshov, V. N. Kuleshov, S. A. Dovbysh, S. A. Grigoriev, S. V. Kurochkin, P. Millet, Development and performances of a 0.5 kW high-pressure alkaline water electrolyzer, *Int. J. Hydrogen Energy* **44** (2019) 29441.

[64] S. H. Ahn, B. S. Lee, I. Choi, S. J. Yoo, H. J. Kim, E. Cho, D. Henkensmeier, S. W. Nam, S. K. Kim, J. H. Jang, Development of a membrane electrode assembly for alkaline water electrolysis by direct electrodeposition of nickel on carbon papers, *Appl. Catal. B* **154** (2014) 197.

[65] S. Vengatesan, S. Santhi, S. Jeevanantham, G. Sozhan, Quaternized poly (styrene-co-vinyl benzyl chloride) anion exchange membranes for alkaline water electrolyzers, *J. Power Sources* **284** (2015) 361.

[66] X. Chu, Y. Shi, L. Liu, Y. Huang, N. Li, Piperidinium-functionalized anion exchange membranes and their application in alkaline fuel cells and water electrolysis, *J. Mater. Chem. A* **7** (2019) 7717.

[67] J. Hnát, M. Plevova, R. A. Tufa, J. Zitka, M. Paidar, K. Bouzek, Development and testing of a novel catalyst-coated membrane with platinum-free catalysts for alkaline water electrolysis, *Int. J. Hydrogen Energy* **44** (2019) 17493.

[68] J. E. Park, S. Y. Kang, S. H. Oh, J. K. Kim, M. S. Lim, C. Y. Ahn, Y. H. Cho, Y. E. Sung, High-performance anion-exchange membrane water electrolysis, *Electrochim. Acta* **295** (2019) 99.

[69] M. S. Wilson, S. Gottesfeld, Thin-film catalyst layers for polymer electrolyte fuel cell electrodes, *J. Appl. Electrochem.* **22** (1992) 1.

[70] X. Wu, K. Scott, A Li-doped Co3O4 oxygen evolution catalyst for non-precious metal alkaline anion exchange membrane water electrolyzers, *Int. J. Hydrogen Energy* **38** (2013) 3123.

[71] A. Zadick, L. Dubau, N. Sergent, G. Berthome, M. Chatenet, Huge Instability of Pt/C in Alkaline Medium, *ACS Catal.* **5** (2015) 4819.

Chapter 2:

The Effect of Surface Wettability on Bubble Growth Behavior using Micro-Patterned Electrodes

2.1. Introduction

In alkaline water electrolysis process, hydrogen is generated by the following rection described in (2.1) on the cathode.

$$2H_2O + 2e^- \rightarrow H_2 + 2OH^- \quad (2.1)$$

This reaction is called the Hydrogen Evolution Reaction (HER), and the catalytic electrode is required to achieve HER efficiently. HER proceeds on the catalytic electrode, and bubble nucleation and growth take place on the electrode continuously. A decrease in the overpotential for HER is necessary to improve the efficiency of the whole process. In conventional water electrolysis applications, Pt is one of the most common materials for the HER catalytic electrode because it shows the highest HER activity [1] and longer stability. However, the scarcity of Pt causes the higher cost of the catalytic electrode, and the applications are limited. Therefore, a lower-cost catalytic electrode with higher HER activity and longer durability must be developed.

Two significant problems should be overcome to realize the catalytic electrode with higher HER activity, longer durability, and lower-cost. One problem is the scarcity of the electrode materials for HER. The new catalytic electrode materials such as transition metal-based materials [2-4] and carbon-based materials [5] have been widely investigated and developed. The other problem is the degradation of HER efficiency caused by evolved bubbles on the electrode surface as HER proceeds. The previous studies have indicated that generated bubbles by HER influence the current distribution [6] and inhibit the reaction sites on the electrode surface [7, 8]. These behaviors cause the inhibition of H_2O access to the electrode surface. Moreover, released bubbles from the surface increase the ohmic resistance between the cathode and the anode because of their insulating characteristics of the bubbles.

The surface morphologies [9] and nano/microstructures on the electrode surface [10, 11] are known as essential factors that control the evolved bubbles' behaviors on the surface to access the H_2O molecules. Controlling bubble behaviors on the surface

is an important strategy for improving HER catalytic electrodes' efficiency.

Despite these analyses of the bubble behaviors on the electrodes during HER, the correlations between the surface structures and bubble behaviors are still unknown. Among the many parameters to control the characteristics of the electrode surface, surface wettability is recognized as one of the critical parameters that govern the nature of the electrode surface. The effects of surface wettability have been widely investigated in the field of not only the electrosynthesis [12, 13] and fabrication of the functional surfaces [14-16] but also the interfacial processes and the catalytic reactions on the electrode surface [17, 18]. Y. Li et al. demonstrated that micro-scale structures on the electrode surface improved HER efficiency due to low bubble adhesive force [19]. Gh. Darband et al. also demonstrated that micro-scale dendritic-like structures enhanced bubble detachment from the electrode [20]. However, the detailed effects of the surface wettability on bubble behaviors and the correlation between surface microstructures and bubble behaviors have not been fully elucidated.

The micro-patterned structure is suitable for the quantitative analyses of the effect of the surface wettability on the bubble behaviors. It has repeated the same microdots and can control the surface wettability by tuning the pitches and the intervals of the microdots [21, 22]. It has also been indicated that the micro-patterned structure governs the surface wettability parameters independently [21]. Choi et al. also demonstrated that tailoring the micro-scale structures on the electrode surface exhibits superhydrophobicity [23]. Thus, the micro-patterned structures are adequate for the quantitative analyses of the micro-scale structures' effect and the mechanism of the bubble behaviors on the textured surface.

This chapter aims to elucidate the correlation between micro-patterned structures, the surface wettability, and bubble behaviors on the electrode surface in order to achieve the higher HER performance. Firstly, Ni micro-patterned electrodes were fabricated using a combination of the lithography technique and electrodeposition process. The bubble behaviors were observed on the different micro-patterned surfaces using the *in situ* measurement system, and the bubble diameter distribution analyses were carried out. The structural factors that control bubble behaviors were investigated by comparing the bubble behaviors on the different electrodes. The mechanism of bubble behaviors on the

microtextured surface is discussed.

2.2. Experimental

2.2.1. Fabrication of Ni micro-patterned electrodes

Cu substrates were mechanically polished by a mechanical laptop polishing machine (MA-400, Musashino Denshi Co.) with a colloidal silica slurry (Planerlite 7101, Fujimi Incorporated) to obtain a specular finishing surface. In this study, Cu was selected as the substrate material because it shows lower HER activity [1] than Ni used as the catalyst material. After that, the photoresist (OFPR-200, Tokyo Ohka Kogyo Co. and AZ P4000, Merck KGaA) was spin-coated on the polished Cu surface. The Cu substrates covered with the photoresist were exposed by the UV light from 10 s to 70 s (BA-6, SÜSS MICROTEC Co.) to form the micropores. After UV exposure, the Cu substrates were developed by the developing solution (NMD-3, Tokyo Ohka Kogyo Co.) for 20 to 40 s, then rinsed by the ultra-pure water for 3 min.

In order to prepare Ni microarrays, Ni microdots were electrodeposited by the periodic reverse (PR) deposition. Ni was selected as the catalyst material in this analysis because Ni shows inherently high HER activity [1] and is widely adopted in the industrial alkaline water process [24,25]. For the microdots' electrodeposition, the prepared micro-patterned Cu substrates were used as the working electrode, the Pt mesh and Ag/AgCl electrode were employed as the counter and the reference electrodes, respectively. The electrodeposition bath was employed a 0.05 mol dm^{-3} $NiCl_2 \cdot 6H_2O$ (UGR grade, Kanto Chemical Co.) solution adjusted to pH 2.5 using an HCl solution (Regent grade, Kanto Chemical Co.). In the PR deposition process, −1200 mV vs. Ag/AgCl for 20 s and the open circuit potential (OCP) for 20 s were applied repeatedly. The step number of PR deposition was defined as a total set of −1200 mV vs. Ag/AgCl for 20 s and OCP for 20 s, and the number of this step number was varied to control the structure of the microdot. The Ni microdot fabrication process scheme and the conditions for the electrodeposition process were shown in scheme 2.1 and Table 2.1.

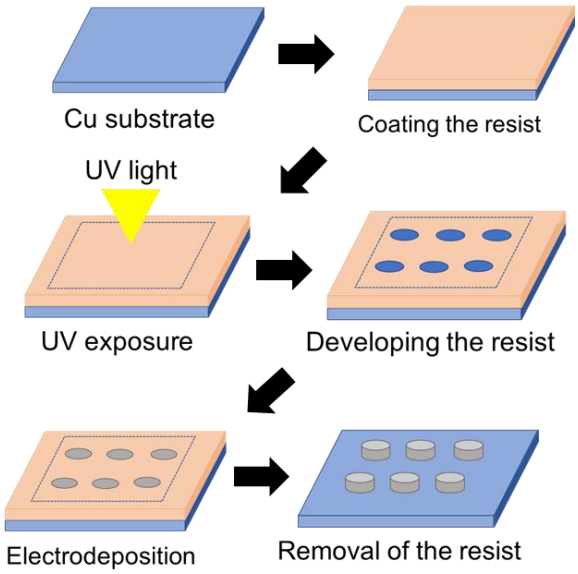

Scheme 2.1 Fabrication process of Ni micro-patterned electrodes

Table 2.1 Electrodeposition conditions for Ni micro-patterned electrodes

$NiCl_2 \cdot 6H_2O$	0.05 M
Temperature	R. T. (23 °C)
pH	2.5 (adjusted by HCl)
W. E.	Patterned Cu
C. E.	Pt mesh
R. E.	Ag/AgCl
Potential	-1200 mV, REST
Time	20 s

2.2.2. analysis of the bubble behaviors on the electrode surface

In order to evaluate the surface morphologies of prepared microdots, a scanning electron microscopy (VE-7800, Keyence Corp. and SU-8240, Hitach) was employed. The contact angle measurements of fabricated micro-patterned electrodes were conducted by

a contact angle measurement system (LCD-400S and FAMAS, Kyowa Interface Science Co. Ltd. and DM500, Kyowa Interface Science Co.) to evaluate the surface wettability of micro-patterned structures.

Electrolyte for water electrolysis process was 1.0 mol dm^{-3} KOH solution. KOH was used in the conventional alkaline water electrolysis process [26]. The concentration of KOH was lower than the industrial process [24, 26], though it was suitable for monitoring bubble behaviors on the electrode surface. The 48 wt% KOH solution (UGR grade, Kanto Chemical Co.) was diluted by ultra-pure water to prepare a 1.0 mol dm^{-3} KOH solution. Prior to measure the water electrolysis process, the KOH solution was deaerated by N_2 gas for 20 min to remove dissolved oxygen from the electrolyte. All electrochemical measurements were carried out by an electrochemical measurement system (HZ-7000, Hokuto Denko Co.). The three-electrodes system consists of prepared Ni micro-patterned electrodes as the working electrode, Pt mesh as the counter electrode, and Hg/HgO electrode (Inter Chemie Inc.) as the reference electrode was employed for the electrochemical measurements. A schematic image of the cell is shown in Figure 2.1.

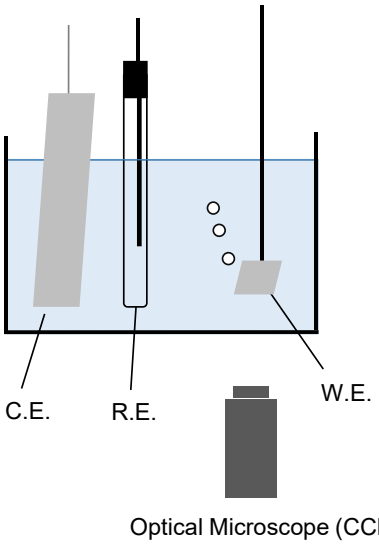

Figure 2.1. Schematic image of the cell for water electrolysis

Linear sweep voltammetry (LSV) of the micro-patterned electrode in 1.0 mol dm^{-3} KOH was measured by sweeping the potential from the rest potential to -1.5 V vs. Hg/HgO with 10 mV s^{-1}. For evaluating the HER efficiency, galvanostatic electrolysis at −20 mA

cm^{-2} for 30 min was also measured. The current density value is much lower than the industrial water electrolysis [24]. It is suitable for observation of the bubble behaviors on the surface. The current density values in this chapter were calculated by the geometrical surface area of the electrodes.

For analyzing the bubbles' behaviors on the surface, an optical microscope was employed using a high-speed CCD camera (HAS-U2, DITECT Corp.) equipped with a micro zoom lens (VSZ-0745, VS Technology) for the *in situ* observation of the bubble behavior. The evolved hydrogen bubble behavior on the electrode surface was observed during the galvanostatic electrolysis at −20 mA cm^{-2}, 1200 s from the start. The flame rate of the high-speed camera was set as 400 frames per second (fps). The bubbles' diameter distribution on the different micro-array structure during the measurement was analyzed from the result obtained by the *in situ* observation. Image processing and analyzing software (ImageJ) were used to measure the diameters of the bubble and analyze the diameters' distribution.

2.3. Results and Discussion

2.3.1. analysis of the correlation between micro-patterned structures and surface wettability

Ni micro-patterned electrodes were fabricated by the electrodeposition process, and SEM images of the micro-patterned electrodes were shown in Figure 2.2. Figure 2.2 shows that the micro-patterned electrodes with uniformly deposited Ni microdots are successfully prepared by the process shown in scheme 2.1. In order to vary the diameter of each microdot, the exposure duration of UV light in the lithography process was changed from 10 s to 70 s, as shown in Figure 2.2 (a) and (b). Moreover, to consider the difference of microdot, particularly focusing on the edge structures, the electrodes with different microdot structures; the cylindrical (Figure 2.2(b)) and the semispherical (Figure 2.2 (c)) were fabricated by varying the step number of the PR deposition process.

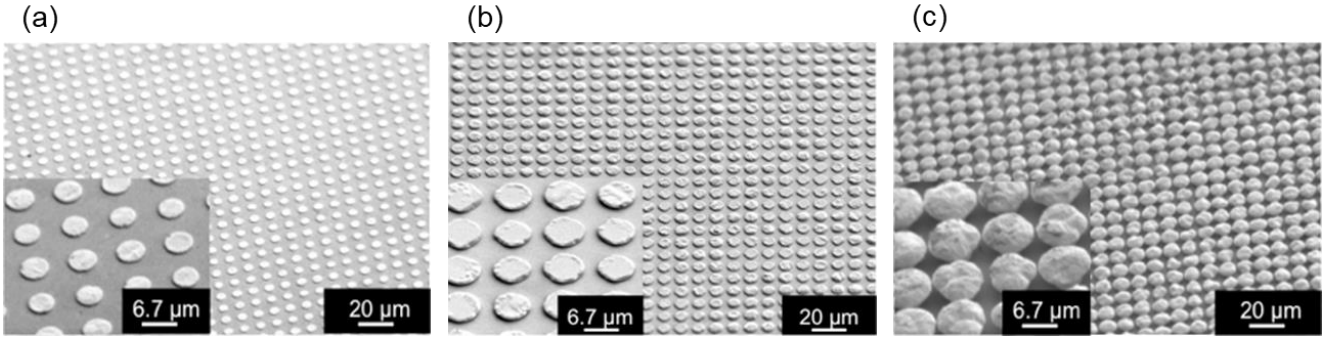

Figure 2.2 Representative SEM images of prepared Ni micro-patterned electrodes; (a) cylindrical microdot with small diameter, (b) cylindrical microdot with large diameter, and (c) semispherical microdot with a large diameter. Inserted SEMs is the enlarged view of the micro-patterned electrodes

In this analysis, the microdot's diameter, as shown in Figure 2.2, was approximately 5-10 μm. The reason for choosing these sizes is to control the microscale surface wettability. It is difficult to change the surface wettability when larger-sized microdots are used based on previous studies [21, 27]. Hence, it was suitable for this analysis.

Furthermore, in order to evaluate the structural changes of the prepared Ni micro-

patterned electrodes, it is necessary to convert these structures to a particular parameter. In this study, the Ni coverage, the ratio of Ni microarray areas to the Cu substrate was calculated as the parameter by the following process from SEM images in Figure 2.2. From the SEM images, it is hypothesized that each microdot's shape from the top view is the circle-like shape, and the average diameter of the micro-patterned electrode was measured. Then, the Ni coverage was calculated as the following equation (2.2).

$$Ni\ coverage\ (\%) = \frac{\pi(d_a/2)^2}{L^2} \times 100 \qquad (2.2)$$

In equation (2.2), d_a and L are defined as the average diameter and the actual distance decided by the photomask for the lithography (L = 10, 15, or 20 μm in this study). The correlation between the Ni coverage and the contact angle value was investigated to quantitatively analyze the effect of structural changes of the electrodes on the surface wettability.

The contact angle of the micro-patterned electrode with different Ni coverage was measured using a water droplet in the ambient condition. The correlation between the Ni coverage and measured contact angle values is shown in Figure 2.3.

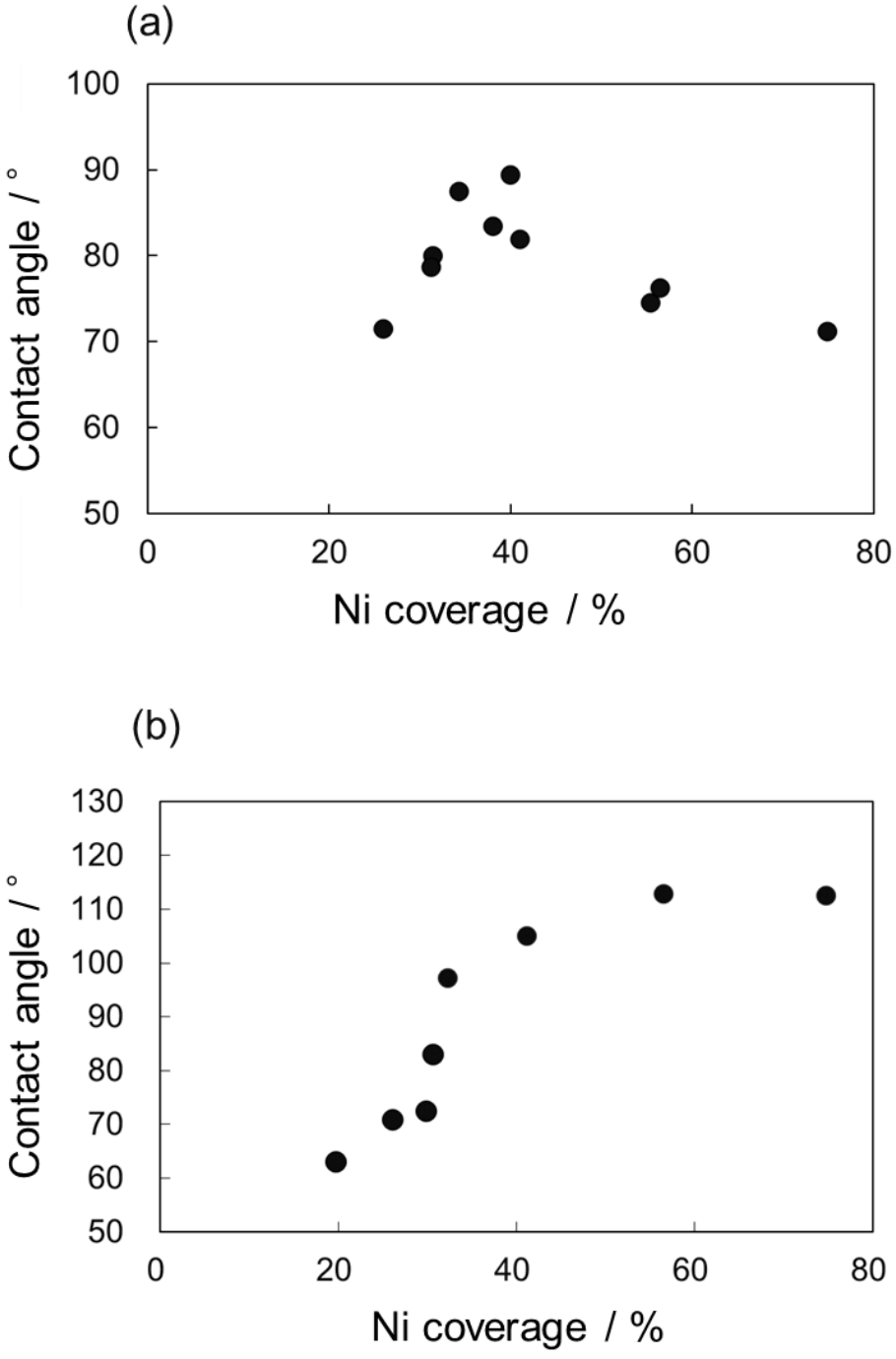

Figure 2.3 The correlation between the Ni coverage and measured contact angle values on the Ni micro-patterned electrodes with (a) cylindrical microdot and (b) semispherical microdot

Figure 2.3 shows the horizontal and vertical axes exhibit the calculated Ni coverage by Eq. (2.2) and the measured contact angles, respectively. From the results, in the lower Ni coverage region lower than 40 %, the contact angle transient with different microdot structures shows the same tendency. As the Ni coverage increases, the value of the contact angle also increases, indicating that a decrease of the microdot intervals contributed to the transition from the hydrophobic state of the textured surface (called as Wenzel surface wettability model [28]) to the hydrophilic state of the textured surface (called as Cassie-Baxter surface wettability model [29,30]).

In higher Ni coverage than 40 %, the transient of the contact angles shows differently on the micro-patterned electrodes with different microdot structures. From Figure 2.3 (a), the value of the contact angles decreases with increasing Ni coverage. This behavior indicates that the Ni micro-patterned structures with larger microdot diameters behave similarly to the flatly electrodeposited Ni electrode surface. The flatly deposited surface shows relatively higher wettability compared with polished or micro-patterned Ni surface. This characteristic could explain how the contact angles on cylindrical micro-patterned electrodes behave in the higher Ni coverage region. In contrast, the trend of contact angle on the semispherical electrodes was changed. In Figure 2.3 (b), the contact angle remains stable at approximately 110 °, irrespective of changing the Ni coverage region by more than 40 %. This trend indicates that the microdot structure also governs the surface wettability of the micro-patterned electrodes. When the Ni coverage of semispherical microdots increases, the semisphere head is also enlarged. The larger semisphere head decreases the interface between the droplet and the microdot. This decrease could cause a destabilizing effect of a water droplet on the surface [29, 31]. The schematic images of these behaviors on the different micro-patterned electrodes are shown in Figure 2.4.

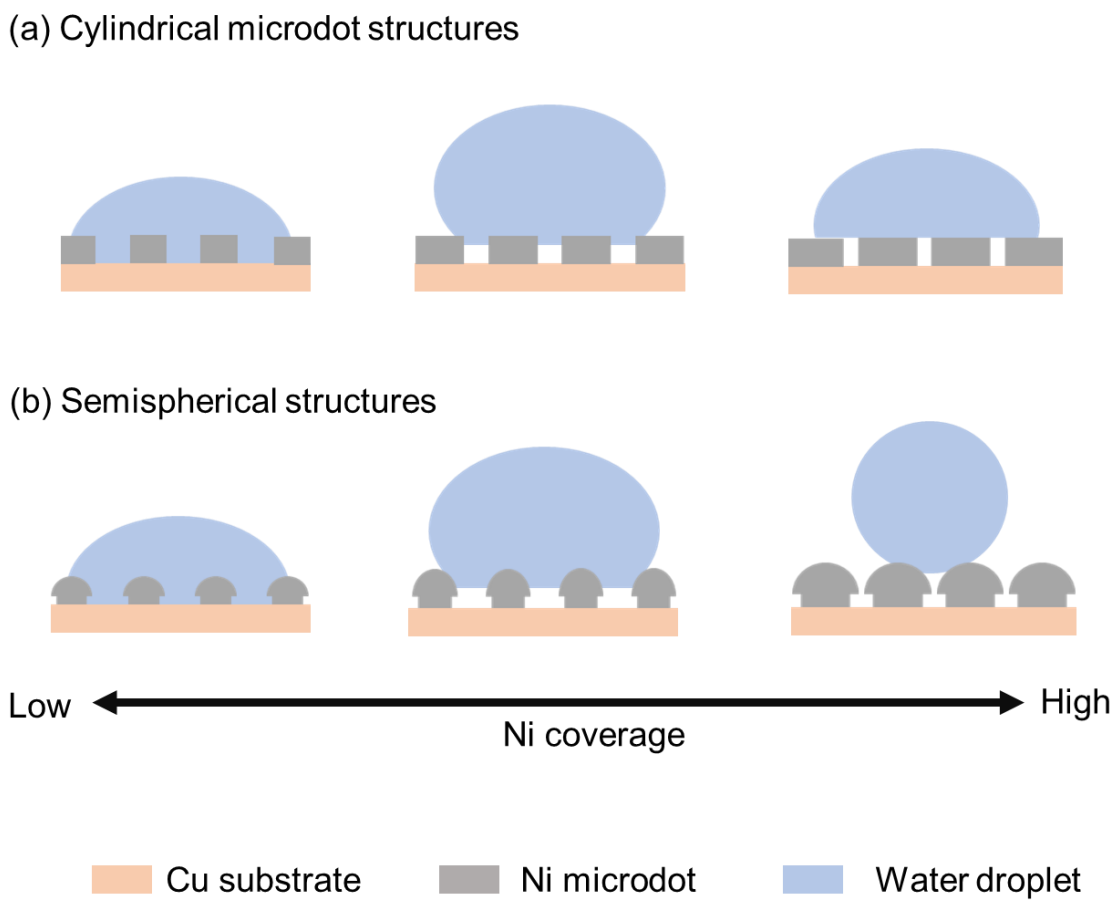

Figure 2.4 Schematic images of surface wettability's behavior with the change of the Ni coverage on (a) cylindrical and (b) semispherical microdots.

Therefore, both the micro-patterned structures and the microdot structures affected the surface wettability. Moreover, the Ni micro-patterned electrodes that can tune the surface wettability by tailoring microdot structures were successfully prepared using the UV lithography technique and electrodeposition process.

2.3.2. analysis of the effect of controlled surface wettability on bubble behaviors

Next, to analyze the microstructures' influence and surface wettability on HER performance, the electrochemical measurements were carried out by employing the

micro-patterned electrodes. The LSV by sweeping the potential range from OCP to −1.5 V vs. Hg/HgO with a scan speed of 10 mV s^{-1} was performed in order to analyze the effect of the surface wettability and the micro-patterned structures on HER activity in Figure 2.5.

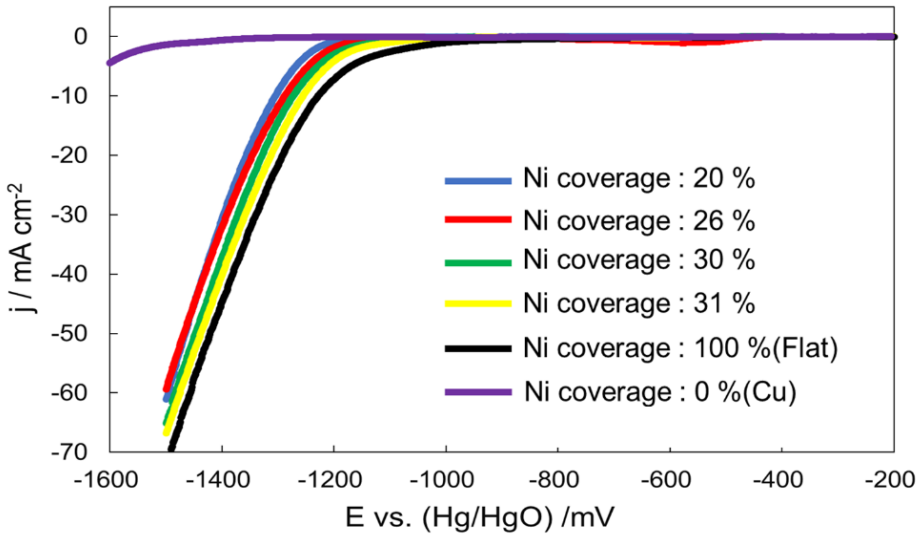

Figure 2.5 LSV of the micro-patterned electrodes with different Ni coverage

In Figure 2.5, the electrochemically active surface area of the micro-patterned electrodes was estimated by the same method with the Ni coverage calculation described above. By this process, the value of the current density in Figure 2.5 was estimated. Figure 2.5 shows that the current density is increased around −1200 mV vs. Hg/HgO on Ni micro-patterned electrodes except for 0% Ni coverage (same as Cu electrode). This result indicates that Cu has no HER activity at approximately −1200 mV vs. Hg/HgO and HER proceeds not on the Cu substrate region but on the Ni micro-patterned region in the electrodes. It is also suggested that Ni micro-patterned structure (e. g., cylindrical and semispherical structures) shows little influence on HER activity due to no significant change of the onset potential in Figure 2.5. On the other hand, the difference among Ni micro-patterned electrodes and the Ni flat electrode appears. Around −5 mA cm^{-2}, the overpotential difference tends to be smaller as the Ni coverage increases. For example, by comparing the Ni coverage of 20% and that of 100%, the value of the overpotential difference was around 100 mV. The bubbles evolved on the electrode cover the reaction sites. This

phenomenon may cause the difference between the calculated surface area from Ni coverage and the actual region where HER proceeds. In contrast, the difference of the overpotentials tends to be smaller at higher current densities. This result suggests that the micro-patterned structure can accelerate the bubble detachment from the surface than the flat surface, which leads to a decrease in the overpotential for evolving the following bubbles on the surface.

To further analyze the effect of the micro-patterned structures and wettability on HER efficiency, the galvanostatic electrolysis at −20 mA cm^{-2} for 30 min was carried out.

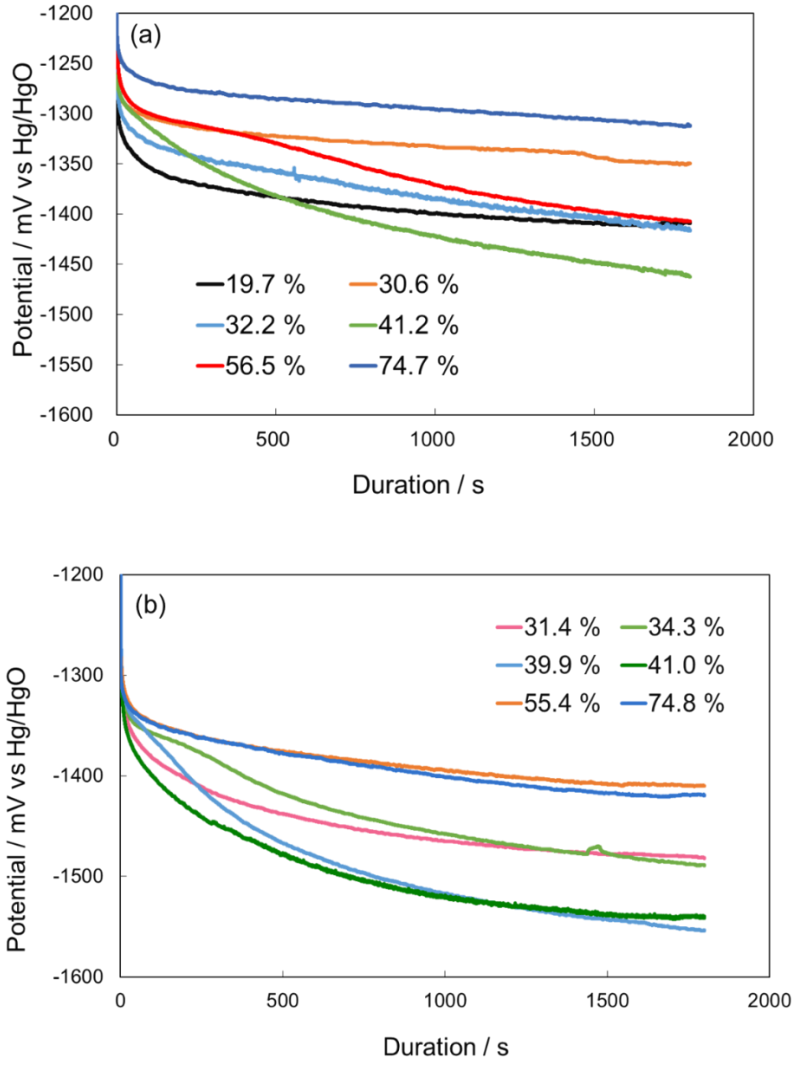

Figure 2.6 Chronopotentiograms of the Ni micro-patterned electrodes with (a) cylindrical and (b) semispherical microdots (−20 mA cm^{-2} for 30 min)

The current density of −20 mA cm^{-2} was determined by the geometrical surface area. Figures 3 (a) and (b) show the potential profiles of the galvanostatic electrolysis on the cylindrical and the semispherical micro-patterned electrodes. From the potential profiles in Figures 3(a) and (b), the potential on the micro-patterned electrodes increases as the electrolysis duration proceeds, regardless of the difference of the microdot structures. One of the possible reasons for this tendency is that evolved hydrogen bubbles stay on the electrode surface. Previous studies indicated that the electrode covered with hydrogen bubbles caused the increase of the electrical resistance and ohmic losses because of the insulating characteristics of hydrogen bubbles [7, 32]. In addition, the current distribution is changed by the existence of hydrogen bubbles on the electrode surface, which leads to an increase of the overpotential [6]. For these reasons, HER could proceed with higher potentials because of the evolved hydrogen bubbles' effect on the surface.

To evaluate the effect of surface wettability on the potential increase, one of the indicators for HER performance, the value differences in the potentials from 200 s to 1800 s during the electrolysis, were calculated from the potential profiles shown in Figure 2.6. Figure 2.7 shows the correlation between the measured surface wettability of the electrodes and the calculated potential differences.

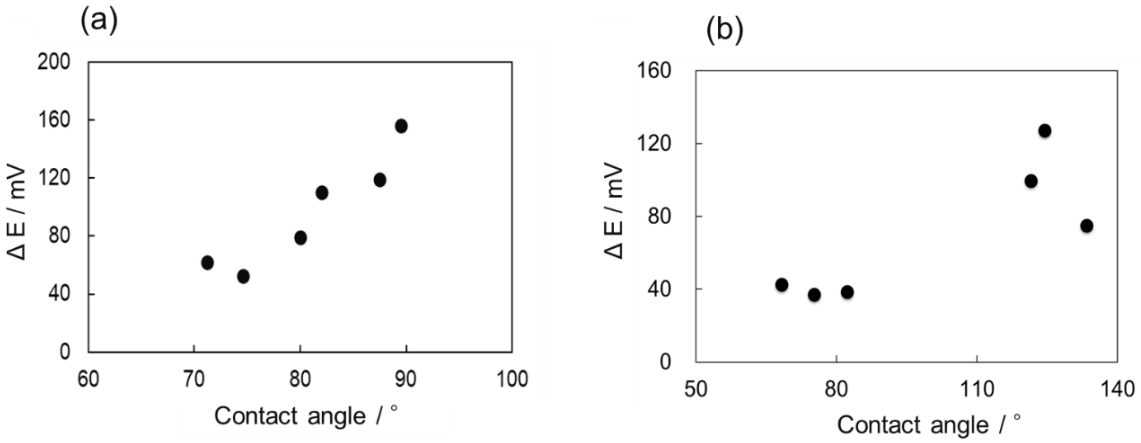

Figure 2.7 The correlation between the measured contact angles and the potential difference on the micro-patterned electrodes with (a) cylindrical and (b) semispherical microdots

The period was selected from 200 s to 1800 s because HER seemed to proceed stably in the potential profile shown in Figure 2.6. During this duration, the effect of evolved bubbles could appear. In Figure 2.7, the vertical and horizontal axes show the measured contact angles and the calculated potential differences. The potential differences increases as the contact angle became large regardless of the microdot's structural difference in Figure 2.7. This tendency indicates that lower wettability caused by microstructures contributes to the overpotential increase for HER by affecting the bubble behaviors on the surface. The previous studies also indicated that growing and/or aggregating the bubbles on the surface are enhanced by the lower surface wettability [33]. From the results mentioned above, it can be concluded that the lower surface wettability modified by the micro-patterned structures degrade the HER efficiency by enhancing bubble growth and/or aggregation on the surface. It is also suggested that controlling the micro-patterned structures suppress large bubbles on the electrode surface.

To further analyze the detailed effect of the surface wettability modified by micro-patterned structure on bubble nucleation and growth process contributing to the HER efficiency, the bubble behaviors on the different micro-patterned electrode surface during the electrolysis were investigated by *in situ* bubble behavior measurements on the electrode. Firstly, the bubble diameter on the electrode surface was analyzed. Figure 2.8 shows the representative results of the *in situ* optical images on the electrode surface obtained by a high-speed CCD camera with the following conditions; 400 fps at the electrolysis duration of 1200 s. In Figure 2.8, the black-colored dotted surface is the micro-patterned electrode surface, and the white-colored sphere attached to the surface is an evolved hydrogen bubble by HER. Moreover, the bubbles' diameter stayed on the electrode surface was determined, and the distribution of the bubble diameter was investigated by analyzing the *in situ* optical images shown in Figure 2.8 by employing the image processing and analysis software (ImageJ).

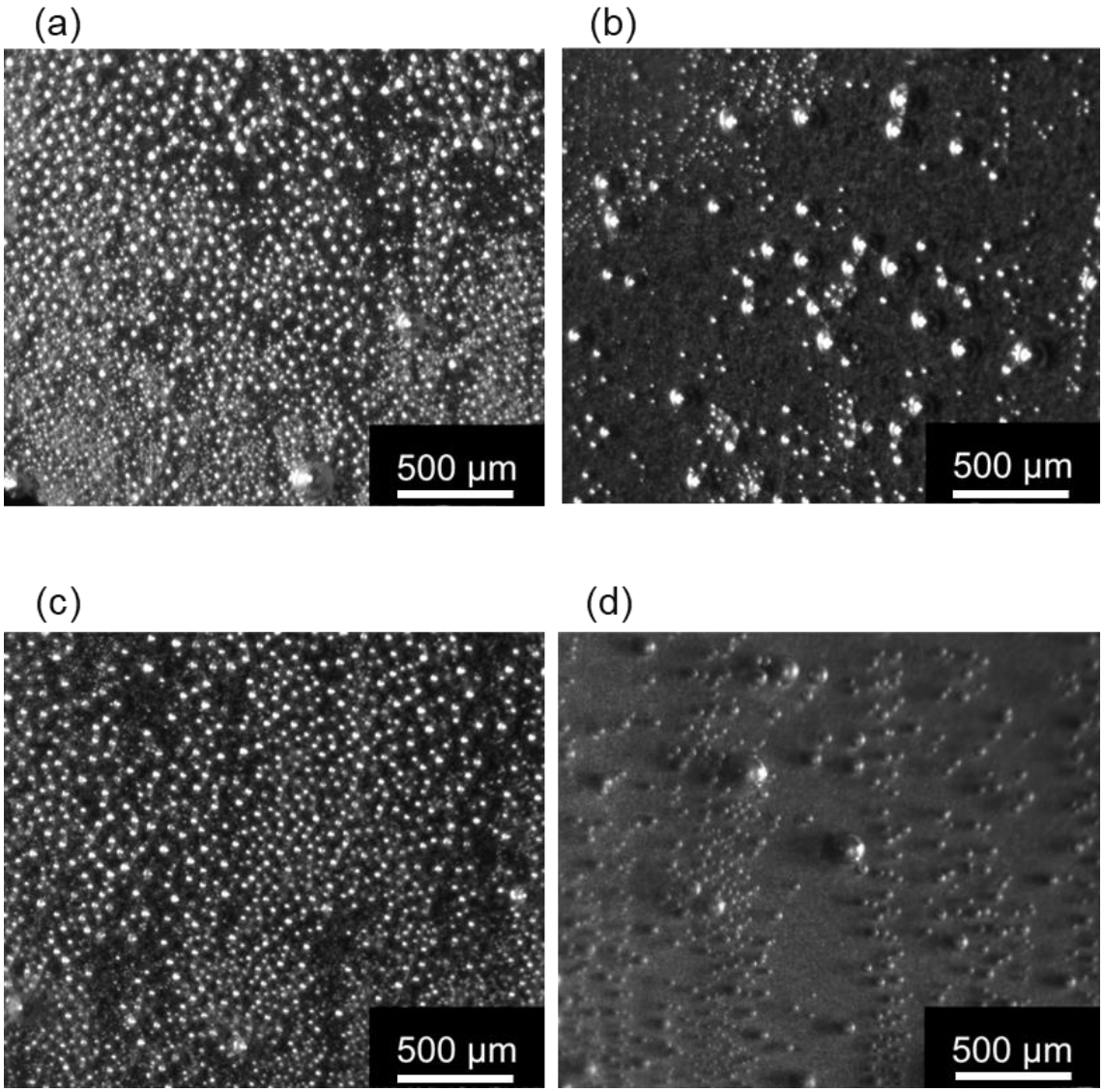

Figure 2.8 Representative *in situ* optical images on the electrode surface during the electrolysis (−20 mA cm^{-2} at 20 min): electrodes with (a) cylindrical microarray, Ni coverage 31.4 %, contact angle 74.6 °, (b) cylindrical microarray, Ni coverage 55.4 %, contact angle 71.5 °, (c) cylindrical microarray Ni coverage 39.9 %, contact angle 89.5 °, and (d) semispherical microarray Ni coverage 74.7 %, contact angle 112.5 °

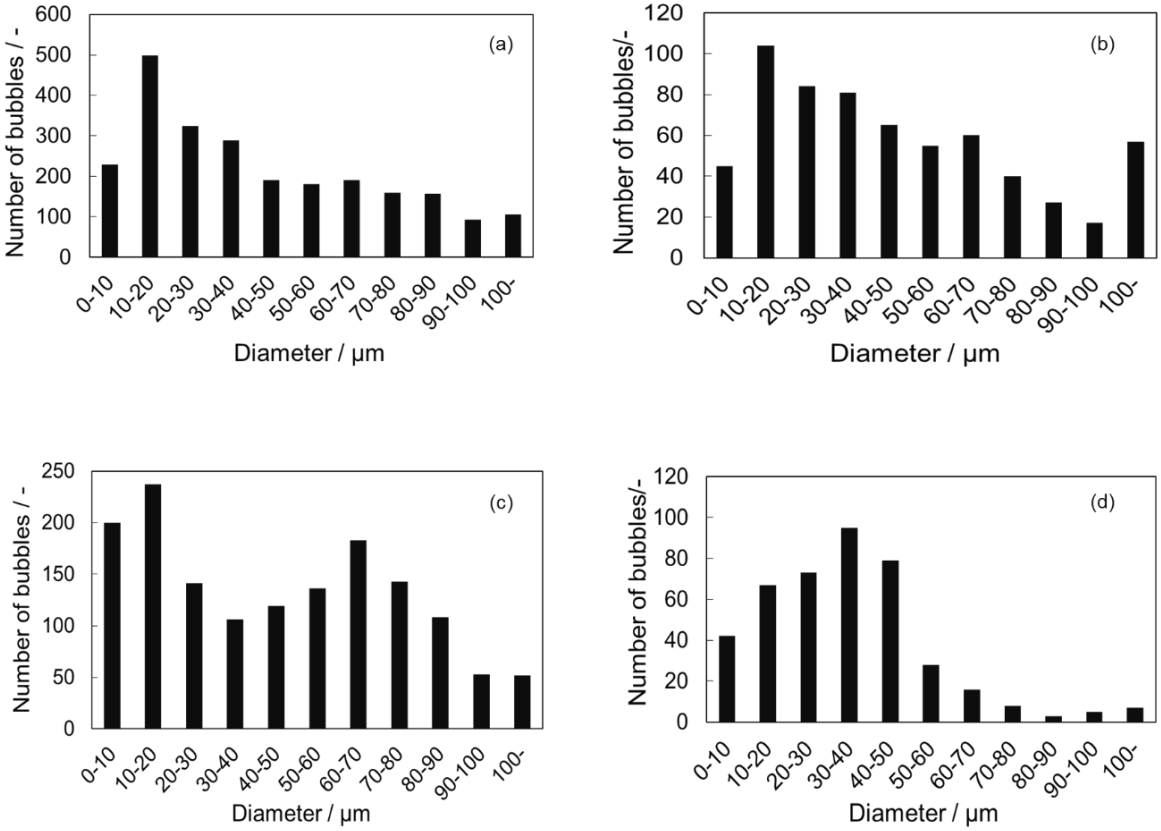

Figure 2.9 Diameter distribution of hydrogen bubbles on the electrode surface during the water electrolysis at 1200 s with different micro-patterned electrodes: (a) cylindrical microarray, Ni coverage 55.4 %, contact angle 74.6 °, (b) cylindrical microarray, Ni coverage 31.4 %, contact angle 71.5 °, (c) cylindrical microarray Ni coverage 39.9 %, contact angle 89.5 °, and (d) semispherical microarray Ni coverage 74.7 %, contact angle 112.5 °

Figure 2.9 shows the diameter distribution of the bubbles on the surface with the different micro-patterned electrodes of Figure 2.8. When the Ni coverage increased (comparing Figures 2.9 (a) and (b)), the mode diameter of the bubble exhibits the same value regardless of changing the Ni coverage. On the other hand, the higher Ni coverage surface increases the ratio of larger bubbles whose diameter is more than 60 μm. This behavior indicates that the electrode with high Ni coverage would accelerate the bubble growth and/or aggregation, causing preventing H_2O from access the reaction sites for HER [34] and changing the current distribution to the electrode surface [6]. A similar tendency is

observed in the case of the diameter distributions with different surface wettability (Figure 2.9(a) and (c)). The mode diameter of bubbles on the surface does not change dramatically. However, the bubbles with a diameter larger than 60 μm increase when the contact angle increased. This result also indicates that the electrode surface with lower wettability could stabilize bubbles on the surface, which enhances the bubble growth on the surface. The coincidence of the behaviors in comparing the Ni coverage in the low-value region (< 40 %) and the surface wettability could be explained by the correlation between the Ni coverage and the contact angle shown in Figure 2.3(a). In contrast, the different behaviors were confirmed in the case of changing the microdot structures. Figures 2.9(a) and (d) show that the mode diameter of bubbles on the surface increased as the microdot structure was transformed from cylindrical to semispherical. However, the ratio of the bubbles larger than 70 μm in diameter significantly decreased on the semispherical micro-patterned electrode. This observation suggests that the small bubbles are stabilized and tend to grow on the semispherical microarray surface in the early stage of bubble growth. The larger bubble has more contact points to the electrode, but the area of each contact point decreases by increasing the curvature of the bubble itself. In addition, the interface between the hydrogen bubble and the electrolyte also increases, which increases the repulsion of the negatively charged bubble surface to the electrolyte [35]. Consequently, the stability of the larger bubbles on the semispherical microdots is destabilized [29, 33]. This behavior could be one of the possible mechanisms to enhance detaching the larger bubbles from the electrode surface composed of semispherical microdots.

For further analyses of the bubble adsorption and detachment behaviors on the micro-patterned surface, the *in situ* bubble behavior observation from the horizontal viewpoint on the different microarray was performed. Figure 2.10 shows the representative images captured on the electrode surface during the observation. The *in situ* observation was carried out under the galvanostatic electrolysis at −20 mA cm^{-2}.

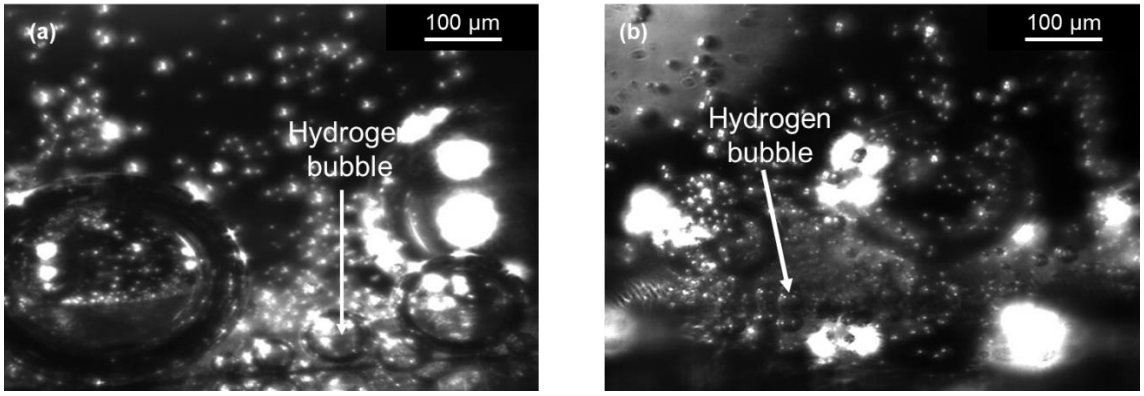

Figure 2.10 Representative images of *in situ* bubble behavior observation on the surface during the electrolysis (a) cylindrical and (b) semispherical microdots

Figure 2.10 observed that evolved bubbles stayed not on the top flat area of the microdots but among them. After that, bubbles slowly grew to some extent preferentially on the margin area of the microdots instead of the upper flat area. This phenomenon was independent of the microdot structures. From this observation, it is indicated that not only the structure of the microdot itself but also the sidewall and the height of the microdot contribute to the bubble behavior during the electrolysis. Moreover, the bubble attachment behavior to the microdot was analyzed. Comparing Figure 2.10(a) and (b), it is indicative that the interface between the bubble and the microdot seems to become smaller from on the cylindrical to on the semispherical microdots. This observation would be supportive to the analysis of bubble diameter distribution in Figure 2.9(d).

From the analyses mentioned above, it is suggested that modification of the microdot structures and surface wettability suppresses the larger bubbles' unfavorable stay on the electrode surface, which can realize that bubbles detach from the surface with smaller diameters. This effect may improve the HER efficiency lowered by the effect of bubbles and bubble coverage on the electrode surface.

2.3.3. analysis of the effect of the microdot shape on bubble behavior

In order to analyze the effect of the height of the microdot, the other parameter that is suggested to affect the bubble behaviors in 2.3.2, Ni micro-patterned electrodes with the different microdot heights, were fabricated by controlling the thickness of the photoresist in the lithography process in Scheme 2.1. The aspect ratio, the ratio of height to the microdot diameter, was utilized as the parameter to evaluate the microdot height. The prepared micro-patterned electrodes with different aspect ratios are shown in Figure 2.11.

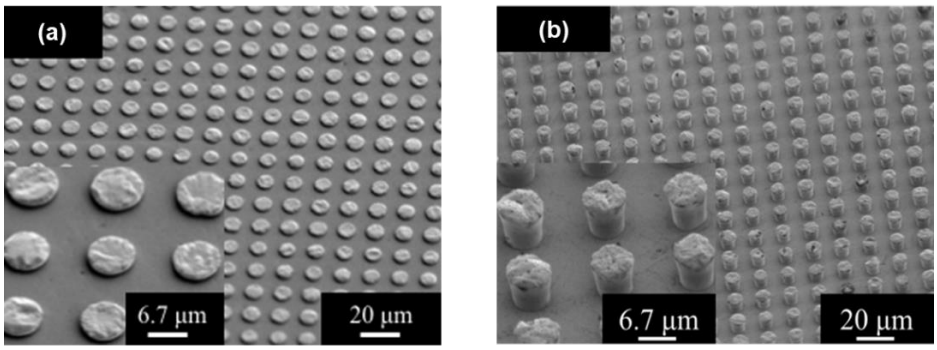

Figure 2.11 SEM images of the Ni micro-patterned electrodes with different aspect ratios: (a) low (0.3) and high (1.2). Inserted SEM images are the enlarged view of the microarrays.

From Figure 2.11, the microdots with a different height were successfully prepared, and uniform microdot formation without dependence on the substrate position was confirmed. The *in situ* bubble observation on the different aspects (low and high aspect) microdots were carried out. Figure 2.12 shows the representative *in situ* optical images of bubble behaviors on the low aspect (0.3) and the high aspect (1.2) micro-patterned electrodes.

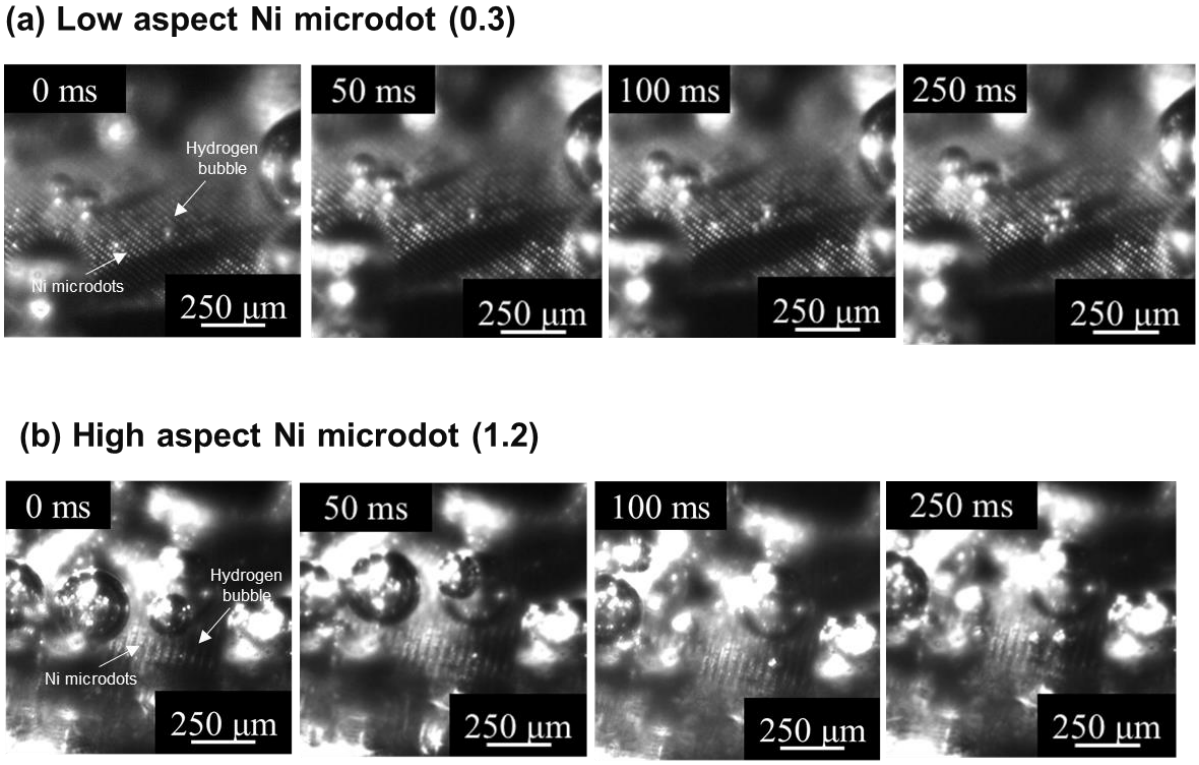

Figure 2.12 Representative *in situ* optical images of the bubble nucleation and growth behavior on (a) the low aspect (0.3) and (b) the high aspect (1.2) during the galvanostatic electrolysis (−20 mA cm^{-2}) at 1200 s

In Figure 2.12(a), a hydrogen bubble appeared on the top flat region of the microdot rather than between the microdots. After that, a bubble grew on the top flat regions and attached to the multiple microdots when the bubble's size was large enough to cover the multiple microdots due to increasing the interface between the bubble and the electrode that contributed to the smaller surface energy. On the other hand, a different phenomenon was observed on the high aspect micro-patterned electrode. In Figure 2.12(b), a hydrogen bubble first evolved on the sidewall region of the microdot rather than the upper flat area of the microdot like in Figure 2.12(a). After that, the bubble grew between the microdots to become large enough to move to the other site with more room to grow. Subsequently, the bubble transferred from the sidewall to the top surface to grow larger, finally detaching from the flat top surface of the microdot. Previous studies have indicated that the defect-like micro-structures behave as the bubble nucleation sites [36-38] due to lower interaction between the bubble and the electrolyte [33]. It is also indicated that bubble

nucleation and growth processes occur in different microdot locations. This difference suggests that it was easy to evolve bubbles [39, 40]. The *in situ* bubble behavior observation from the vertical direction to the substrate was performed to further analyze the bubble nucleation behaviors on the high aspect micro-patterned electrode, as shown in Figure 2. 13.

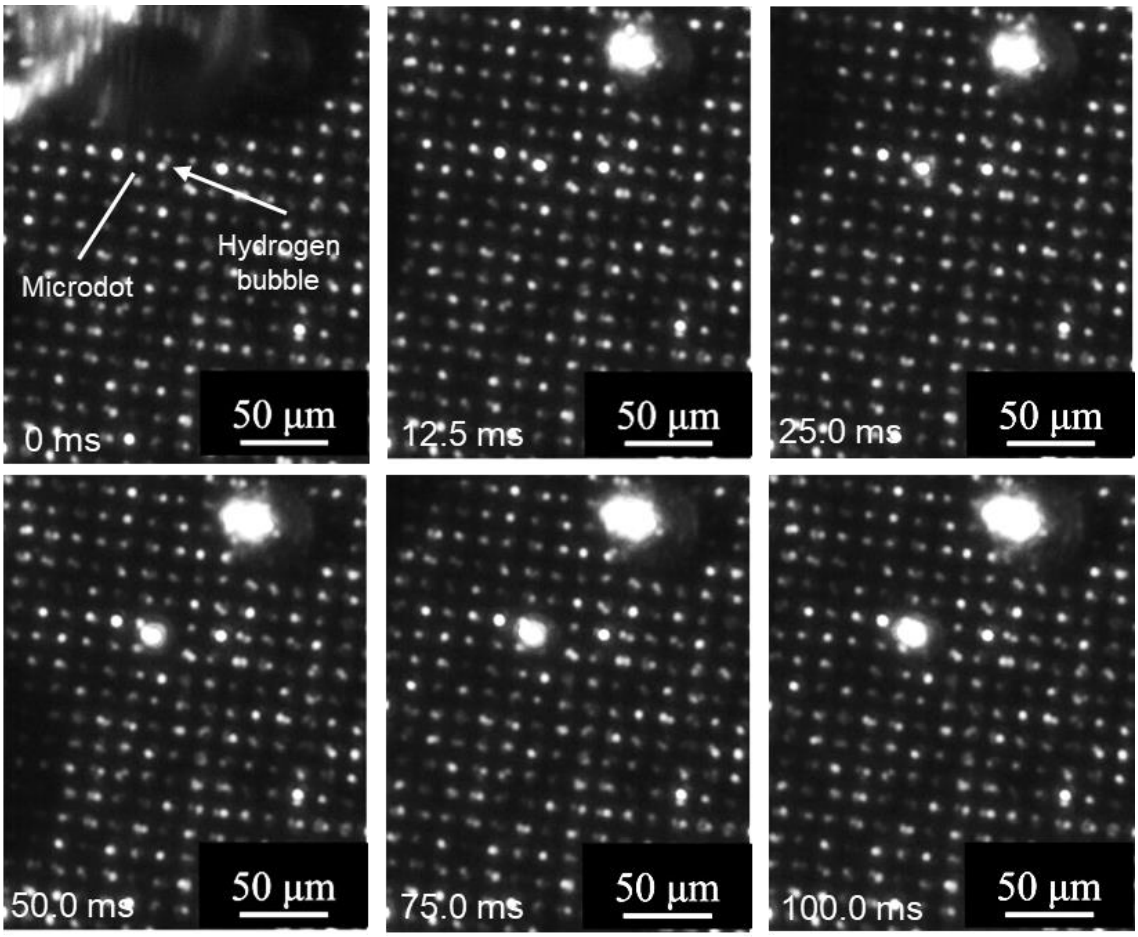

Figure 2.13 Representative in situ optical images on high aspect micro-patterned electrodes from the vertical viewpoint during the galvanostatic electrolysis (at −10 mA cm^{-2}, for 30 min)

In Figure 2.13, a hydrogen bubble evolved among the microdots rather than on the flat top surface of the microdot, as described in Figure 2.12(b). This observation indicates that the sidewall similarly behaves as the void-like structures in the bubble formation [37, 38]. It is suggested that bubbles tend to grow on the microdot's sidewall [37] due to the larger

sidewall surface of the high aspect microdot, which causes the enhancement of bubble growth and easy detachment from these structures to minimize its surface area [41]. This behavior can be necessary to suppress the overpotential increase for HER.

From these results obtained by the analyses using the micro-patterned electrodes, the bubble behaviors on the micro-patterned structures are suggested in Figure 2.14.

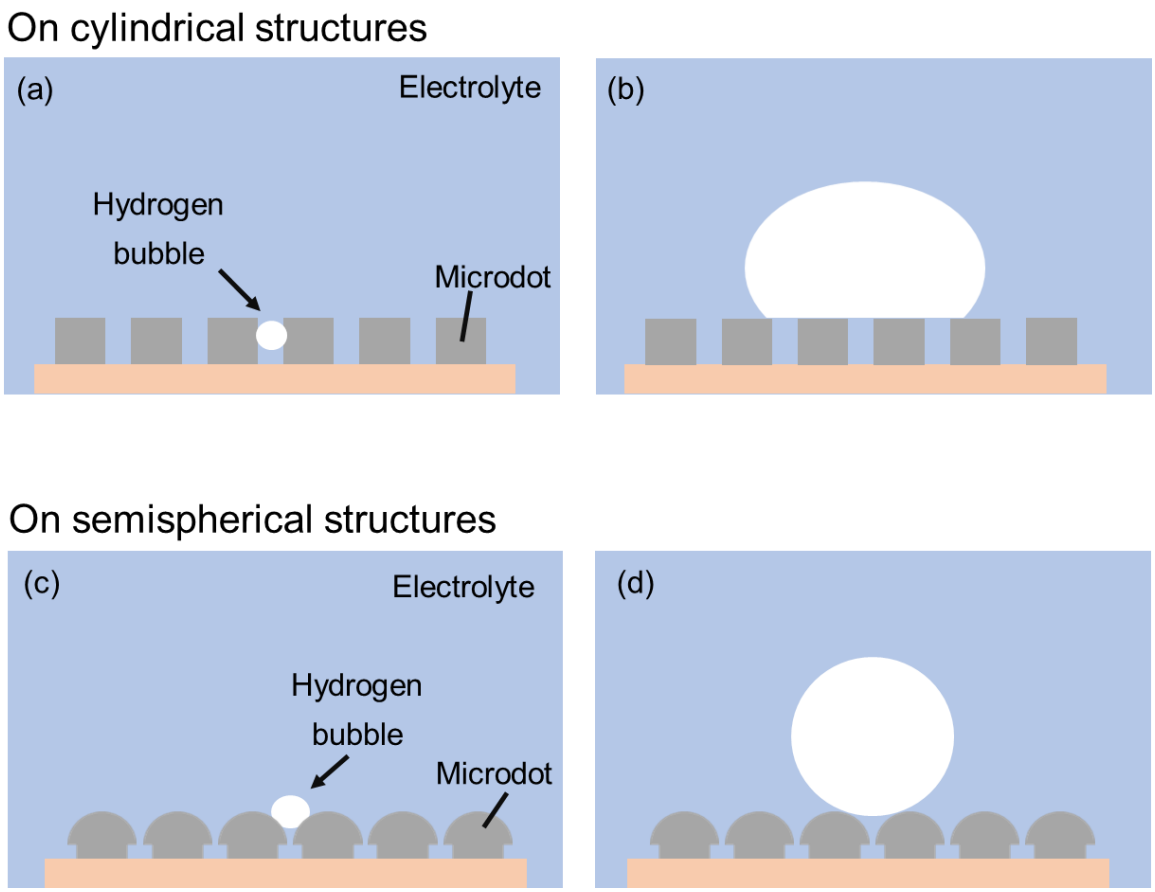

Figure 2.14 Schematic mechanisms of suggested bubble behaviors on cylindrical and semispherical microarray surfaces: (a) bubble nucleation and (b) bubble growth on cylindrical microdots, (c) bubble nucleation, and (d) bubble growth on semispherical microdots

In Figure 2.14(a) and (b), on cylindrical microdots, a bubble evolves on the sidewall and grows to some extent among the microdots by the interaction between the bubble and microdot [34]. Whereafter, the bubble moves and grows on the top area of the microdot until detachment from the surface. The large top flat surface stabilizes bubble adsorption

on the cylindrical microdots. However, this effect can weaken on the larger microdot surface, such as larger diameter than bubbles size, because bubble nucleation and growth can proceed on a single microdot surface. When the effect of the surface area is considered, approximately 5 to 10 μm may be suitable to maintain the number of reaction sites for HER and avoid the bubbles' negative effect.

Similarly, a hydrogen bubble first evolves between the spherical structures of the microdot that behave the nucleation sites of bubbles and grows onto the top flat region of the microdots (as shown in Figure 2.14(c) and (d)). When the bubble grows large, the bubble-microdot interface decreases, and the bubble-electrolyte interface increases. Consequently, the bubble can be destabilized on the surface and is easy to detach with a smaller size, as observed in Figure 2.9(d). From these suggested mechanisms, it can be concluded that the surface area of the sidewall to accelerate the bubble nucleation and the early stage of the bubble growth. In addition, the relatively sharp structures such as semispherical and dendritic structures smaller than tens of micrometer are vital factors to enhance the supply of H_2O, the reactant of HER, with higher efficiency by enhancing bubble detachme caused by the small bubble-electrode interface.

2.4. Conclusion

In chapter 2, the bubble behaviors on the microtextured surface during HER was investigated using the Ni micro-patterned electrodes with different parameters to analyze the effect of surface microstructures and wettability controlled by them on bubble nucleation and growth behavior. Prior to the analyses, Ni micro-patterned electrodes that can control the surface wettability by modifying the parameters were successfully fabricated by lithography and electrodeposition. The electrochemical measurements confirmed that the electrode with lower wettability increased the overpotential value to proceed with the following reaction, indicating that bubble growth and/or aggregation affected the lower HER efficiency. *In situ* observation of the bubble behavior and analysis of diameter distribution on the surface revealed that larger bubbles were generated on the low wettability surface, and the microdot structure influenced the bubble detachment. Moreover, *in situ* bubble behavior observation on the different height's microdot indicated that the sidewall behaves as the bubble evolution sites, and bubble nucleation and growth processes proceed on the different sites in the case of the high aspect microarray.

From the collective results, controlling the bubble-electrode interface by microstructure modification suppresses the bubble growth and improves bubble detachment, which enhances the following HER and access of H_2O to the reaction sites.

References

[1] S. Trasatti, Work Function, Electronegativity, and Electrochemical Behaviour of Metals III. Electrolytic hydrogen evolution in acid solutions, *J. Electroanal. Chem. Interfacial Electrochem.* **39** (1972) 163.

[2] Y. Yan, B. Xia, Z. Xu, X. Wang, Recent Development of Molybdenum Sulfides as Advanced Electrocatalysts for Hydrogen Evolution Reaction, *ACS Catal*. **4** (2014) 1693.

[3] Z. Chen, X. Duan, W. Wei, S. Wang, B. Ni, Recent advances in transition metal-based electrocatalysts for alkaline hydrogen evolution, *J. Mater. Chem. A* **7** (2019) 14971.

[4] X. Zou, Y. Zhang, Noble metal-free hydrogen evolution catalysts for water splitting, *Chem. Soc. Rev.* **44** (2015) 5148.

[5] W. Zhou, J. Jia, J. Lu, L. Yang, D. Hou, G. Li, S. Chen, Recent developments of carbon-based electrocatalysts for hydrogen evolution reaction, *Nano Energy* **28** (2016) 29.

[6] P. J. Sides, C. W. Tobias, Resistance of a Planar Array of Spheres: Gas Bubbles on Electrode, *J. Electrochem. Soc.* **129** (1982) 2715.

[7] H. Vogt, R. J. Balzer, The bubble coverage of gas-evolving electrodes in stagnant electrolytes, *Electrochim. Acta* **50** (2005) 2073.

[8] R. Wüthrich, C. Comninellis, H. Bleuler, Bubble evolution on vertical electrodes under extreme current densities, *Electrochim. Acta* **50** (2005) 5242.

[9] S. H. Ahn, S. J. Hwang, S.J. Yoo, I. Choi, H. J. Kim, J. H. Jang, S. W. Nam, T. Lim, T. Lim, S. Kim, J. J. Kim, Electrodeposited Ni dendrites with high activity and durability for hydrogen evolution reaction in alkaline water electrolysis, *J. Mater. Chem.* **22** (2012) 15153.

[10] X. Li, X. Hao, A. Abudula, G. Guan, Nanostructured catalysts for electrochemical water splitting: current state and prospects, *J. Mater. Chem. A* **4** (2016) 11973.

[11] K. Zeng, D. Zhang, Evaluating the effect of surface modifications on Ni based electrodes for alkaline water electrolysis, *Fuel* **114** (2014) 692.

[12] J. Yoshida, K. Kataoka, R. Horcajada, A. Nagaki, Modern Strategies in Electroorganic Synthesis, *Chem. Rev.* **108** (2008) 2265.

[13] Y. Li, H. Deng, J. E. Dick, A. J. Bard, Analyzing Benzene and Cyclohexane Emulsion Droplet Collisions on Ultramicroelectrodes, *Anal. Chem.* **87** (2015) 11013.

[14] M. Liu, Y. Zheng, J. Zhai, L. Jiang, Bioinspired Super-antiwetting Interfaces with Special Liquid-Solid Adhesion, *Acc. Chem. Res.* **43** (2009) 368.

[15] T. Darmanin, E. T. Gvenchy, S. Amigoni, F. Guittard, Superhydrophobic Surfaces by Electrochemical Processes, *Adv. Mater.* **25** (2013) 1378.

[16] B. Su, Y. Tian, L. Jiang, Bioinspired Interfaces with Superwettability: From Materials to Chemistry, *J. Am. Chem. Soc.* **138** (2016) 1727.

[17] L. Wang, F. Xiao, The Importance of Catalyst Wettability, *ChemCatChem* **6** (2014) 3048.

[18] G. B. Darband, M. Aliofkhazraei, S. Shanmugam, Recent advances in methods and technologies for enhancing bubble detachment during electrochemical water splitting, *Renewable Sustainable Energy Rev.* **114** (2019) 109300.

[19] Y. Li, H. Zhang, T. Xu, Z. Lu, X. Wu, P. Wan, X. Sun, L. Jiang, Under-Water Superaerophobic Pine-Shaped Pt Nanoarray Electrode for Ultrahigh-Performance Hydrogen Evolution, *Adv. Funct. Mater.* **25** (2015) 1737.

[20] Gh. B. Darband, M. Aliofkhazraei, A. S. Rouhaghdam, Three-dimensional porous Ni-CNT composite nanocones as high performance electrocatalysts for hydrogen evolution reaction, *J. Electroanal. Chem.* **829** (2018) 194.

[21] J. Bico, C. Tordeux, D. Quere, Rough wetting, *Europhys. Lett.* **55** (2001) 214.

[22] J. Bico, U. Rhiele, D. Quere, Wetting of textured surface, *Colloids Surf. A* **206** (2002) 41.

[23] W. Choi, A. Tuteja, J. M. Mabry, R. E. Cohen, G. H. McKinley, A modified Cassie-Baxter relationship to explain contact angle hysteresis and anisotropy on non-wetting textured surfaces, *J. Colloid Interface Sci.* **339** (2009) 208.

[24] R. L. ReLoy, Industrial Water Electrolysis: Present and Future, *Int. J. Hydrogen Energy* **8** (1983) 401.

[25] N. Guillet, P. Millet, Hydrogen Production: By electrolysis, in: A. Gidula, D. Stolten (Eds.), Wiley, Hoboken, 2015.

[26] K. Ota, H. Minoshima, Denkai ni yoru Suisoseizou, *Electrochemistry* **71**(4) 2003 274.

[27] A. Checco, T. Hofmann, E. DiMasi, C. T. Black, B. M. Ocko, Morphology of Air Nanobubbles Trapped at Hydrophobic Nanopatterned Surfaces, *Nano Lett.* **10** (2010) 1354.

[28] A. B. D. Cassie, S. Baxter, Wettability of Porous Surfaces, *Trans. Faraday Soc.* **50** (1944) 546.

[29] N. A. Patankar, Transition between Superhydrophobic States on Rough Surfaces, *Langmuir* **20** (2004) 7097.

[30] N. J. Shirtcliffe, G. McHale, M. I. Newton, C. C. Perry, Wetting and Wetting Transitions on Copper-Based Super-Hydrophobic Surfaces, *Langmuir* **21** (2005) 937.

[31] A. Kietzig, S. G. Hatzikiriakos, P. Englezos, Patterned Superphydrophobic Metallic Surfaces, *Langmuir* **25** (2009) 4821.

[32] K. Zeng, D. Zhang, Recent progress in alkaline water electrolysis for hydrogen production and applications, *Prog. Energy Combust. Sci.* **36** (2010) 307.

[33] D.J. Wesley, R.M. Smith, W.B. Zimmerman, J.R. Howse, Influence of surface wettability on microbubble formation, *Langmuir* **32** (2016) 1269.

[34] S. T. Yohe, Y. L. Colson, M. W. Grinstaff, Superhydrophobic Materials for Tunable Drug Release: Using Displacement of Air to Control Delivery Rates, *J. Am. Chem. Soc.* **134** (2012) 2016.

[35] N. P. Brandon, G. H. Kelsall, S. Leveni, A. L. Smith, Interfacial electrical properties of electrogenerated bubbles, *J. Appl. Electrochem.* **15** (1985) 485.

[36] L. Dong, X. Quan, P. Cheng, An analysis of surface-microstructures effects on heterogeneous nucleation in pool boiling, *Int. J. Heat Mass Transfer* **55** (2012) 4376.

[37] A. Giacomello, M. Chinappi, S. Meloni, C. M. Casciola, Geometry as a Catalyst: How Vapor Cavities Nucleate from Defects, *Langmuir* **29** (2013) 14873.

[38] A. Giacomello, S. Meloni, M. Chinappi, C. M. Casciola, Cassie−Baxter and Wenzel States on a Nanostructured Surface: Phase Diagram, Metastabilities, and Transition Mechanism by Atomistic Free Energy Calculations, *Langmuir* **28** (2012) 10764.

[39] X. Yang, D. Baczyzmalski, C. Cierpka, G. Mutschke, K. Eckert, Marangoni convection at electrogenerated hydrogen bubbles, *Phys. Chem. Chem. Phys.* **20** (2018)

[40] J. Dukovic, C. W. Tobias, The Influence of Attached Bubbles on Potential Drop and Current Distribution at Gas-Evolving Electrodes, *J. Electrochem. Soc.* **134** (1987) 331.

[41] G. Sakuma, Y. Fukunaka, H. Matsushima, Nucleation and growth of electrolytic gas bubbles under microgravity, Int. *J. Hydrog. Energy* **39** (2014) 7638.

Chapter 3:

The Effect of Surface Microstructures on the Bubble Behaviors

3.1. Introduction

As described in Chapter 2, one of the important factors influencing the bubble behaviors on the electrode surface is the micro-scale structures and surface wettability modified by these structures. The effect of the microstructures on bubble behaviors was analyzed using the micro-patterned electrodes. Although the micro-patterned structure affected the bubble behaviors directly in chapter 2, one microdot is also composed of lots of relatively smaller-scale characteristics that influence HER and the following bubble nucleation growth behaviors, such as nano-scale structures [1, 2], roughness derived from nanostructures [3, 4], and crystal orientation [5]. In order to control the bubble behaviors on the surface for improving HER efficiency, not only the micro-scale structures such as the microdots but also these nano-scale parameters are necessary to be controlled.

Among these factors, the crystalline facet is one of the most important factors to control HER and the following bubble behaviors. Many studies have focused on the effect of crystalline facet on the catalytic performance of HER. Especially, previous studies focused on not only the activity of HER [6, 7] but also the adsorption of hydrogen atoms on the surface [7, 8]. N. M. Marković a et al. have indicated that the HER activity on the Pt surface with different crystalline facets was varied by changing the adsorption behaviors of OH^- on each crystalline surface [6]. K. A. Jaaf-Golze et al. also have reported that the adsorption behaviors of ions were changed on the single crystalline surface (called such as microfacet) [8]. Although these features reported in previous studies affect the bubble behaviors on the surface, few studies focus on the direct effect of the existence of the well-defined surface like the microfacet in the electrode on the bubble behavior during water electrolysis. The details have not been fully elucidated.

This chapter aims to investigate the direct effect of the single crystalline facet on evolved bubbles. The bubble behaviors on Pt (111) microfacet electrode fabricated by the Clavilier method [9] were analyzed by *in situ* bubble behavior observation. Moreover, the effect of the microfacet on the bubble behaviors and the HER efficiency was investigated by the combination of the electrochemical measurements and *in situ* observation of bubble behaviors on the electrode surface. From the results obtained from the *in situ*

analyses, the bubble nucleation and growth behaviors on the electrode surface with (111) microfacet is discussed.

3.2. Experimental

3.2.1. Fabrication of Pt (111) microfacet electrodes

The Pt (111) microfacet electrode was fabricated by hydrogen-oxygen flame annealing, called the Clavilier method [9]. Before annealing by hydrogen-oxygen flame, Pt wire (5 cm 0.4 mmφ 99.98%, Nilaco) was immersed into the solution containing 25 mL of 61 % Nitric acid (EL grade, Kanto Chemical Co.), 25 mL 96 % Sulfuric acid (EL grade, Kanto Chemical Co.), and 50 mL ultra-pure water for 5 min to remove the impurities from the surface of Pt wire. After that, the Pt wire was rinsed with ultra-pure water and dried with N_2 gas.

The cleaned Pt wire was annealed by the hydrogen-oxygen flame from the torch with the hydrogen-oxygen gas generator (Sunwelder, San Well Co. Ltd.). First, one end of Pt wire was melted by approaching the flame to fabricate a bead structure in diameter of approximately 2.0 mm. After that, a Pt bead was exposed to the flame for 5 min to maintain the interface between the melt area and solid area illustrated in Figure 3.1.

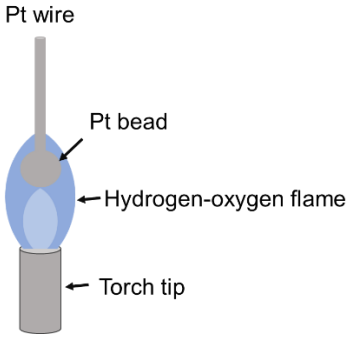

Figure 3.1 Schematic image of the Clavilier method
(hydrogen-oxygen flame annealing process)

After 5 min annealing, the Pt bead was kept away from the flame slowly to move the solid-melt liquid interface on the bead slowly. The Pt bead removed from the flame was cooled in the ambient condition for 30 s and immersed into ultra-pure water to avoid the

effect of the impurities.

In this analysis, (111) microfacet was employed as the model surface in order to analyze the effect of the microfacet on bubble behaviors. The (111) microfacet is one of the most stable crystalline facets [7]. Moreover, many researchers have focused on the electrochemical behaviors on (111) microfacet [8, 10]. Hence, this (111) microfacet may be suitable for the model microfacet surface to observe the bubble behaviors for longer durations, such as for 30 min.

Surface morphologies of the fabricated Pt (111) microfacet electrode were observed by an optical microscope (CK-30, Olympus, or IX-70, Olympus).

3.2.2. Analysis of bubble behaviors on Pt (111) microfacet electrode

All the electrochemical measurements were carried out by an electrochemical analyzer (HZ-Pro, Hokuto Denko Co.) or a potentiostat (RDE 3, Pine Instruments Co.) with a Data acquisition card (USB-6009, National Instruments). For the electrochemical measurements, the three-electrode system consisting of the prepared Pt (111) microfacet electrode as the working electrode, a carbon rod (3.0 mmφ, >99.99%, Nilaco) as the counter electrode, and the Ag/AgCl electrode or the homemade Pt wire reverse hydrogen electrode (RHE) as the reference electrode. A schematic image of the electrochemical measurement setup is shown in Figure 3.2. Figure 3.3 shows the homemade Pt RHE employed in the experiments.

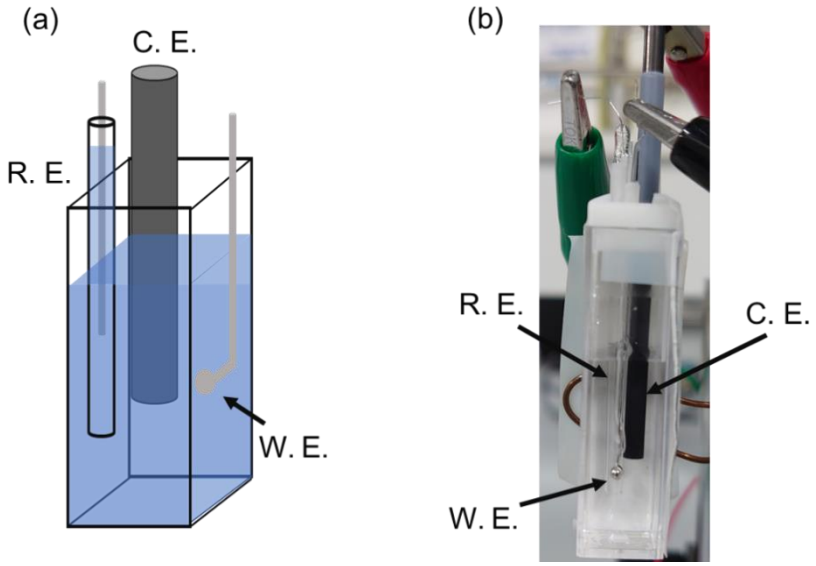

Figure 3.2 The electrochemical measurement cell: (a) schematic image and (b) picture of the measurement cell

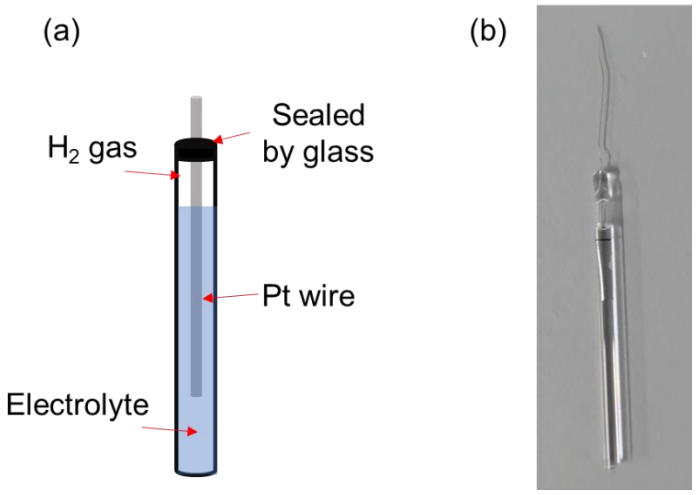

Figure 3.3 The homemade Pt RHE: (a) schematic image and (b) picture of prepared Pt RHE

When the homemade Pt RHE is used, the electrolysis is necessary to maintain hydrogen gas inside the electrode, as Figure 3.2(a) before the electrochemical measurements. This pre-electrolysis for the reference electrode was carried out with a simple two-electrodes system composed of Pt RHE and Carbon rod as the working and counter electrodes. The

voltage was applied at 5.0 V for 180 s by the electrochemical analyzer. The electrolyte was 0.1 mol dm^{-3} H_2SO_4 solution prepared by diluting 96 wt% H_2SO_4 solutions (EL grade, Kanto Chemical Co.) with ultra-pure water. Prior to the measurements, the 0.1 mol dm^{-3} H_2SO_4 solution was purged by N_2 gas for 20 min to remove the dissolved oxygen in the electrolyte. The electrochemical measurement conditions are shown in Table 3.1.

Table 3.1 Electrochemical measurement conditions

W. E.	Prepared Pt microelectrode
C. E.	Carbon rod
R. E.	Pt reversible hydrogen electrode (RHE)
Electrolyte	0.1 M H_2SO_4
Deaeretion	N_2 gas
Temperature	R. T.

Cyclic voltammetry (CV) of Pt (111) microfacet electrode in 0.1 mol dm^{-3} H_2SO_4 solution was performed by sweeping the potential from −200 mV vs. RHE to 600 mV vs. RHE with a scan rate of 300 mV s^{-1} to observe the bubble nucleation and growth behaviors on (111) microfacet. The galvanostatic electrolysis was also performed at −20 or −40 mA cm^{-2} to analyze the bubble behaviors on the electrode surface.

In order to analyze the bubble behaviors on the electrode surface with (111) microfacet, *in situ* observation of bubble behaviors was performed using a high-speed CCD camera (HAS-U2, DITECT Corp.) installed with a macro zoom lens (VSZ-0745, VS Technology) or a microscope (CK-40, Olympus) with a CCD camera (MU-1000, AmScope). The frame rate of the CCD camera was set as 60 fps.

3.3. Results & Discussion

3.3.1. Analysis of bubble behavior on (111) microfacet

The Pt (111) microfacet was fabricated by hydrogen-oxygen flame annealing. The surface of the prepared Pt (111) microfacet was observed by the optical microscope, as shown in Figure 3.4.

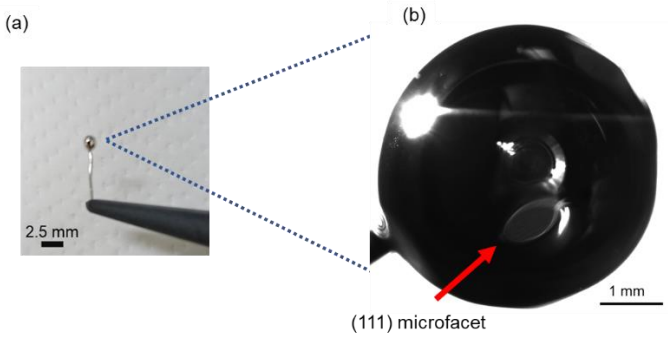

Figure 3.4 Optical images of prepared Pt (111) microfacet electrode:
(a) the whole view of Pt electrode and (b) enlarged view of Pt sphere

From Figure 3.4, a circle-like flat region (pointed by the red arrow in Figure 3.4(b)) randomly appeared on the surface of the Pt bead. Previous studies have indicated that the circle-like (111) microfacet is formed by annealing the Pt bead due to the stable crystalline facet approximately the melting point of Pt [9, 11]. Based on this, it was confirmed that Pt microelectrode with (111) microfacet is successfully prepared. On the (111) microfacet, the size of the (111) microfacet was approximately 50 to several hundred μm diameter. In the following parts, these Pt (111) microfacet electrodes were employed.

First, to investigate the bubble nucleation and growth behaviors on (111) microfacet and the other area of the Pt electrode, cyclic voltammetry measurements of Pt (111) microfacet electrode in 0.1 mol dm^{-3} H_2SO_4 was carried out by sweeping from −200 mV to 600 mV (vs. RHE). The measured cyclic voltammogram is shown in Figure 3.5.

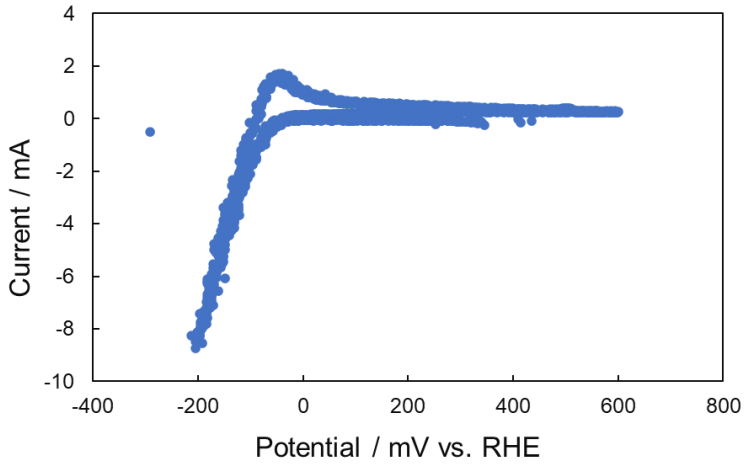

Figure 3.5 Cyclic voltammogram of Pt (111) microfacet electrode in 0.1 mol dm^{-3} H_2SO_4 solution (Potential range: −200 mV to 600 mV vs. RHE, Scan rate: 300 mV s^{-1})

The CV in Figure 3.5 shows the current rapidly increases below approximately − 50 mV vs. RHE in the negative scan. The oxidation peak appears in −200 to −100 mV in the positive scan. This peak is suggested to be derived from the oxidation of hydrogen adsorbed on the electrode surface [12]. These results demonstrate that the prepared Pt (111) microfacet electrode functioned as the catalytic electrode of HER.

During this CV measurement, *in situ* bubble behavior observation was carried out to analyze bubble nucleation and growth behavior on (111) microfacet surface. The representative images of *in situ* bubble observation are shown in Figure 3.6.

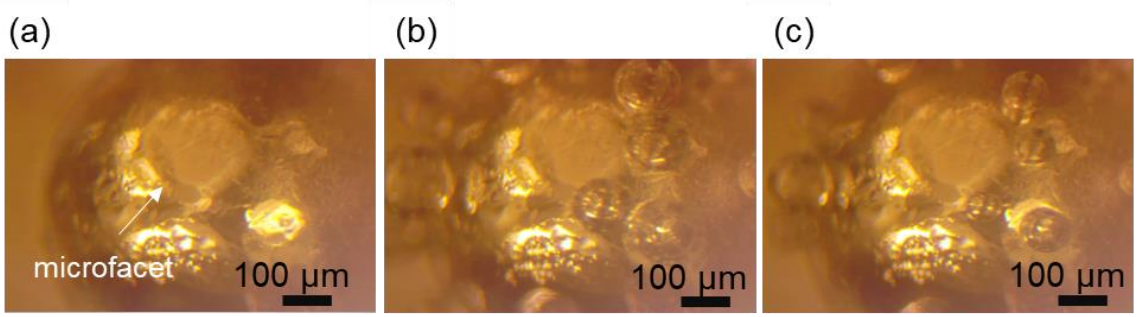

Figure 3.6 Representative images of *in situ* bubble observation on Pt (111) microfacet electrodes: (a) around 0 mV, (b) around −200 mV in the negative scan, and (c) around 0 mV in the positive scan (vs. RHE)

From this *in situ* observation result, Hydrogen bubbles were generated on the (111) microfacet in the negative scan, and the diameter of bubbles decreased as the potential was swept positively. Bubble evolution seemed to occur at the relatively rough sites on the Pt surface except for (111) microfacet. On the other hand, no hydrogen bubbles were observed on the (111) microfacet region in the potential range from −200 mV to 600 mV vs. RHE. The previous study indicated that (111) facet of Pt exhibits relatively lower HER activity than that of other facets and surfaces [5, 6]. Furthermore, the roughness of microfacet was small than other structures such as amorphous surfaces by the previous studies [9, 13]. From these characteristics of (111) microfacet obtained from the previous studies and the experimental results, it is suggested that the lower concentration of dissolved H_2 caused by lower HER activity and the smaller nano-scale roughness of (111) microfacet [3] influence the bubble nucleation process on the microfacet.

In order to further analyze the effect of the applied potential on the bubble nucleation and growth behaviors on (111) microfacet, CV with the more negative potential range was carried out by seeping the range from −400 mV to 600 mV vs. RHE. The obtained cyclic voltammogram is shown in Figure 3.7.

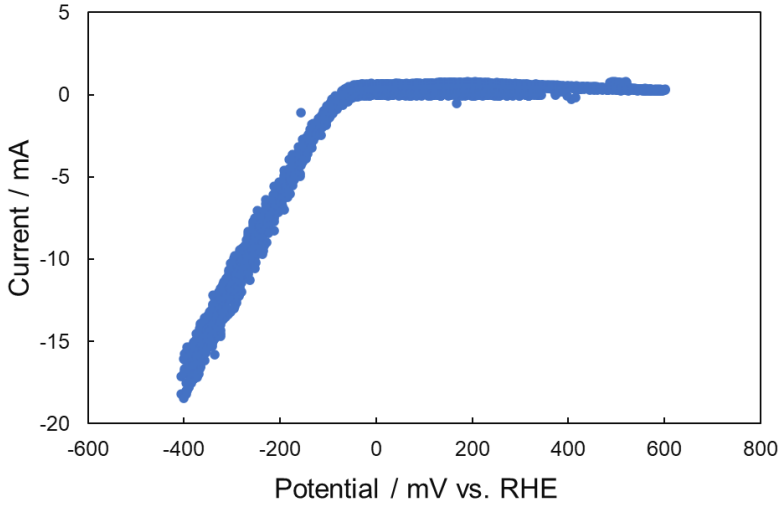

Figure 3.7 Cyclic voltammogram of Pt (111) microfacet electrode in 0.1 mol dm^{-3} H_2SO_4 solution (Potential range: −400 mV to 600 mV vs. RHE, Scan rate: 300 mV s^{-1})

During the CV measurement, in situ observation of bubble behaviors on the electrode

surface was also performed to analyze the effect of the microfacet on bubble behaviors. The representative images of in situ observation are shown in Figure 3.8.

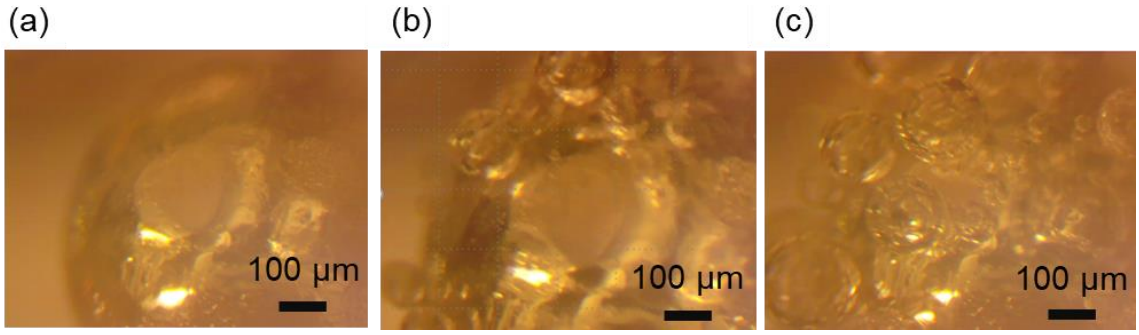

Figure 3.8 The representative images of *in situ* bubble observation on Pt (111) microfacet electrodes: (a) around 0 mV, (b) around −200 mV, and (c) around −400 mV in the positive scan (vs. RHE)

From Figure 3.7, the current increase derived from HER is observed approximately at −50 mV vs. RHE, as same as Figure 3.5. From the corresponding *in situ* observation result in Figure 3.8, it is observed that no bubble is generated on the (111) microfacet as the potential is swept to −200 mV vs. RHE in the negative scan. However, bubble generation is observed on (111) microfacet when the potential more negative than −200 mV vs. RHE is applied, as shown in Figure 3.8 (c). This observation result indicates that bubble formation on (111) microfacet proceed due to increasing the concentration of dissolved H_2 in the solution upon the microfacet by applying overpotential. Compared with the results in the different potential ranges, it is suggested that not only the well-defined structure but also lower HER activity derived from the crystalline facet affect the bubble behaviors, especially bubble nucleation behaviors during the electrolysis.

3.3.2. Analysis of the effect of (111) microfacet on bubble behaviors and the efficiency of HER

In order to further analyze the effect of the existence of (111) microfacet on bubble behaviors during HER, the galvanostatic electrolysis at−20 mA cm^{-2} was carried out using the (111) microfacet electrodes. In this analysis, two Pt (111) microfacet electrodes were prepared: one is the Pt microelectrode with more than 4 microfacets on the surface (named as Pt microelectrode with more microfacet), the other is the Pt microelectrode with fewer than 3 microfacets on the surface (named as the Pt microelectrode with less microfacet). These electrodes were selected to modify the similar conditions of the microdot in chapter 2 that has the edge-like structures on the random positions. Figure 3.9 shows the potential profile of Pt microelectrodes with more and less microfacet.

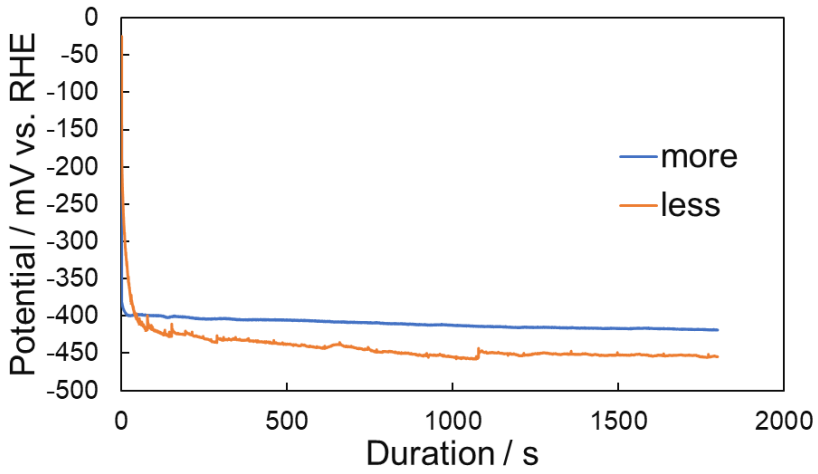

Figure 3.9 Potential profiles of Pt (111) microfacet electrodes with different number of microfacet at −20 mA cm^{-2}

The *in situ* observation of bubble behaviors on the electrode surface was also carried out. Figure 3.10 and 3.11 are the optical images of *in situ* observation results of a duration of 1200 s on the surface of Pt microelectrode with more microfacet and less microfacet.

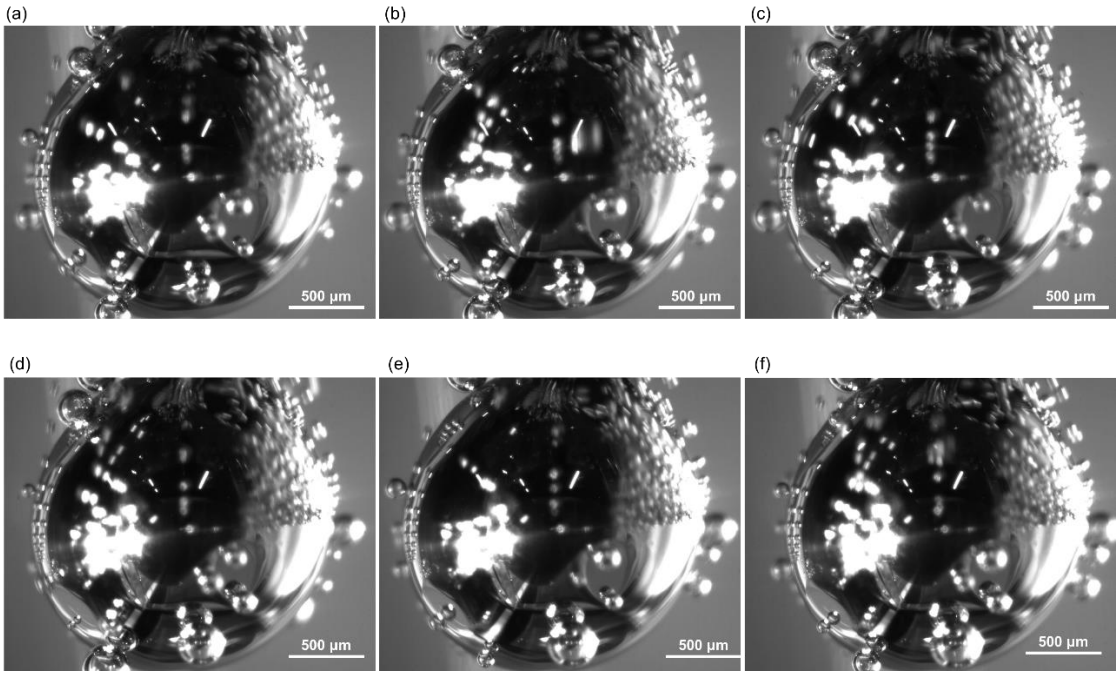

Figure 3.10 Optical images of *in situ* bubble behavior observation on Pt microfacet with more microfacet at 1200 s: (a) 0 s, (b) 0.50 s, (c) 1.0 s, (d) 1.5 s, (e)2.0 s, and (f) 2.5 s

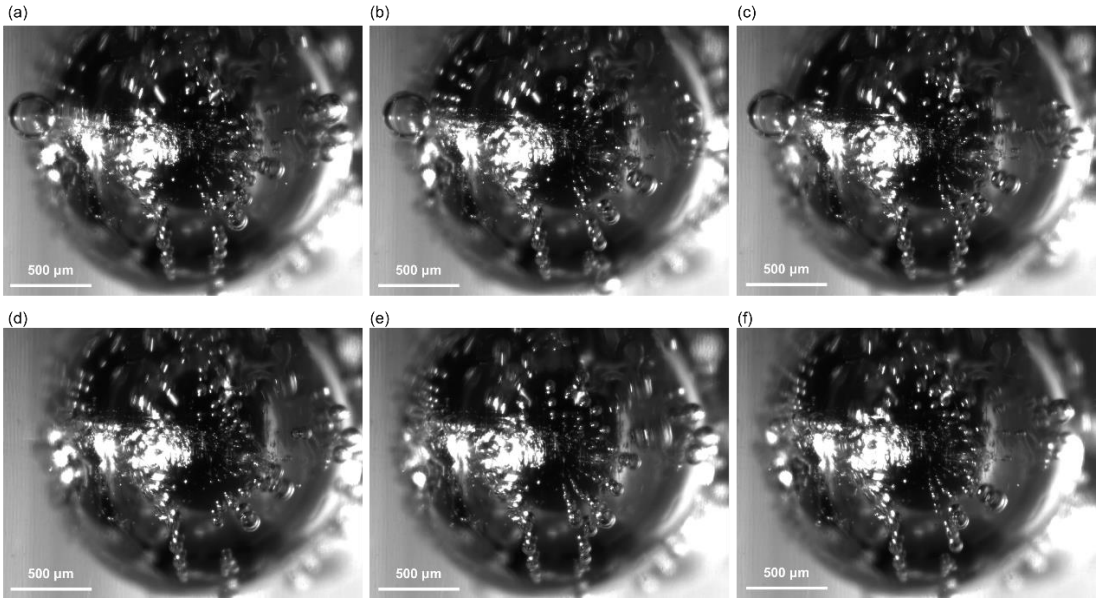

Figure 3.11 Optical images of *in situ* bubble behavior observation on Pt microfacet with less microfacet at 1200 s: (a) 0 s, (b) 0.50 s, (c) 1.0 s, (d) 1.5 s, (e)2.0 s, and (f) 2.5 s

In Figure 3.9, the potential on the Pt microelectrode with more microfacet proceeds stably. On the other hand, the potential on the less microfacet electrode exhibits some fluctuations during the electrolysis. The potential on the less microfacet electrode shows a lower value than that of on the more microfacet electrode at the early stage of the measurement. This trend indicates that (111) microfacet does not function as the reaction sites for HER, which leads to the smaller electrochemically active surface area. As the electrolysis proceeds, the evolved bubbles cover the surface of the less microfacet electrode, and the potential increases. To consider the bubble behaviors' effect, the bubble behaviors on the surface were analyzed from the results in Figures 3.10 and 3.11. In Figure 3.10, bubbles are mainly generated on the non-microfacet regions, whereas no bubbles are generated on the (111) microfacet as same in Figure 3.6. This phenomenon exhibits the trend that bubbles preferentially evolves around the (111) microfacet, especially at the microfacet edge. The previous study indicated that the end of the (111) microfacet had step-ledge structures [13], and the edge of the (111) microfacet had some different structures from the (111) plane. These features suggested that these structures, different from the (111) plane, positively influence bubble formation.

On the other hand, the different behavior is confirmed on the less microfacet electrode. In Figure 3.12, bubbles are generated on the random sites on the Pt surface, and larger bubbles appear on the surface. The potential profile in Figure 3.9 also shows that the fluctuations derived from the bubble detachment occur. These results indicate that the (111) microfacet introduces the sites that preferentially occur bubble nucleation process, and the introduction of the sites for bubble nucleation can control the bubble nucleation [14,15]. It is suggested that the control of the bubble nucleation process could improve the HER efficiency by inhibiting the occupation of the reaction sites for HER by bubbles.

To analyze the effect of the potential on the bubble behaviors on the microfacet, the galvanostatic electrolysis at -40 mA cm^{-2} was carried out, as shown in Figure 3.12. *In situ* bubble observations were also carried out during the electrolysis, as shown in Figures 3.13 and 3.14.

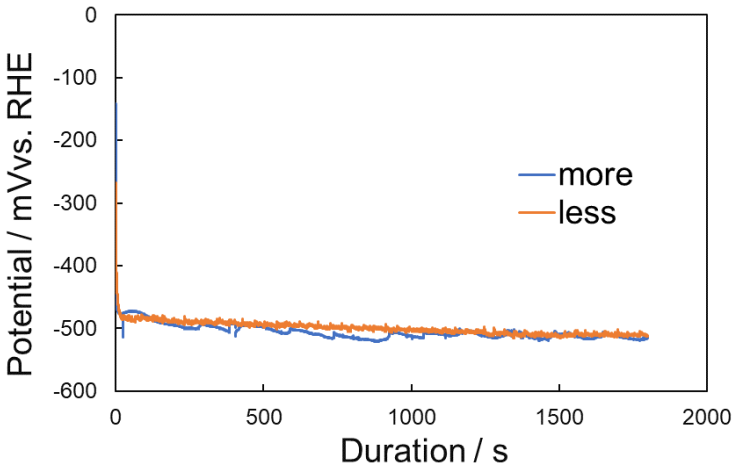

Figure 3.12 Potential profiles of Pt (111) microfacet electrodes with different number of microfacet at −40 mA cm^{-2}

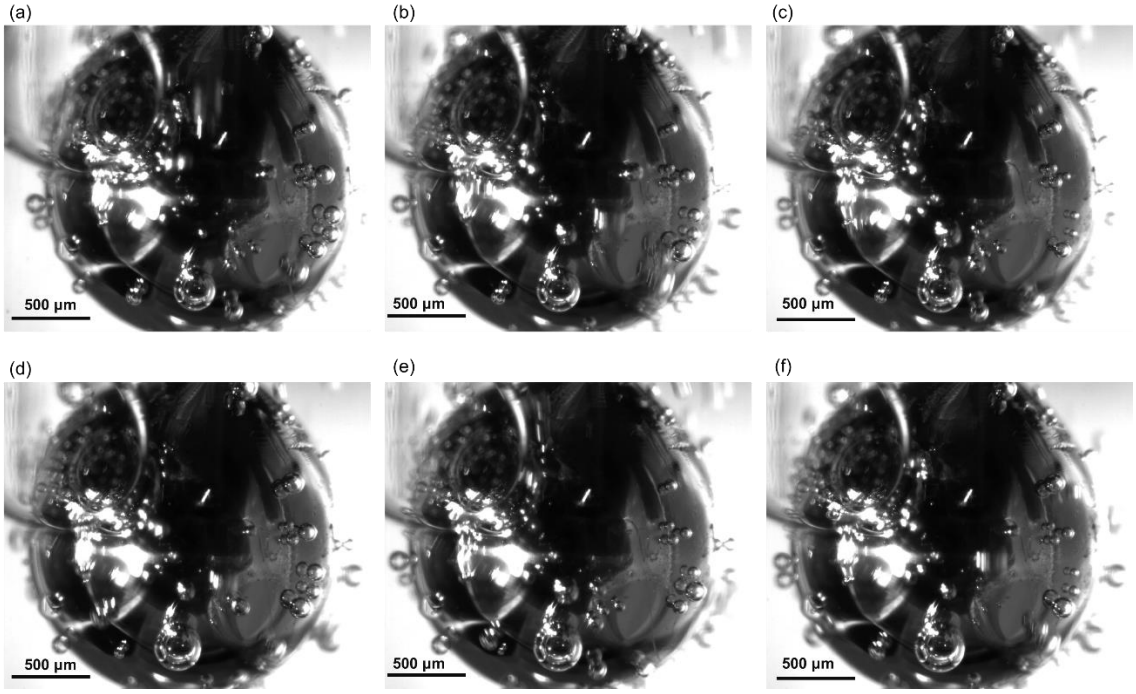

Figure 3.13 Optical images of *in situ* bubble behavior observation on Pt microfacet with more microfacet at 1200 s: (a) 0 s, (b) 0.50 s, (c) 1.0 s, (d) 1.5 s, (e)2.0 s, and (f) 2.5 s

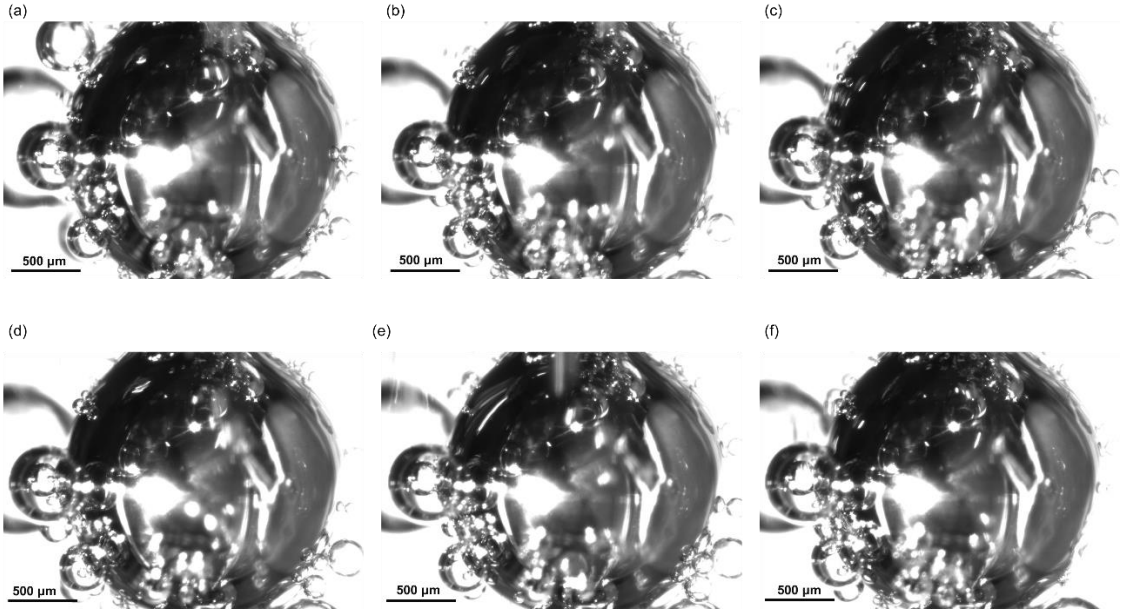

Figure 3.14 Optical images of *in situ* bubble behavior observation on Pt microfacet with less microfacet at 1200 s: (a) 0 s, (b) 0.50 s, (c) 1.0 s, (d) 1.5 s, (e)2.0 s, and (f) 2.5 s

From Figure 3.12, a similar tendency is observed at a higher current density. The potential profile confirms that the reaction proceeds stably on the more microfacet electrode. On the other hand, some large fluctuations appear in the profile of the less microfacet electrode. By comparing bubble behaviors on the electrode surface from Figures 3.13 and 3.14, large bubbles are generated on the less microfacet electrode. Moreover, the potential difference decreases at the early stage of the electrolysis. This observation indicates that the (111) microfacet acts as the reaction site by applying more overpotential, as shown in Figure 3.7. Figure 3.13 also demonstrated that bubbles preferentially evolve on the microfacet edge, but some bubbles are generated on the (111) microfacet, as Figure 3.8 due to the higher overpotential.

To further compare the effect of introducing the (111) microfacet on bubble behaviors, the bubble behaviors on Pt microelectrode with no microfacet were observed by the *in situ* observation shown in Figure 3.15 and 3.16.

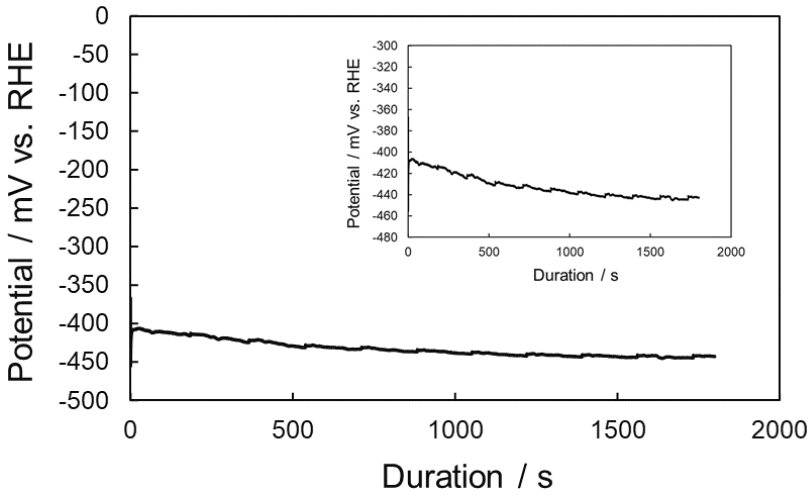

Figure 3.15 Potential profile of Pt microelectrode with no microfacet during the galvanostatic electrolysis at -20 mA cm^{-2}

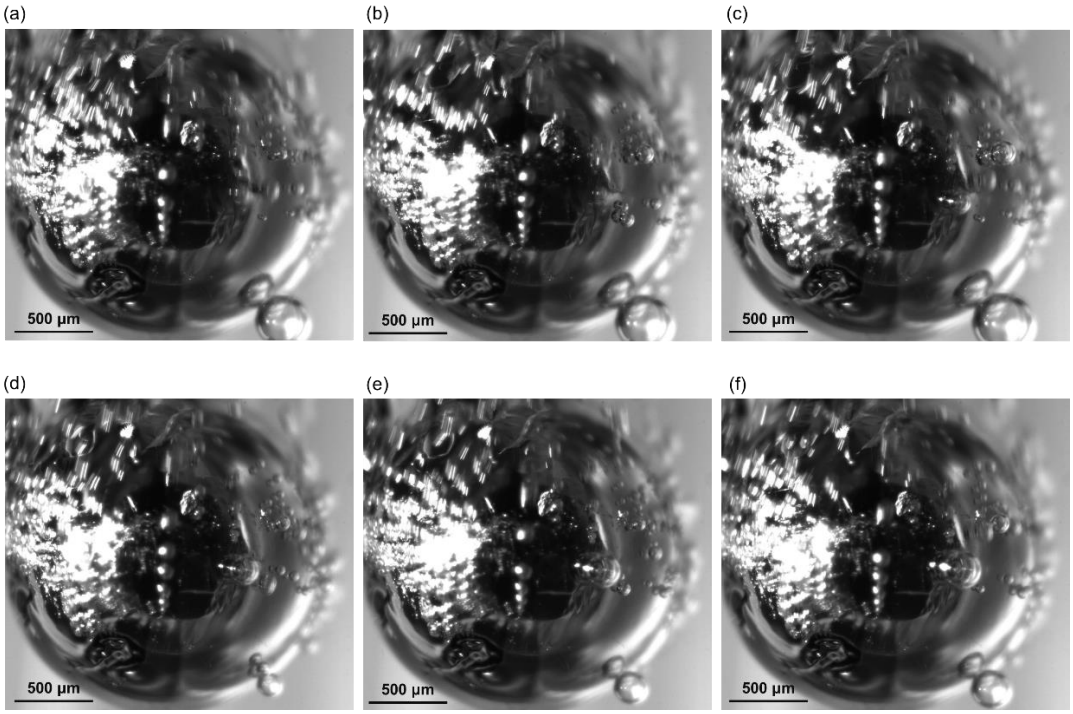

Figure 3.16 Optical images of *in situ* bubble behavior observation on Pt microfacet with no microfacet at 1200 s: (a) 0 s, (b) 0.50 s, (c) 1.0 s, (d) 1.5 s, (e)2.0 s, and (f) 2.5 s

From Figure 3.15, the gradual increase of the potential during the electrolysis is observed, and the fluctuations by the rapid change of surface area by bubble detachment appear. Bubble evolution occurs randomly, and bubbles tend to aggregate, especially the larger bubbles tend to aggregate with the smaller bubbles around themselves in the *in situ* observation. These results indicate that the large bubbles generated by the aggregation cause a temporal decrease in the surface area. However, the detachment of bubbles caused the Marangoni effect that enhances the conventions of the electrolyte near the surface [16], which leads to a decrease in the overpotential. Compared with the bubble behaviors on the microfacets, it is suggested that bubbles differently behaved on the surface without the sites that are suitable for bubble nucleation [14].

To further analyze the bubble growth on the Pt microfacet electrode, bubble size on the electrode surface was compared between 0 min and 20 min from the start of the galvanostatic electrolysis at −20 mA cm^{-2}. Figure 3. 17 shows the observation results of bubble behavior on the surface with various microfacets. In Figures 3. 17(a) and (b), bubbles are preferentially generated and grow on the microfacet edge, and the bubble size before the detachment is changed slightly small from 0 min to 20 min of the electrolysis. In contrast, on less microfacet electrode (Figures 3. 17(c) and (d)) and no microfacet electrode (Figures 3. 17(e) and (f)), the bubble diameter before detaching from the surface decrease as the duration proceeds (0 min → 20 min). One possible reason to decrease the diameter of the bubble is thought to be the Marangoni effect that introduces the convection of the electrolyte by bubble detachment. This effect leads to enhancing the following bubble detachment from the surface [16]. The bubble nucleation and growth on the surface of no and less microfacet electrodes is strongly influenced by the other bubbles surrounding a single bubble. In contrast, Bubble nucleation and growth are rarely affected by the other bubble around the microfacet on the microfacet surface, which results that bubbles stably grow as the previous study [14] and the small decrease of the surface region where HER proceeds.

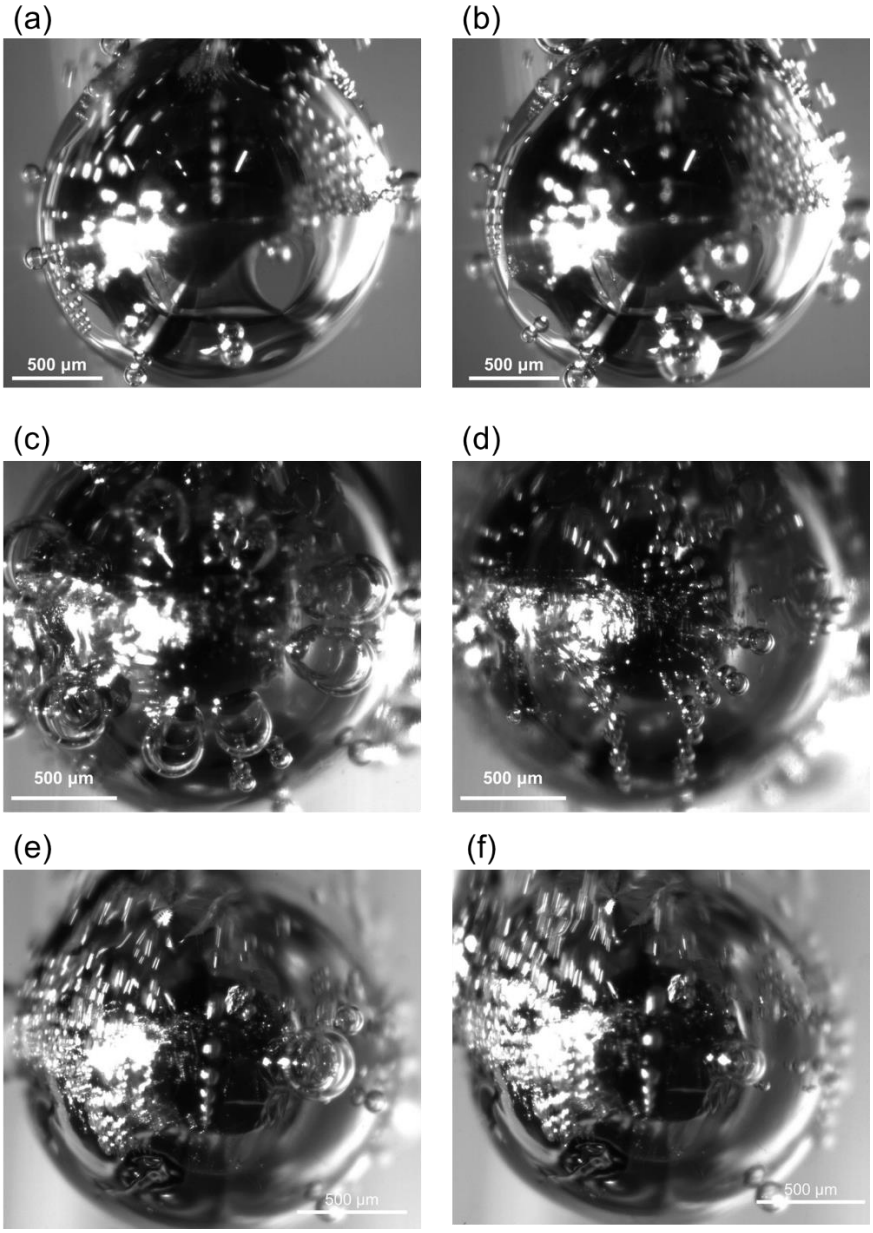

Figure 3. 17 Optical images of *in situ* bubble behavior observation on Pt microfacet before the detachment of bubbles: (a) 0 min and (b) 20 min on more microfacet electrode, (c) 0min and (d) 20 min on less microfacet electrode, (e) 0min and (f) 20 min on no microfacet electrode

From these results obtained by the analyses using the Pt (111) microfacet electrodes, the effect of introducing the well-defined facet such as the (111) microfacet on the bubble behaviors is suggested as follows. On the surface of the electrode with the sites suitable for bubble nucleation, bubbles tend to evolve on the fixed sites. This bubble evolution can suppress the occupation of other areas by the bubbles and proceed the following HER. Therefore, the introduction of the microfacet as the site for bubble nucleation will improve the HER efficiency by controlling bubble nucleation differently from the electrode without the microfacet.

3.4. Conclusion

Chapter 3 aimed to analyze the bubble behaviors on the surface equipped with the well-defined region. Moreover, the effect of the microfacet introduction on bubble behaviors and HER efficiency was investigated. For these analyses, the Pt (111) microfacet electrodes with a different number of (111) microfacet were prepared. Prior to the analyses, the Pt (111) microfacet electrodes were fabricated by the Clavilier method (hydrogen-oxygen annealing process). The electrochemical measurements revealed that no bubble formation occurred on the (111) microfacet with relatively small overpotential. This bubble behavior indicated that the lower HER activity and the smaller roughness of the (111) microfacet would suppress the bubble formation on the (111) microfacet surface. *In situ* bubble behavior observation also indicated that bubble nucleation preferentially proceeded at the microfacet edge rather than the flat surface of the microfacet. Moreover, the HER efficiency evaluated by the galvanostatic electrolysis indicated that the (111) microfacet improved the efficiency by affecting the bubble nucleation behaviors at relatively low current density conditions.

Based on these results, it is suggested that the introduction of the sites favorable for bubble nucleation changes the bubble behaviors on the surface, especially influences covering the surface by bubbles. It can be concluded that the existence of these specific structures will improve HER efficiency.

References

[1] X. Li, X. Hao, A. Abudula, G. Guan, Nanostructured catalysts for electrochemical water splitting: current state and prospects, *J. Mater. Chem. A* **4** (2016) 11973.

[2] G. B. Darband, M. Aliofkhazraei, S. Shanmugam, Recent advances in methods and technologies for enhancing bubble detachment during electrochemical water splitting, *Renewable Sustainable Energy Rev.* **114** (2019) 109300.

[3] K. Kashiwagi, T. Hattori, Y. Samejima, N. Kobayashi, S. Nakabayashi, Hydrogen Nanobubbles at Roughness-Regulated Surfaces: Why Does the Standard Hydrogen Electrode Need a Platinized Platinum Electrode?, *J. Phys. Chem. C* **123**(12) (2019) 7416.

[4] W. Xi, G. Yan, H. Tan, L. Xiao, S. Cheng, S. U. Khan, Y. Wang, Y. Li, Superaerophobic P-doped Ni(OH)2/NiMoO4 hierarchical nanosheet arrays grown on Ni foam for electrocatalytic overall water splitting, *Dalton Trans.* **47** (2018) 8787.

[5] N. M. Markovic, R. N. Ross, Surface science studies of model fuel cell electrocatalysts, *Surf. Sci. Rep.* **45** (2002) 117.

[6] N. M. Markovića, S. T. Sarraf, H. A. Gasteiger, R. N. Ross Jr., Hydrogen electrochemistry on platinum low-index single-crystal surfaces in alkaline solution, *J. Chem. Soc., Faraday Trans.* **92** (1996) 3719.

[7] V. Climent, J. M. Feliu, Thirty years of platinum single crystal electrochemistry, *J. Solid State Electrochem.* **15** (2011) 1297.

[8] K. A. Jaaf-Golze, D. M. Kolb, D. Scherson, On the voltammetry of curves of Pt (111) in aqueous solutions, *J. Electroanal. Chem.* **200**(1) (1986) 353.

[9] J. Clavilier, R. Faure, G. Guinet, R. Durand, Preparation of Monocrystalline Pt Microelectrodes and Electrochemical Study of the Plane Surface Cut in the Direction of the (111) and (110) Planes, *J. Electroanal. Chem.* **107** (1980), 205.

[10] I. Fromondi, D. A. Scherson, Oxidation of Adsorbed CO on Pt(111) in CO-Saturated Perchloric Acid Aqueous Solutions: Simultaneous In Situ Time-Resolved Reflectance Spectroscopy and Second Harmonic Generation Studies, *J. Phys. Chem. B* **110** (2006) 20749.

[11] N. Furuya, M. Ichinose, M. Shibata, Production of high-quality Pt single Crystals using a new flame float-zone method, *Phys. Chem. Chem. Phys.* **16** (2001) 3255.

[12] N. Markovic, M. Hanson, G. McDougall, and E. Yeager, The effects of anions on hydrogen electrosorption on platinum single-crystal electrodes, *J. Electroanal. Chem.* **214** (1986) 555.

[13] S. Tanaka, S. Yau, K. Itaya, In-situ scanning tunneling microscopy of bromide adlayers on Pt(111), *J. Electroanal. Chem.* **396** (1995) 125.

[14] C. Brussieux, P. Viers, H. Roustan, M. Rakib, Controlled electrochemical gas bubble release from

electrodes entirely and partially covered with hydrophobic materials, *Electrochim. Acta* **56** (2011) 7194.

[15] P. Peñas, P. Linde, W. Vijselaar, D. Meer, D. Lohse, J. Huskens, H. Gardeniers, M. A. Modestino, D. F. Rivas, Decoupling Gas Evolution from Water-Splitting Electrodes, *J. Electrochem. Soc.* **166**(15) (2019) H769.

[16] X. Yang, D. Baczyzmalski, C. Cierpka, G. Mutschke, K. Eckert, Marangoni convection at electrogenerated hydrogen bubbles, *Phys. Chem. Chem. Phys.* **20** (2018) 11542.

Chapter 4:

Development of Direct Fabrication Process of the Catalytic Electrode on AEM using Electroless Deposition Process

4.1. Introduction

Anion exchange membrane (AEM) water electrolysis process has been paid attention to [1, 2]. AEM water electrolysis process has the advantages; It shows higher efficiency due to the reduction of the resistance between the electrodes compared with the alkaline solution water electrolysis, and the non-noble metal-based materials apply to the catalytic electrodes due to the lower corrosion resistivity compared with the proton exchange membrane (PEM) electrolysis process [3, 4]. Furthermore, the reaction proceeded at the cathode is the same reaction as that of the alkaline solution water electrolysis process. The materials of the alkane water electrolysis can be adaptable to the electrodes. Therefore, this AEM water electrolysis process is a promising candidate for the next-generation water electrolysis process.

Focusing on the cathode electrode directly producing hydrogen, the highly efficient catalytic electrodes with lower-cost must be developed for the applications. The conventional catalytic electrodes are categorized into two substrates: the catalyst coated substrate (CCS) and the catalyst coated membrane (CCM). The previous studies indicated that the CCM type catalytic electrode exhibited better performance than that of the CCS type because of the improving the contact resistance between the polymer electrolyte and the catalytic electrodes, and the mass transport of ions [5, 6]. The spray process has been widely employed as the conventional fabrication process due to easy control of the loading amount on AEM [7, 8]. However, the applications of the catalytic electrode have been limited because of the lower durability of the electrode by weak adhesion and the difficulty of controlling the surface microstructures [4, 6, 9]. Moreover, it also indicates that the surface structures are essential to enhance the affinity to H_2O for higher HER performance. The microstructures on AEM should play a key role. To address these problems, a new fabrication process is necessary to be developed. As described in Chapters 2 and 3, controlling the surface nano/microstructure could improve HER performance. Therefore, a new fabrication process must be necessary to be investigated.

Electroless deposition process is a powerful technique to fabricate functional thin films by the concept of electrochemistry. This process can fabricate the functional thin

film on the non-conducting substrate. It seems to be suitable for a new fabrication process. Torikai et al. reported that the Pt-based catalytic electrodes were fabricated directly on PEM for water electrolysis process [10, 11]. Nevertheless, there is no previous study that reports the direct fabrication process on AEM using electroless deposition.

In this chapter, in order to achieve the direct fabrication of the electrodes on AEM, the new fabrication process using electroless deposition was investigated, mainly focused on the catalyzation process in the pretreatment process of the electroless deposition process. In addition, the mechanism of the new fabrication process, especially the catalyzation process, and the performance of the fabricated electrodes were also investigated to establish this new process for electrode fabrication.

4.2. Experimental

4.2.1. Electroless deposition processes of the catalytic electrodes on AEM

In this chapter, the substrate for electroless deposition was used the anion exchange membrane (A-201, Tokuyama Corp.) The structure of AEM used in this chapter is shown in Figure 4.1

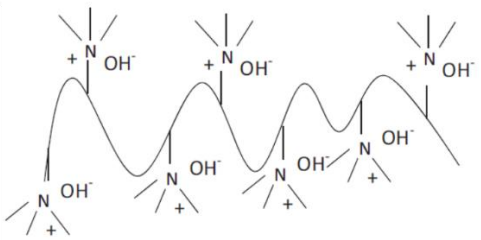

Figure 4.1 Schematic structure of A-201 AEM [1] (Reprinted from Renewable and Sustainable Energy Reviews, 81, I. Vincent, D. Bessarabov, Low cost hydrogen production by anion exchange membrane electrolysis: A review, 1695, Copyright (2018), with permission from Elsevier)

The structure of A-201 consists of the hydrocarbon-based main chains and quaternary ammonium groups as the functional group [1, 12].

Prior to applying the electroless deposition process, the pretreatment process was carried out by the following procedure. AEM, a substrate of electroless deposition process, was rinsed in a sulfuric acid solution (UGR grade, Kanto Chemical Co.) for 30 s, followed by rinsing ultra-pure water for 15 s before the catalyzation process and the electroless deposition process. In this study, two different catalyzation process were applied to analyze the effect of the catalyzation process on the fabrication of the catalytic electrodes. One was the conventional process using the Sn solution and the Pd solution, called the sensitizing-activation process [13] (Sn+Pd process hereafter in this study). In this Sn+Pd process, AEM was immersed into the Sn solution ($SnCl_2 \cdot 2H_2O$ (UGR Grade, Kanto Chemical Co.) + HCl solution (EL Grade, Kanto Chemical Co.) for 30 s, followed by

rinsing ultra-pure water for 15 s (called the sensitization process hereafter in this study). After this process, AEM was immersed into the Pd solution (containing $PdCl_2$ (UGR Grade, Kanto Chemical) and HCl solution (EL Grade, Kanto Chemical Co.)) for 30 s, followed by rinsing ultra-pure water for 15 s (called the catalyzation process hereafter in this study). These processes were repeated three times in the Pd-Sn process. The Conditions of the Sn and Pd solutions are shown in Table 3.1 and 3.2

Table 4.1 The composition of Sn solution

Chemicals	Concentration /mmol dm^{-3}
$SnCl_2{\cdot}2H_2O$	44
HCl	120

Table 4.2 The composition of Pd solution

Chemicals	Concentration /mmol dm^{-3}
$PdCl_2$	10
HCl	30

After repeating this process three times, AEM was immersed in the solution containing 50 mmol dm^{-3} dimethylamine borane (DMAB, Regent Grade, Tokyo Chemical Industry co.). The other process was the Pd process. In this process, AEM after cleaned was immersed in the Pd solution shown in Table 4.2 for 30 s, then rinsed by ultra-pure water for 15 s. After this process, AEM was immersed into a 50 mmol dm^{-3} DMAB solution, as same as the Sn+Pd process.

NiP electroless deposition process was selected as the model process in the electroless deposition because NiP exhibits HER activity in alkaline conditions from the previous study [14] and the NiP electroless deposition process is one of the conventional processes. The electroless NiP deposition conditions [15] are shown in Table 4.3. For the electroless deposition process, AEM after pretreatment was immersed in the solution for 180 s. After immersion into the electroless bath, AEM was rinsed by ultra-pure water for 30 s.

Table 4.3 Electroless NiP deposition conditions

Chemicals	Concentration / mol dm^{-3}
$NiSO_4 \cdot 6H_2O$	0.1
CH_3COONH_4	0.4
$NaH_2PO2 \cdot H_2O$	0.1, 0.2, 0.5, 1.0
Conditions	
pH	5.0 ~ 5.5
Temp.	50 ℃

The surface morphologies and the compositions of the NiP catalytic electrode on AEM were observed by a scanning electron microscopy (SU-8240, Hitachi) with energy-dispersive X-ray spectroscopy.

4.2.2. Theoretical analysis of the catalyzation mechanism using Pd solution in the electroless deposition process

All the theoretical analyses were carried out by density functional theory (DFT) using Gaussian 09 [16]. The exchange-correlation functional was B3LYP. The basis set for H and C was6-31G** [17, 18], the basis set for N and Cl was 6-31+G* [17, 18], and the basis set for Sn and Pd was aug-cc-pvdz-pp ECP [19-23]. The solvation effect was realized by a polarized continuum model (PCM) [24]. The model of AEM fragment was considered from Figure 4.1, and the optimization and calculation of the Mulliken charge population were carried out. Using the Mulliken population change, the interaction among the surface and the Sn and Pd species was analyzed by calculating the interaction energy.

4.2.3. Evaluation of the catalytic electrodes on AEM fabricated by electroless deposition process

In order to evaluate the performance of the catalytic electrode fabricated by electroless deposition process, the electrochemical measurements were carried out. The two-electrodes system with the prepared NiP coated AEM and Pt mesh as the working and the counter electrode respectively was used for the measurement. The schematic image of the electrochemical measurement cell is shown in Figure 4.2. The electrolyte for the measurement was 1.0 mol dm^{-3} K_2CO_3 solution as the anode side and ultra-pure water as the cathode side. Prior to conducting the electrochemical measurements, the K_2CO_3 solution and ultra-pure water were deaerated by N_2 gas for 20 min to remove the dissolved oxygen in the electrolyte.

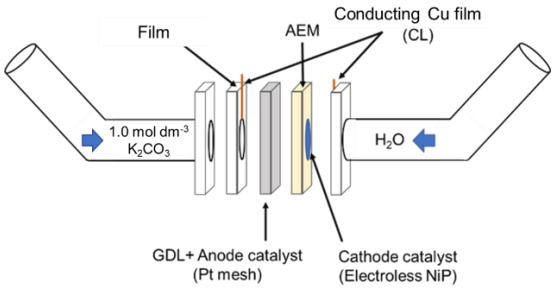

Figure 4.2 Schematic image of the electrochemical cell

All the electrochemical measurements were performed by an electrochemical analyzer (HZ-7000, Hokuto Denko Corp.). LSV of the prepared NiP electrode on AEM was measured by sweeping the voltage from rest to −2.5 V with 10 mV s^{-1}. The galvanostatic electrolysis was also carried out with the current density at −3.5 mA cm^{-2} to evaluate the durability of the prepared NiP electrodes on AEM. The electrochemical measurement conditions are shown in Table 4.4.

Table 4.4 Electrochemical measurement conditions for Evaluating NiP electrode

W. E.	Prepared NiP
C. E.	Pt
Electrolyte	1 M K_2CO_3 (Anode) H_2O (Cathode)
Temperature	R. T. (24 °C)
Applied Current (Galvanostatic electrolysis)	-1.0 mA (-3.5 mA cm^{-2})
Voltage Range (LSV)	REST ~ -2.5 V
Scan Rate (LSV)	10 mV s^{-1}

4.3 Results & Discussion

4.3.1. fabrication of the catalytic electrodes on AEM using electroless deposition process

In order to analyze the effect of the catalyzation process on the electroless deposition process, two different catalyzing processes, the Sn+Pd process and the Pd process, were applied to NiP electroless deposition using AEM as the substrate. Figure 4.3 shows the results of applying two different catalyzation processes.

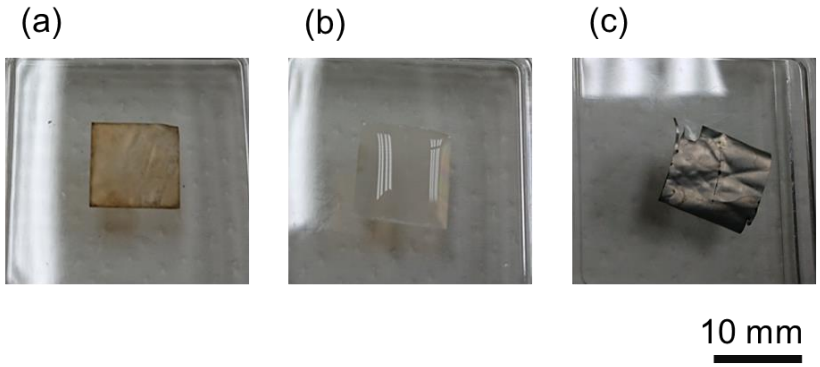

Figure 4.3 Optical images of AEM after the catalyzing and NiP electroless deposition process: (a) Sn+Pd process, (b) Pd process, and (c) Pd process + electroless NiP deposition

From Figure 4.3, the color of the AEM changed to brown-like, as shown in Figure 4.3(a). Any change was not observed after the NiP electroless deposition process. on the other hand, when the Pd process was applied as the catalyzation process, the color of AEM was not dramatically changed, as shown in Figure 4.3(b). It is observed that electroless NiP deposition proceeds and NiP layer is successfully prepared on AEM surface after Pd process in Figure 4.3(c). SEM observation of fabricated electrodes was carried out, and the obtained SEM image is shown in Figure 4.4.

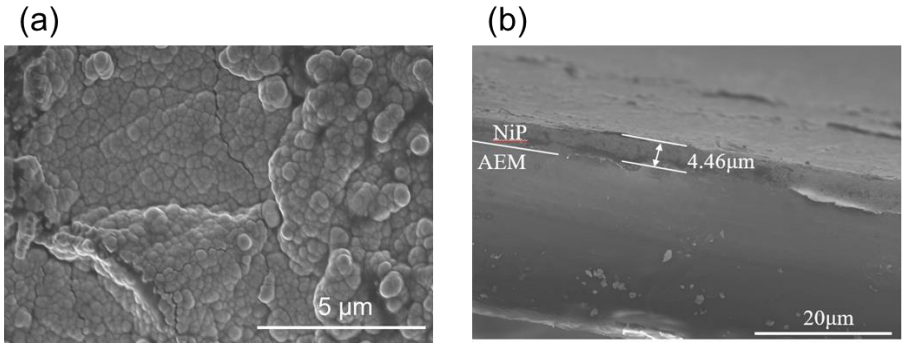

Figure 4.4 SEM images of NiP layer on AEM: (a) top view and (b) cross-sectional view of NiP layer

From Figure 4.4, the electrode with particle-like surface morphologies is fabricated directly on AEM. The SEM-EDS analysis also shows that both Ni and P are detected. This result indicates that NiP layer is successfully prepared by the electroless deposition with the Pd catalyzation process.

To further analyze the effect of the Sn process and Pd process in the catalyzation process, the immersion duration of Sn solution and Pd Solution was varied, and NiP electroless deposition was carried out. The results with different Sn and Pd immersion durations are shown in Figure 4.5.

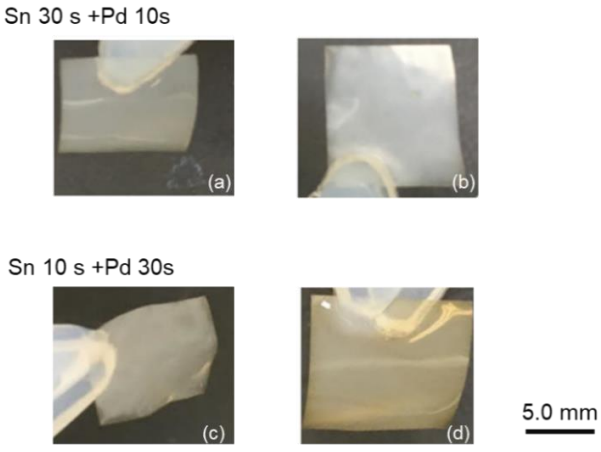

Figure 4.5 Optical images of NiP electroless deposition and Sn+Pd process with different duration: after (a) catalyzation and (b) electroless deposition in Sn 30 s + Pd 10s and after (c) catalyzation and (d) electroless deposition process in Sn 30 s + Pd 10s

From Figure 4.5, NiP layer is not formed on AEM by the Sn+Pd process regardless of the duration of the immersion into the Sn solution. This result indicates that the NiP electroless deposition on AEM can be inhibited by immersion into the Sn solution and the interaction between Pd solution and Sn solution. To analyze the effect of the Sn immersion process, the catalyzation process using only the Sn immersion process was applied to NiP electroless deposition on AEM. The results with Sn catalyzation and NiP electroless deposition are shown in Figure 4.6.

Figure 4.6 Optical images of NiP electroless deposition and Sn process:
After (a) catalyzation and (b) electroless deposition

From Figure 4.6, NiP electroless deposition is inhibited by the Sn process as the catalyzation process. These results suggest that the Sn process can prevent NiP electroless deposition on AEM by interacting with AEM and the Sn solution.

To further analyze the effect of the Pd process on NiP electroless deposition, the catalyzation process with varying duration was applied to NiP electroless deposition on AEM. Figures 4.7 and 4.8 show the optical images of AEM with NiP and SEM images of the NiP layer on AEM with different Pd process duration.

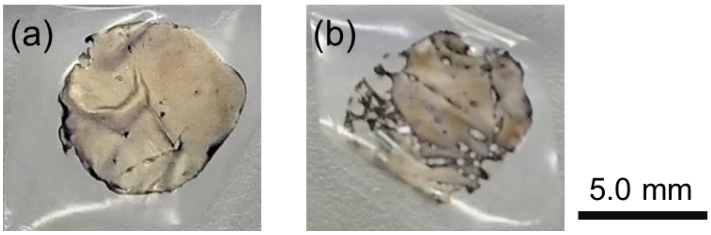

Figure 4.7 Optical images of electroless deposited NiP layer on AEM with different Pd process duration: (a) 10 s and (b) 30 s

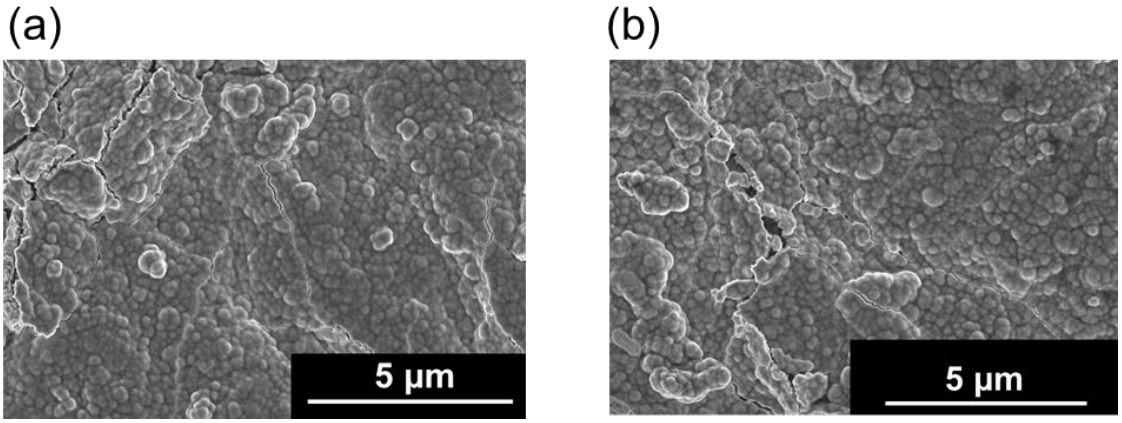

Figure 4.8 SEM images of electroless deposited NiP layer on AEM with different Pd process duration (a) 10 s and (b) 30 s

Figure 4.7 confirms that the Pd process controls the NiP deposits. This result indicates that the amount of Pd particle adsorption affects NiP electroless deposition. Moreover, SEM images shown in Figure 4.8 confirms that particle-like morphologies are fabricated regardless of the Pd process duration. The immersion process changes particle size and aggregation of particles.

From these results, it is suggested that the new direct fabrication process of the catalytic electrodes is developed by the electroless deposition with modifying the catalyzation process, one of the pretreatment processes which introduces the catalyst particle for electroless deposition.

4.3.2. Theoretical analysis of the effect of the catalyzation process on electroless deposition process

In 4.3.1, electroless deposition of NiP on AEM was achieved by the Pd process as the catalyzation process. The results suggested that Sn immersion would inhibit the following the electroless deposition process. In order to analyze the effect of the catalyzation process (i.e., Sn+Pd process and Pd process) on the electroless deposition process, the interaction between AEM and the chemical species in Pd solution and Sn solution was analyzed by theoretical calculation using DFT with Gaussian 09. Prior to analyzing the interaction on the AEM surface, the charge population around the quaternary ammonium group was calculated by the optimization of the structures. Previous studies indicated that the functional groups in the side chain play a significant role in the interaction of AEM to the chemical species, and several studies employed the calculation model of AEM was only composed of multiple functional groups [25, 26]. Furthermore, the detailed structures of the main chain and side chain of the polymer are not supplied in Figure 4.1. Based on these previous studies, DFT calculation was carried out by assuming that the carbon side chain was composed of a simple hydrocarbon chain. The optimization result is shown in Figure 4.9.

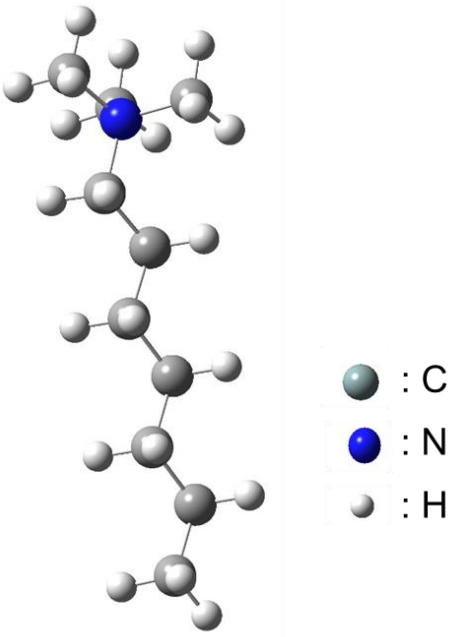

Figure 4.9 Optimized Structure of the fragment of polymer in AEM
(Gray: C, Blue: N, and White: H)

From Figure 4.9, the Mulliken charge population was calculated. The Mulliken charge of the CH_3 group is +0.407, and that of the N atom is −0.664. This result indicates that the $N(CH_3)_3$ region is positively charged in AEM structures. These Mullilen charge values were employed to analyze the interaction among Sn, Pd species, and AEM surface.

In order to analyze the interaction among the Sn, Pd species, and AEM surface, the model of AEM surface, should be maintained. The previous study proposed that the side chains containing the functional groups randomly exist on the surface and inside of the polymer electrolyte membrane, and the structure surrounded by the multiple functional groups were supposed to be formed [27]. Based on this model, it was assumed that the side chains containing $N(CH_3)_3$ groups were randomly located to surround the chemical species. Thus, the calculation model of AEM surface constructed as only multiple $N(CH_3)_3$ groups assumed to come from the branches around the chemical species. Using this simple AEM surface model, the interaction between the $N(CH_3)_3$ functional group and the Sn and Pd species in the solutions were analyzed by DFT calculations, and the optimized structures were considered.

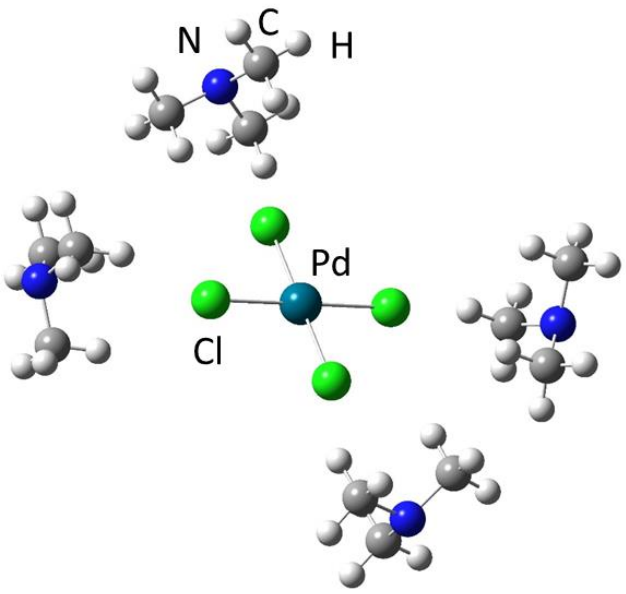

Figure 4.10 Optimized structures of the interaction between Pd species and $N(CH_3)_3$ functional groups on AEM surface
(Gray: C, Blue: N, green: Cl, dark green: Pd, and White: H)

In the Pd process, the Pd species were considered to exist as $[PdCl_4]^{2-}$ complex. The optimized structures of the interaction between $[PdCl_4]^{2-}$ and AEM surface are shown in Figure 4.10. In Figure 4.10, the negatively charged Cl atom interacts with the CH_3 group in $N(CH_3)_3$ functional group by the electrostatic interaction. The energy of the interaction was calculated from the optimized structures. The value of the interaction energy is −20.67 kJ mol^{-1}. This value indicates that the interaction between $[PdCl_4]^{2-}$ and AEM surface is favorable. The Pd species are supposed to stably exist on the AEM surface and function as the catalyst nuclei of electroless deposition.

In the Sn+Pd process, the reaction is shown in equation (4.1) was proceeded, and SnO_3^{2-} species were mainly produced [28].

$$Sn(II) + Pd^{2+} \rightarrow Sn(IV) + Pd\ (0) \qquad (4.1)$$

The interaction between SnO_3^{2-} as the main Sn species and AEM surface was calculated.

The optimized structures are shown in Figure 4.11.

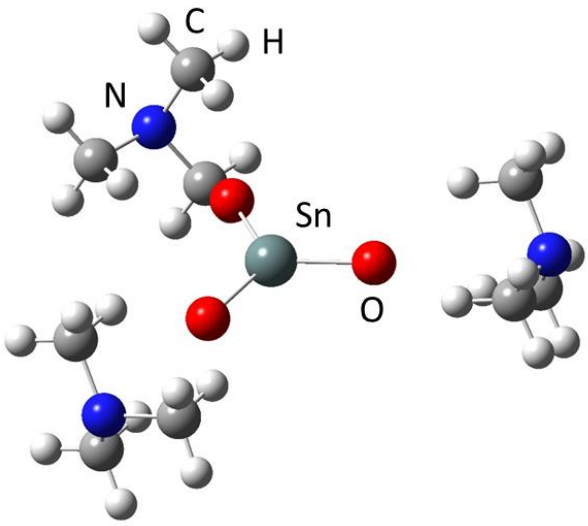

Figure 4.11 Optimized structures of the interaction between Sn species and $N(CH_3)_3$ functional groups on AEM surface
(Gray: C, Blue: N, Red: O, Light gray: Sn, and White: H)

From Figure 4.11, the negatively charged O atoms in SnO_3^{2-} interact with the CH_3 group in $N(CH_3)_3$ functional group by the electrostatic interaction as similar as the interaction between Pd species and AEM in Figure 4.10. The energy of the interaction between SnO_3^{2-} and AEM surface was calculated from the optimized structures in Figure 4.11. The value of the interaction energy is −55.37 kJ mol^{-1}. This value indicates that SnO_3^{2-} also stays on AEM surface stably. By comparing the interaction energies in the Pd process and the Sn+Pd process, the interaction between SnO_3^{2-} and AEM is much stronger than that of with AEM surface. This trend suggests that strongly interacted SnO_3^{2-} exists on AEM surface after the Sn+Pd process. These interaction energies are quite smaller than the bonding energy of C-H, indicating that the interaction of C-H is much stronger than that of AEM to chemical species. This weaker interaction can play a key role in forming Pd nuclei for electroless deposition. The previous study revealed that SnO_3^{2-} in the Sn solution inhibited the formation of Pd catalyst nuclei after immersion into the Pd solution in the Sn+Pd catalyzation process.

From these results obtained by DFT calculations, it may be concluded that forming SnO_3^{2-} species by immersion in Sn solution on AEM inhibits the formation of Pd catalyst nuclei on AEM surface, which results in no formation of NiP layer on AEM. In contrast, negatively charged Cl atoms could supply the stable interaction between Pd and AEM as $[PdCl4]^{2-}$, resulting in the formation of Pd catalyst particles for the following electroless deposition. These results suggest that control of the interaction among the chemical species and AEM surface is the key factor for the electroless deposition on the AEM surface to form the catalyst nuclei.

From the DFT calculations, the interaction of $[PdCl_4]^{2-}$ to the functional group enables the following electroless deposition. This study focuses on the quaternary ammonium group, which is commonly used as the positively charged functional group in AEM [29, 30]. In addition to this quaternary ammonium group, AEMs with different functional groups, such as P atom-based functional groups, have been developed [30]. The interaction between the Cl^- ion, as the counterion, and the functional group in AEM may be one indicator that determines whether the electroless deposition process proceeds [29, 31]. For example, when the interaction of Cl^- ion to the functional group is weaker, it may be difficult to form the Pd nuclei on AEM, and the Pd precursor should be replaced based on the interaction to the functional group in AEM.

4.3.3. Evaluation of the catalytic performance of the electroless deposited NiP catalytic electrodes on AEM

In order to evaluate NiP catalytic electrode on AEM by electroless deposition process in 4.3.1, the electrochemical measurements were conducted to confirm that NiP catalyst layer functioned as HER cathode in AEM water electrolysis process.

Prior to evaluating the catalytic performance of electroless deposited NiP electrode on AEM, NiP catalytic electrodes with different morphologies were fabricated by controlling the concentration of $NiSO_4 \cdot 6H_2O$, the precursor of Ni in the electroless deposition bath shown in Table 4.3. The concentration of $NiSO_4 \cdot 6H_2O$ varied from 0.030,

0.10, and 0.20 mol dm^{-3}. The optical images and SEM images of prepared NiP catalytic electrodes are shown in Figures 4.12 and 4.13.

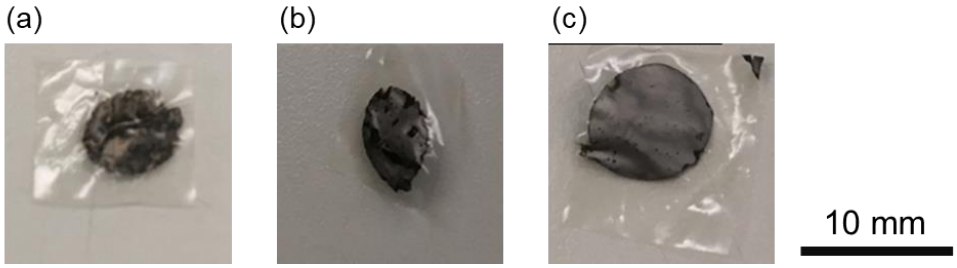

Figure 4.12 Optical images of electroless deposited NiP layer on AEM with different $NiSO_4 \cdot 6H_2O$ concentration: (a) 0.030, (b) 0.10, and (c) 0.20 mol dm^{-3}

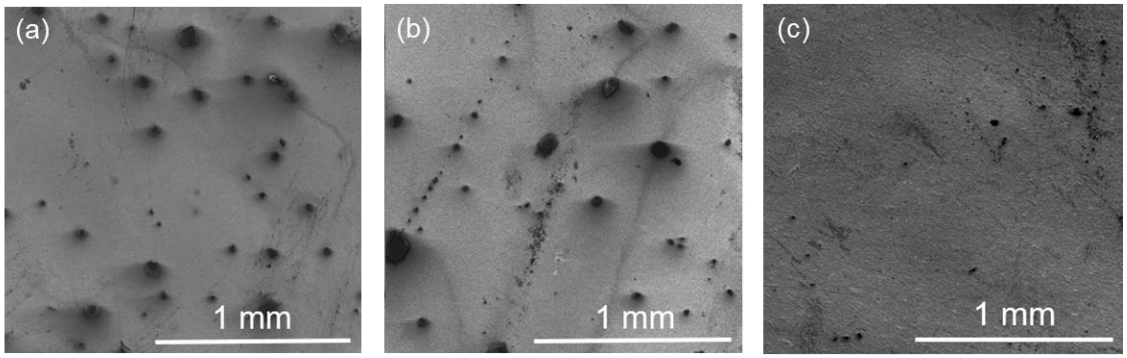

Figure 4.13 SEM images of electroless deposited NiP layer on AEM with different $NiSO_4 \cdot 6H_2O$ concentration: (a) 0.030, (b) 0.10, and (c) 0.20 mol dm^{-3}

From Figure 4.12, uniform NiP catalytic electrodes are fabricated on AEM surface regardless of the concentration of the Ni precursor. SEM images in Figure 4.13 also confirmes that AEM surface is covered with NiP catalytic electrodes, and the particle-like morphologies are generated. To analyze the composition of NiP electrodes, SEM-EDS analysis was carried out, and the obtained composition is shown in Table 4.5.

Table 4.5 Atomic ratio of NiP catalytic electrode with different $NiSO_4 \cdot 6H_2O$ concentration

$NiSO_4 \cdot 6H_2O$ Concentration / M	Atomic ratio of Ni to P
0.03	75.7 : 24.3
0.1	82.1 : 17.9
0.2	87.4 : 12.6

The SEM-EDS analysis reveals that the ratio of P increases as the concentration of Ni precursor decreased [32].

In order to evaluate the catalytic electrodes on AEM fabricated by electroless deposition process, the electrochemical measurements were carried out. First, to evaluate the HER activity of electroless deposited NiP, LSV measurements were carried out, as shown in Figure 4.14.

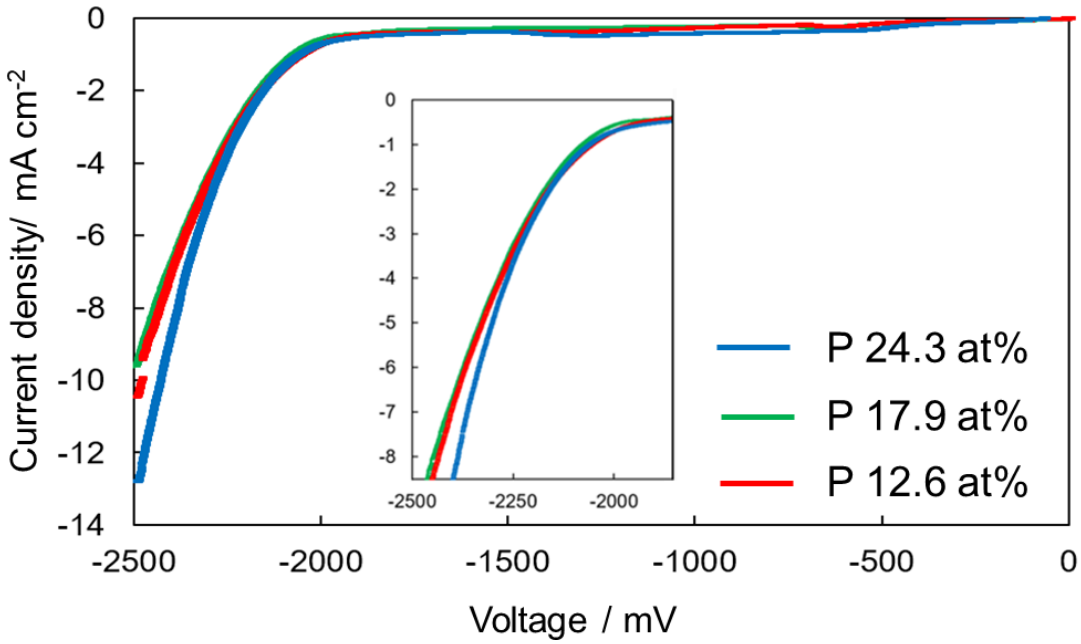

Figure 4.14 LSV of prepared NiP catalytic electrodes on AEM with different composition (Inserted graph is an enlarged view of the potential from −1800 to −2500 mV)

From LSV in Figure 4.14, an increase in the current density derived from HER is confirmed. The onset potential is almost similar in this range of P composition. On the other hand, the current density at −2500 mV is larger on NiP with higher P composition than other compositions. The previous study indicated that a negatively charged P that draws from metal ions could behave to trap proton during HER [33]. Based on that, NiP with high P composition exhibits higher HER activity among these NiP catalytic electrodes in Figure 4.14. To further analyze the effect of surface morphologies on HER performance, the resistance between the electrodes was measured by iR measurement at −2500 mV. The values of the resistance between the electrodes were 12.9 Ω at 12.6 at%, 14.5Ω at 17.9 at%, and 11.7 Ω 24.3 at%, respectively. This result indicates that particle-like morphologies would not be favorable to bubble desorption. From these results, it is confirmed that NiP catalytic electrodes fabricated by electroless deposition function as the cathode in AEM water electrolysis process, and this electroless deposition process can control the surface morphologies of the catalytic electrode on AEM.

To evaluate the durability of NiP catalytic electrodes, the galvanostatic electrolysis at −3.5 mA cm^{-2} for 30 min was carried out. The voltage profile is shown in Figure 4.15.

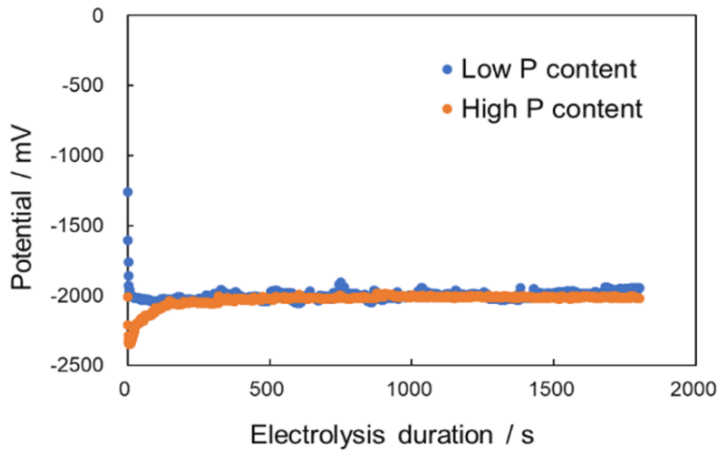

Figure 4.15 Voltage profile during the galvanostatic electrolysis at −3.5 mA cm^{-2} with different NiP composition

From the voltage profile, no drastic voltage change is not confirmed, regardless of the

composition. This result indicates that the compact deposits on AEM enhance the adhesion of NiP catalytic electrode to AEM. These results suggest that the NiP catalytic electrode with controllable composition, morphology, and durability is achieved by the electroless deposition process.

4.4. Conclusion

In chapter 4, a new direct fabrication process of the catalytic electrodes on AEM was investigated using electroless deposition. Electroless deposition process is advantageous to form the functional thin films on the non-conducting substrate such as polymer electrolyte in this study. First, focusing on the catalyzation process, the effect of the catalyzing process on electroless deposition process was analyzed. The obtained results confirmed that the electroless deposited layer on AEM was successfully fabricated by the Pd process as the catalyzation process. The DFT analysis indicated that SnO_3^{2-} species formed in the catalyzation process inhibited the deposition of NiP on the AEM because stronger interaction between SnO_3^{2-} and AEM surface inhibited the formation of Pd nuclei on AEM surface. Moreover, SEM analysis confirms that a uniform layer is successfully prepared by this electroless deposition process. The electrochemical measurements demonstrated that the catalytic electrode on AEM functioned as the cathode of AEM water electrolysis process.

The collective results have suggested that the new fabrication process is achieved by controlling the catalyzation process of electroless deposition process. To the best of our knowledge, this investigation is the first-time study that electrode layer is fabricated on AEM surface using the electroless deposition process without any ionomers.

References

[1] I. Vincent, D. Bessarabov, Low cost hydrogen production by anion exchange membrane electrolysis: A review, *Renewable Sustainable Energy Rev.* **81** (2018) 1690.

[2] S. Marini, P. Salvi, P. Nelli, R. Pesenti, M. Villa, M. Berrettoni, G. Zangari, Y. Kiros, Advanced alkaline water electrolysis, *Electrochim. Acta* **82** (2012) 384.

[3] K. Zeng, D. Zhang, Recent progress in alkaline water electrolysis for hydrogen production and applications, *Prog. Energy Combust. Sci.* **36** (2010) 307.

[4] H.A. Miller, K. Bouzek, J. Hnat, S. Loos, C.I. Bernäcker, T. Weißgärber, L. Röntzsch, J. Meier-Haack, Green hydrogen from anion exchange membrane water electrolysis: A review of recent developments in critical materials and operating conditions, *Sustain. Energy Fuels* **4** (2020) 2114.

[5] J. E. Park, S. Y. Kang, S. Oh, J. K. Kim, M. Su Lim, C. Ahn, Y. Cho, Y. Sung, High-performance anion-exchange membrane water electrolysis, *Electrochim. Acta* **295** (2019) 99.

[6] H. Ito, N. Miyazaki, S. Sugiyama, M. Ishida, Y. Nakamura, S. Iwasaki, Y. Hasegawa, A. Nakano, Investigation on electrode configurations for anion exchange membrane electrolysis, *J. Appl. Electrochem.* **48** (2018) 305.

[7] Y. Leng, G. Chen, A. J. Mendoza, T. B. Tighe, M. A. Hickner, C. Wang, Solid-State Water Electrolysis with an Alkaline Membrane, *J. Am. Chem. Soc.* **134** (2012) 9054.

[8] J. Hnat, M. Plevova, R. A. Tufa, J. Zitka, M. Paidar, K. Bouzek, Development and testing of a novel catalyst-coated membrane with platinum-free catalysts for alkaline water electrolysis, *Int. J. Hydrogen Energy* **44** (2019) 17493.

[9] A. Zadick, L. Dubau, N. Sergent, G. Berthome, M. Chatenet, Huge Instability of Pt/C in Alkaline Medium, *ACS Catal.* **5** (2015) 4819.

[10] H. Takenaka, E. Torikai, Y. Kawami, N. Wakabayashi, Solid Polymer Electrolyte Water Electrolysis, *Int. J. Hydrogen Energy* **7** (1982) 397.

[11] N. Fujiwara, K. Yasuda, T. Ioroi, Z. Siroma, Y. Miyazaki, Preparation of platinum-ruthenium onto solid polymer electrolyte membrane and the application to a DMFC anode, *Electrochim. Acta* **47** (2002) 4079.

[12] K. Fukuta, Electrolyte materials for AMFCs electrolyte materials for AMFCs and AMFC performance. AMFC Workshop 8 may 2011 [Accessed on November 14th, 2020].

[13] Denki-Mekki Kenkyu-kai, Gendai Mekki Kyouhon, Nikkan-Kougyo Shinbunsya, 1st ed, 177 (2014).

[14] Q. Liu, C. Tang, S. Lu, Z. Zou, S. Gu, Y. Zhang, C. M. Li, Rationally tuning the atomic ratio of electrodeposited NiP for greatly enhanced hydrogen evolution in alkaline media, *Chem. Commun.* **54** (2018) 12408.

[15] C. P. Lin, M. Saito, and T. Homma, Initial catalyzation analysis of electroless NiP nanoimprinting mold replicated from self-assembled monolayer modified nanopatterns, *Electrochim. Acta* **82** (2012) 75.

[16] M. J. Frisch, G. W. Trucks, H. B. Schlegel, G. E. Scuseria, M. A. Robb, J. R. Cheeseman, G. Scalmani, V. Barone, B. Mennucci, G. A. Petersson, H. Nakatsuji, M. Caricato, X. Li, H. P. Hratchian, A. F. Izmaylov, J. Bloino, G. Zheng, J. L. Sonnenberg, M. Hada, M. Ehara, K. Toyota, R. Fukuda, J. Hasegawa, M. Ishida, T. Nakajima, Y. Honda, O. Kitao, H. Nakai, T. Vreven, J. A. Montgomery, Jr., J. E. Peralta, F. Ogliaro, M. Bearpark, J. J. Heyd, E. Brothers, K. N. Kudin, V. N. Staroverov, R. Kobayashi, J. Normand, K. Raghavachari, A. Rendell, J. C. Burant, S. S. Iyengar, J. Tomasi, M. Cossi, N. Rega, J. M. Millam, M. Klene, J. E. Knox, J. B. Cross, V. Bakken, C. Adamo, J. Jaramillo, R. Gomperts, R. E. Stratmann, O. Yazyev, A. J. Austin, R. Cammi, C. Pomelli, J. W. Ochterski, R. L. Martin, K. Morokuma, V. G. Zakrzewski, G. A. Voth, P. Salvador, J. J. Dannenberg, S. Dapprich, A. D. Daniels, Ö. Farkas, J. B. Foresman, J. V. Ortiz, J. Cioslowski, and D. J. Fox, Gaussian 09, Revision A.01, Gaussian, Inc., Wallingford, CT (2009).

[17] W. J. Hehre, R. Ditchfield, J. A. Pople, Self—Consistent Molecular Orbital Methods. XII. Further Extensions of Gaussian—Type Basis Sets for Use in Molecular Orbital Studies of Organic Molecules, *J. Chem. Phys.* **56** (1972) 2257.

[18] M. J. Frisch, J. A. Pople, J. S. Binkley, Self-consistent molecular orbital methods 25. Supplementary functions for Gaussian basis sets, *J. Chem. Phys.* **80** (1984) 3265.

[19] D. E. Woon, T. H. Dunning Jr., Gaussian basis sets for use in correlated molecular calculations. III. The atoms aluminum through argon, *J. Chem. Phys.* **98** (1993) 1358.

[20] R. A. Kendall, T. H. Dunning Jr., R. J. Harrison, Electron affinities of the first-row atoms revisited. Systematic basis sets and wave functions, *J. Chem. Phys.* **96** (1992) 6796.

[21] T. H. Dunning Jr., Gaussian basis sets for use in correlated molecular calculations. I. The atoms boron through neon and hydrogen, *J. Chem. Phys.* **90** (1989) 1007.

[22] K. A. Peterson, D. E. Woon, T. H. Dunning Jr., Benchmark calculations with correlated molecular wave functions. IV. The classical barrier height of the H+H2→H2+H reaction, *J. Chem. Phys.* **100** (1994) 7410.

[23] A. Wilson, T. van Mourik, T. H. Dunning Jr., Gaussian basis sets for use in correlated molecular calculations. VI. Sextuple zeta correlation consistent basis sets for boron through neon, *J. Mol. Struct. (Theochem)* **388** (1997) 339.

[24] E. Ca , B. Mennucci, J. Tomasi, A new integral equation formalism for the polarizable continuum model: Theoretical background and applications to isotropic and anisotropic dielectrics, *J. Chem. Phys.* **107** (1997) 3032.

[25] H. Long, B. Pivovar, Hydroxide Degradation Pathways for Imidazolium Cations: A DFT Study, *J. Phys. Chem. C* **107** (2014) 9880.

[26] G. Yang, J. Hao, J. Cheng, N. Zhang, G. He, F. Zhang, C. Hao, Hydroxide ion transfer into anion exchange membrane: A density functional theory study, *Int. J. Hydrogen Energy* **41** (2016) 6877.

[27] K. Jiao, X. Li, Water transport in polymer electrolyte membrane fuel cells, *Prog. Energy Combust. Sci.* **37** (2011) 221.

[28] J. Przylusky, M. Kasprzak, J. Bielinski, Investigation of SiCl2-Sensitizing Solution for Electroless Plating, *Surf. Coat. Technol.* **31** (1987) 203.

[29] C. G. Arges, J. Parrondo, G. Johnson, A. Nadhan, V. Ramani, Assessing the influence of different cation chemistries on ionic conductivity and alkaline stability of anion exchange membranes, *J. Mater. Chem.*, **22** (2012) 3733.

[30] J. R. Varcoe, P. Atanassov,D. R. Dekel, A. M. Herring, M. A. Hickner, P. A. Kohl, A. R. Kucernak, W. E. Mustain, K. Nijmeijer, K. Scott, T. Xuk, L Zhuang, Anion-exchange membranes in electrochemical energy systems, *Energy Environ. Sci*., **7** (2014) 3155.

[31] X. Kong, K. Wadhwa, J. G. Verkade, K. Schmidt-Roher, Determination of the Structure of a Novel Anion Exchange Fuel Cell Membrane by Solid-State Nuclear Magnetic Resonance Spectroscopy, *Macromolecules* **42**(5) (2009) 1659.

[32] L. M. Abrantes, A. Fundo, G. Jin, Influence of phosphorus content on the structure of nickel electroless deposits, *J. Mater. Chem.* **11** (2001) 200.

[33] Y. Shia, B. Zhang, Recent advances in transition metal phosphide nanomaterials: synthesis and applications in hydrogen evolution reaction, *Chem. Soc. Rev.* **45** (2016) 15

Chapter 5:

Analysis of Electrode Structures for the Cathode Reaction in AEM Water Electrolysis

5.1. Introduction

As described in Chapter 4, one of the significant advantages of AEM water electrolysis process is that non-noble metal-based material is available to the catalyst materials [1, 2]. Pavel et al. demonstrated that CeO_2-La_2O_3/carbon support catalyst was applied to the catalytic electrode for HER [3]. Transition metal catalyst materials such as Ni-based materials [4-6] have been proposed as the cathode materials in AEM. Moreover, the materials applied in the alkaline solution water electrolysis can also be available [7]. However, carbon-supported Pt is one of the most common electrode materials for AEM water electrolysis [8,9]. The spray process has been widely employed as the conventional process for preparing Pt/C on polymer electrolyte membrane [10]. However, Pt/C catalyst exhibited lower durability and dissolved into the solution under alkaline conditions due to carbon support instability [7, 8, 11].

Based on this background, the new fabrication process using electroless deposition process was developed in Chapter 4. This process is also able to control the surface microstructures that may play a key role in improving the interaction to H_2O and H_2 in Chapters 2 and 3, fabricated on AEM.

Therefore, this chapter analyzed the HER performance of electroless deposited electrodes on AEM by comparing the conventional Pt/C catalyst sprayed on AEM. It also investigated the effect of microstructures and composition of the catalytic electrodes on HER and the interfacial processes. For these objectives, Pt and NiCoP [12, 13] were selected as the electrode materials.

5.2. Experimental

5.2.1. Fabrication of electroless deposited catalytic electrodes

In this chapter, AEM (A-201, Tokuyama Corp.) was used as the substrate for the electroless deposition to fabricate the CCM type catalytic electrode. The characteristics of AEM is described in 4.2.1. Before the electroless deposition process, AEM substrate was rinsed with a sulfuric acid solution (UGR grade, Kanto Chemical Co.) for 30 s, followed by rinsing ultra-pure water for 15 s as the cleaning of the substrate. After that, the catalyzation process was applied to fabricate the catalyst nuclei. The Pd solution composition is shown in Table 5.1. In the catalyzation process, an AEM was immersed into Pd solution for 30 s, after that rinsed by ultra-pure water for 15 s as described in chapter 4.

Table 5.1 Solution composition of Pd process

Chemicals	Concentration /mmol dm^{-3}
$PdCl_2$	10
HCl	30

After the catalyzation process, the electroless deposition of Pt and NiCoP was carried out. In Pt electroless deposition process, Pt was electrolessly deposited from the electrolyte summarized in Table 5.2, based on the previous studies [14]. The bath temperature was 50 ℃, and the bath's pH was adjusted to 7.0 by a diluted NaOH solution (UGR grade, Kanto Chemical Co.). The electroless deposition duration was 120 min.

Table 5.2 Bath compositions and electroless deposition conditions of Pt

Chemicals	Concentration / mol dm^{-3}
$H_2[PtCl_6]\cdot 6H_2O$	0.0026
EDTA	0.034
HCOOH	1.19
NaCl	1.94
NaH_2PO_4	0.69
Bath Temperature	50 ℃
pH	7 (adjusted by NaOH)

In Electroless deposition of NiCoP, NiCoP was electrolessly deposited from the electroless deposition bath summarized in Table 5.3, based on the previous study [15, 16]. The deposition bath was 50 ℃, and the pH of the electrolyte was adjusted to 8.6 by NH_4OH solution (UGR grade, Kanto Chemical Co.). The concentration of Co was changed from 5.0 to 200 mmol dm^{-3} in order to obtain the NiCoP with a different Ni/Co ratio.

Table 5.3 Bath composition and electroless composition of NiCoP

Chemicals	Concentration / mmol dm^{-3}
$NiSO_4\cdot 6H_2O$	15
$CoSO_4\cdot 7H_2O$	20 - 5
$(NH_4)_2SO_4$	250
$NaH_2PO_2\cdot H_2O$	200
pH	8.6 adjusted by NH_4OH
Bath temperature	50 °C

The morphologies of the fabricated electrodes were observed by a scanning electron microscope (SU-8240, Hitach). The composition of the electrodes was analyzed by SEM-EDS (SU-8240, Hitachi).

5.2.2. Analysis of the effect of surface morphologies on the catalyst performance

For evaluating HER performance of prepared catalytic electrodes, the electrochemical measurements were performed. All the electrochemical measurements were performed utilizing an electrochemical analyzer (VSP-300, Bio-Logic Sciences Instruments); prepared Pt or NiCoP on AEM and Ni foam (10 mm × 10 mm, Nagamine Manufacturing Co. Ltd.) were used as the working and the counter electrodes. For the measurements, the electrochemical cell designed by Yokohama National University was employed. The electrode area was defined as 10 mm × 10 mm, and the detailed setup of the cell is shown in Figure 5.1.

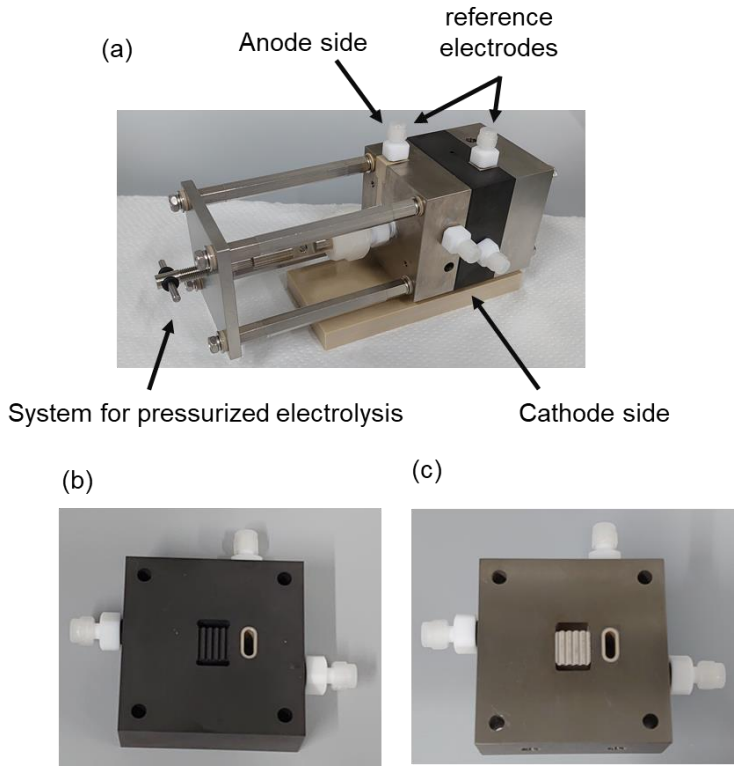

Figure 5.1 Electrochemical measurement cell for AEM water electrolysis:
(a) cell setup, (b) inside of the cathode cell, and (c) inside of the anode cell

For the water electrolysis measurements, the electrolyte was 1.0 mol dm^{-3} K_2CO_3 solution. The 1.0 mol dm^{-3} K_2CO_3 solution was prepared by dissolving K_2CO_3 (UGR grade, Kanto Chemical Co.) into ultra-pure water. Before the measurements, the K_2CO_3 electrolyte was

deaerated by N_2 gas for 20 min to remove the dissolved oxygen. The electrolyte flow was introduced by a smooth-flow pump (Q-100-TT-P-S, Takumima Co.) to only the anode side from the inlet at the bottom of the cell to the outlet at the upper, based on the previous study [8]. The flow rate was 5.0 mL min^{-1}. The detailed setup conditions of the electrochemical measurement cell are shown in Table 5.4.

Table 5.4 Cell setup and operating conditions of the measurement cell

W. E.	Prepared catalysts
C. E.	Ni foam
PTL	Carbon paper (Cathode)
	Ni foam (Anode)
Temperature	R. T. (24 ℃)
Flow rate	5 mL min^{-1}

To evaluate the HER performance of the electrodes, linear sweep voltammetry was performed by sweeping the voltage range from the open circuit voltage (OCV) to −2500 mV with a scan rate of 50 mV s^{-1}. The galvanostatic electrolysis at −500 mA cm^{-2} was also carried out for the evaluation of the HER performance. Electrochemical impedance spectroscopy (EIS) of the membrane-electrode assembly (MEA) was carried out by an electrochemical analyzer (VSP-300, Bio-Logic Sciences Instruments). The alternating current was superimposed at a frequency ranging from 1MHz to 100 Hz at $\Delta I = \pm 100$ μA cm^{-2} at rest potential. Measurements points were 40 points/decades. Curve fittings of the obtained impedance data to equivalent circuits were conducted using software (ZView, Scribner Associates).

In order to compare the HER performance of Pt/C on AEM prepared by the ordinary process, Pt/C spray-coated CCM was prepared. The fabrication process for this Pt/C CCM was supplied by Prof. Ito in the National Institute of Advanced Industrial Science and Technology (AIST) based on his previous research [8, 17]. The prepared Pt/C sprayed CCM is shown in Figure 5.2. the loading amount of Pt/C was 3.0 mg cm^{-2}.

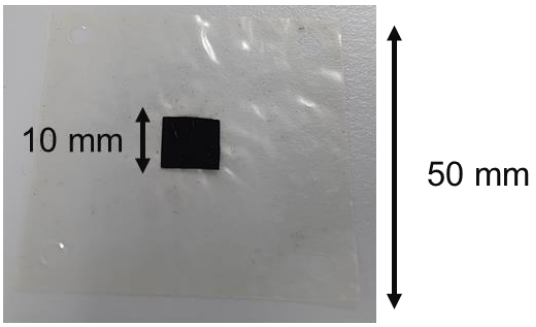

Figure 5.2 Pt/C spray-coated AEM

(AEM: 50 mm ×350 mm, catalyst region 10 mm ×10 mm)

5.3. Results & Discussion

5.3.1. Fabrication of the catalytic electrode on AEM

In order to prepare the Pt electrode on AEM, the electroless deposition of Pt on AEM was carried out for 120 min with the conditions shown in Table 5.2.

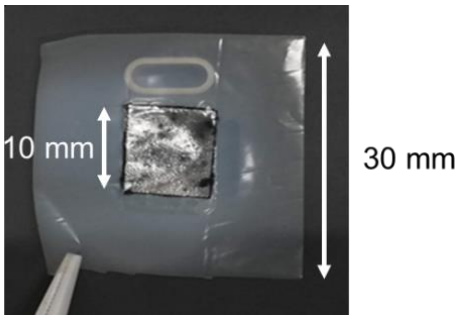

Figure 5.3 Prepared Pt catalytic electrode on AEM
(AEM: 30 mm ×30 mm, catalyst region 10 mm ×10 mm)

As shown in Figure 5.3, a 10 mm ×10 mm size Pt catalytic electrode was directly fabricated on the AEM surface. SEM observation was carried out to observe the morphology and thickness of the deposited Pt layer. Results are shown in Figure 5.4.

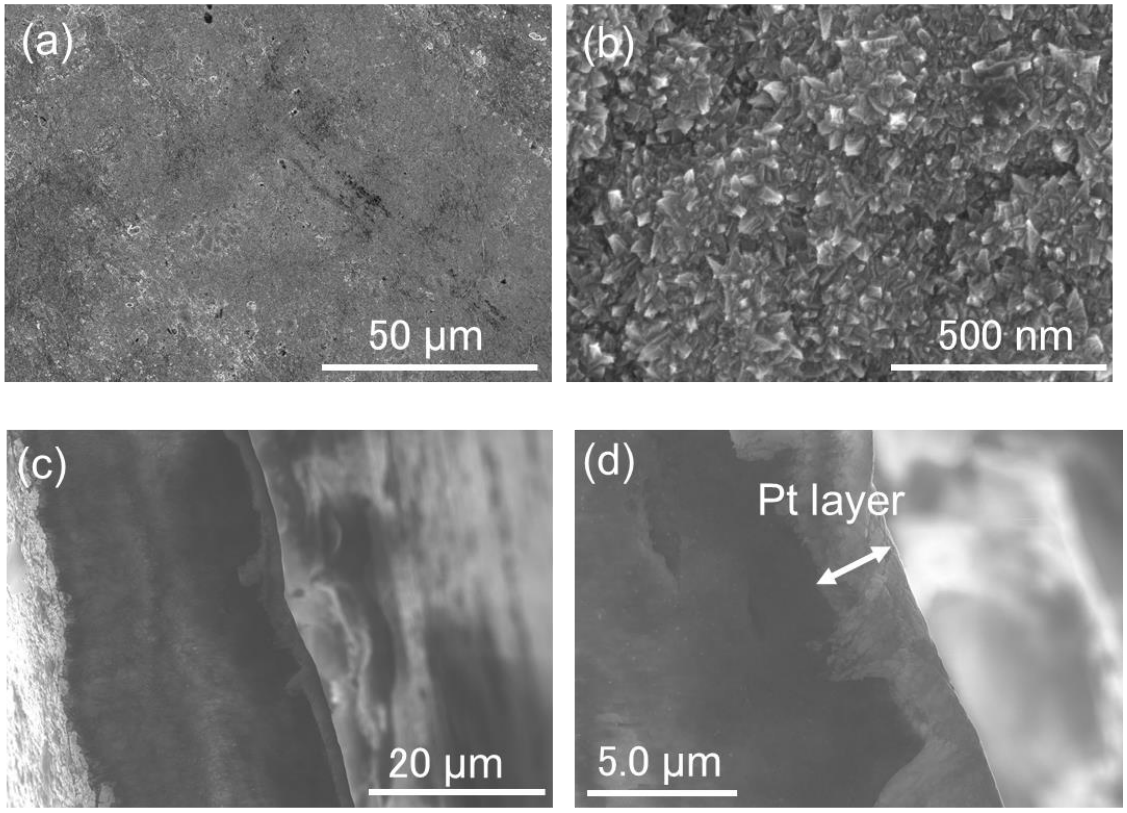

Figure 5.4 SEM images of Pt catalytic electrodes on AEM; (a) top view, (b) enlarged top view, (c) cross-sectional view, and (d) enlarged cross-sectional view of Pt electrode

Figure 5.4 shows that the uniform deposition is observed on the entire surface, and the morphologies are elongated, as reported by the previous paper [18]. SEM images also reveal that the compact layer is formed on the AEM surface and the thickness of the Pt electrode is approximately 2.0 μm. From this value, the calculated loading amount of Pt electrode on AEM was approximately 3.0 mg cm^{-2}. These results demonstrate that the compact Pt electrode layer is successfully fabricated by the electroless deposition process described in Chapter 4.

In order to evaluate the HER performance of the prepared Pt electroless deposition electrode, LSV measurement was performed. Figure 5.5 shows the LSV of the Pt electrode and Pt/C catalyst on AEM by sweeping from 0 mV to −2500 mV with a scan rate of 50 mV s^{-1}.

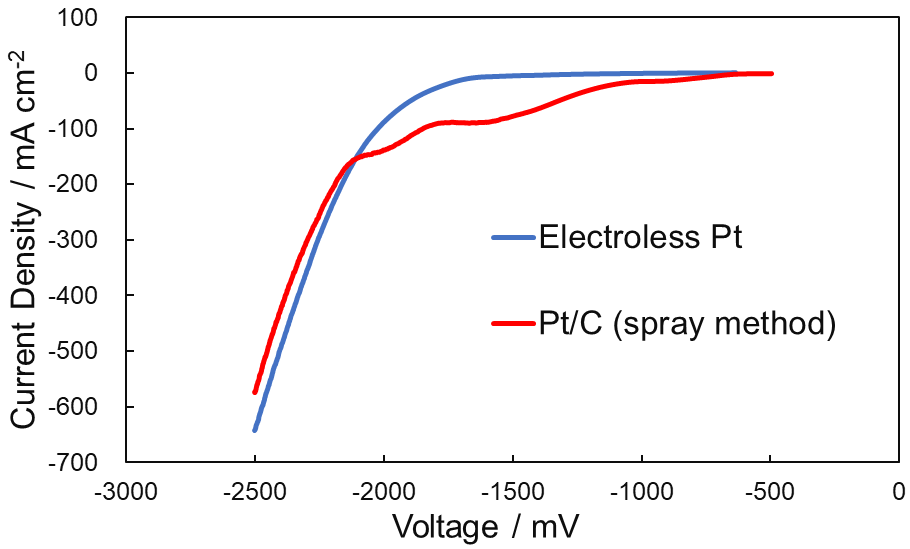

Figure 5.5 Linear sweep voltammograms of electroless Pt electrode on AEM and Pt/C catalyst on AEM

Figure 5.5 shows that the current density is increased around −1800 mV on the electroless Pt electrode, and the gas evolution by HER is confirmed, indicating that the electroless Pt functions as the HER catalytic electrode. On the other hand, the three broad peaks appear in the LSV on the Pt/C electrode. A. Zadick et al. reported that Pt/C catalyst suffers from the dissolution into the electrolyte in alkaline conditions [11, 19].

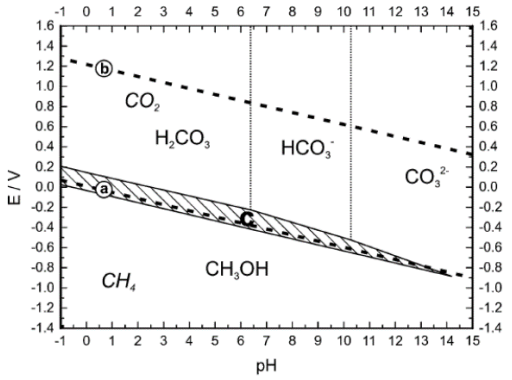

Figure 5.6 Pourbaix diagram of carbon in 298 K [20] (J. R. Varcoe, P. Atanassov, D. R. Dekel, A. M. Herring, M. A. Hickner, Paul. A. Kohl, A. R. Kucernak, W. E. Mustain, K. Nijmeijer, K. Scott, T. Xu and L. Zhuang, Energy Environ. Sci., 2014, 7, 3135- Published by The Royal Society of Chemistry.)

The Pourbaix diagram shown in Figure 5.6 also indicates that in high pH conditions, C stably exists as CH_3OH under the negative potential. From this point, the Pt/C catalyst can be detached from the AEM surface due to dissolving and decomposing C support, and the loading amount decreases. The reaction assumed from the Pourbaix diagram is shown as Equation (5.1).

$$C + H_2O + 2e^- \rightarrow CH_3OH \quad (5.1)$$

The multiple peaks derived from the decomposition of C appears in LSV. Although the exact mechanism for these multiple peaks is not understood, one possibility is that several species exhibiting different oxidation states are produced. The peaks are suggested that these species are reduced to CH_3OH. From these results, it is indicated that the electroless deposition process improves the stability of MEA. Furthermore, comparing the current densities at -2.5 V indicates that electroless Pt on AEM electrode has the almost same HER performance as the conventional Pt/C catalyst coated AEM.

To further analyze the HER performance, the galvanostatic electrolysis at −500 mA cm^{-2} for 10 min was carried out. Figure 5.7 shows the voltage profile of the galvanostatic electrolysis at −500 mA cm^{-2}.

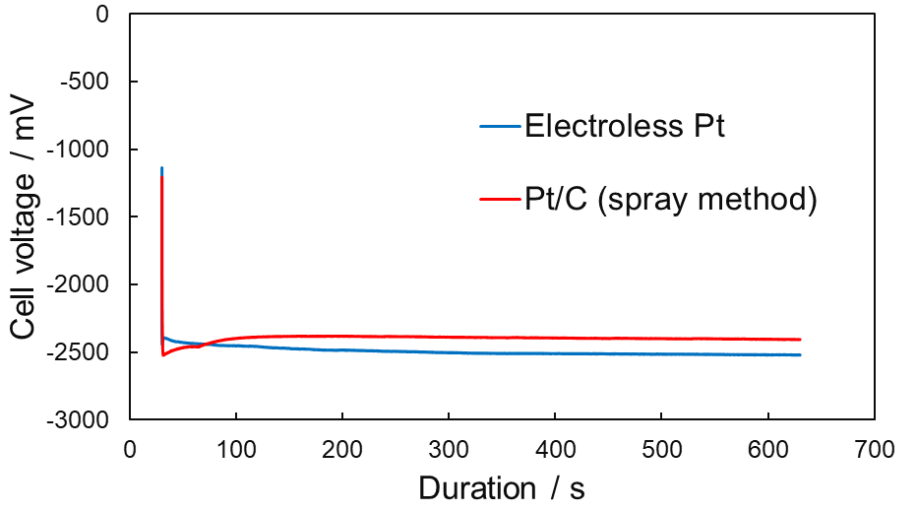

Figure 5.7 The voltage profile of the galvanostatic electrolysis at -500 mA cm^{-2} for 10 min

From Figure 5.7, the voltage slightly increases, and HER stably proceeds on the

electroless Pt electrode. On the other hand, the reaction stably proceeds after a sudden drop of the voltage in the early stage on the Pt/C electrode. By comparing the voltage profile of the electroless Pt electrode and Pt/C coated electrode, the voltage of electroless Pt is smaller than that of Pt/C at the start of the electrolysis. However, this trend is in reverse after 100 s from the start of the electrolysis. The previous study revealed that Pt/C catalyst exhibited higher porosity to obtain the larger surface area [17]. On the other hand, the electroless Pt electrode had compact structures, and Pt was directly attached to AEM in Figure 5.4. Although the exact reason is not completely understood, it is considered that more H_2O molecules, the reactant of HER, are transported from the anode side as the reaction proceed, the required voltage for HER are decreased on large Pt/C surface.

Comparing the LSV result and the voltage profile in Figures 5.5 and 5.7, electroless Pt catalytic electrode possesses the almost same HER performance as the Pt/C CCM from the onset voltage and the current density at −2.5 V in the LSV result. On the other hand, the potential profile exhibits that the Pt/C has a lower overpotential than the electroless Pt catalytic electrodes. From the previous studies, the sprayed Pt/C catalysts possess porous structures that realize the larger electrochemically active surface area inside the Pt/C catalyst layer [21]. In contrast, the electroless Pt catalytic electrode layer had compact and dense structures on the AEM surfaces, as shown in Figure 5.4. The electrode structures of the electroless Pt exhibits the rough elongated shape that can provide the pathways to escape the reduced H_2 molecules from the AEM-electrode interface. However, this compact and dense Pt electrode layer provide the pathways for H_2 gas insufficiently, which may cause trapping H_2 gas on the interface between AEM and the electrode layer or/and covering the active surface by hydrogen gas. These factors may contribute to increasing the excess overpotential for following HER in the galvanostatic electrolysis. Thus, the different behaviors are suggested to be observed in Figure 5.7. On the other hand, the amount of generated H_2 gas during the measurement is much smaller in LSV measurements than in the galvanostatic measurement. This difference can suppress trapping and covering hydrogen bubbles in the interface. Moreover, the contact area of the Pt electrode layer to AEM seems to be larger in the electroless Pt electrode than in the Pt/C cathode due to the compositional difference between electroless Pt and Pt/C. A detailed analysis is necessary to address the different

behaviors in LSV and CP. Nevertheless, this mechanism mentioned above is one of the possible reasons to explain the different performance in LSV and CP measurements.

From these collective results, it is suggested that the electroless Pt electrode exhibits higher durability because the carbon-free Pt electrode suppresses the dissolution of Pt/C. It is also suggested that both the surface structures and the inside structures of the catalytic electrode influence the H_2O and H_2 behaviors during the reaction. It is necessary to analyze the effect of these structural factors on the HER performance in AEM water electrolysis.

5.3.2. Analysis of the effect of surface morphologies on HER performance

To further analyze the effect of surface morphologies on HER, NiCoP catalytic electrodes on AEM were fabricated by the electroless deposition process. In order to control the surface morphologies of deposited NiCoP electrodes, the concentration of Co precursor in the electroless deposition bath was varied from 1.0 mmol dm^{-3} to 20 mmol dm^{-3}. Figure 5.8 shows the SEM images of prepared NiCoP electrodes with different Co precursor concentration. From Figure 5.8, at lower Co concentration in the electroless deposition bath, the particle-like structures are formed, which are similar to the morphology of NiP, as shown in Figure 4.4. As the Co concentration increases, the particle-like structures are transformed into elongated and angular shapes, which are similar to electroless Pt and may be preferable to H_2 gas pathway discussed in 5.3.1. The compositional difference of NiCoP electrode from the different Co concentration bath shown in Figure 5.8 was analyzed by SEM-EDS analysis in Table 5.5.

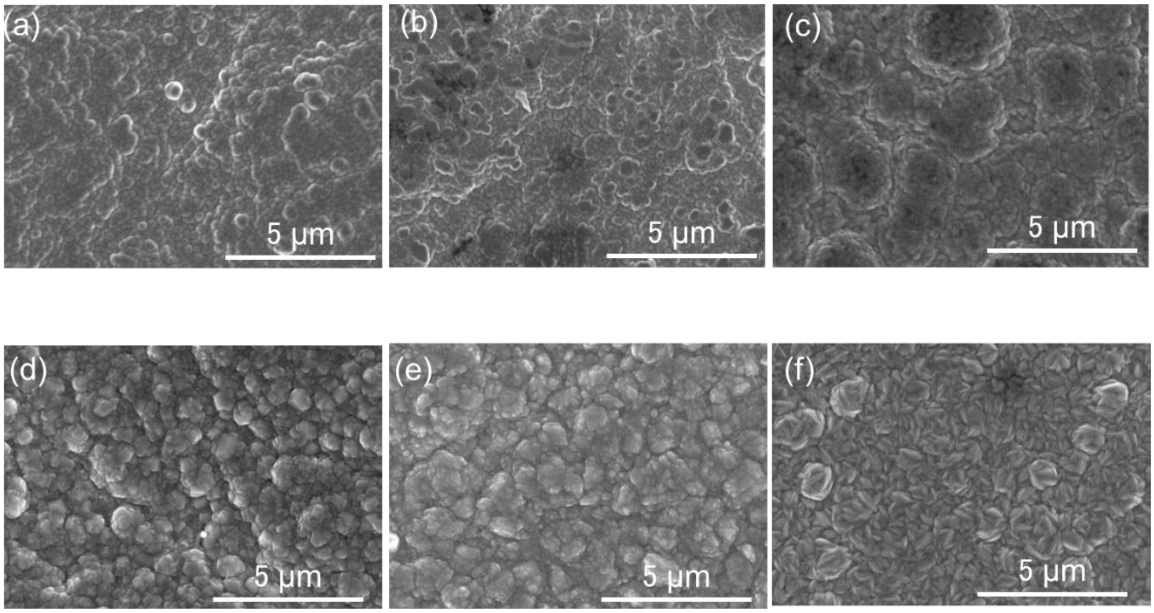

Figure 5.8 SEM images of NiCoP electrodes with different Co precursor concentration: (a) 0 mmol dm^{-3}, (b) 1 mmol dm^{-3}, (c) 5 mmol dm^{-3}, (d) 10 mmol dm^{-3}, (e) 15 mmol dm^{-3}, and (f) 20 mmol dm^{-3}

Table 5.5 Composition of NiCoP electrode with different NiCoP precursor concentration

Co concentration / mmol dm^{-3}	Ni / at%	Co/ at%	P / at%	O /at%
1	68.8	14.2	8.07	8.88
5	61.6	20.9	7.40	10.1
10	47.8	38.6	4.53	9.04
15	43.9	46.5	3.50	6.04
20	43.7	47.6	2.80	5.84

Table 5.5 shows that the composition of Co increases and that of Ni decreases as the Co concentration in the bath increases. The composition of P decreases as the Co concentration increases. On the other hand, the oxygen composition exhibits no trend in the Co concentration range from 1 mmol to 20 mmol dm^{-3}. This could be because the surface of NiCoP may be uniformly oxidized under the ambient condition partially oxidized layer would form before measurement. From these results, the NiCoP electrodes

with different surface morphologies are prepared by the control of Co precursor concentration in the electroless deposition bath.

In order to investigate the effect of surface morphologies on HER performance, electrochemical measurements were carried out. First, to evaluate the effect of the compositional changes on the HER performance, LSV by sweeping from REST to −2500 mV with a scan rate of 50 mV was performed. Figure 5.9 shows the linear sweep voltammograms of different compositional NiCoP electrodes.

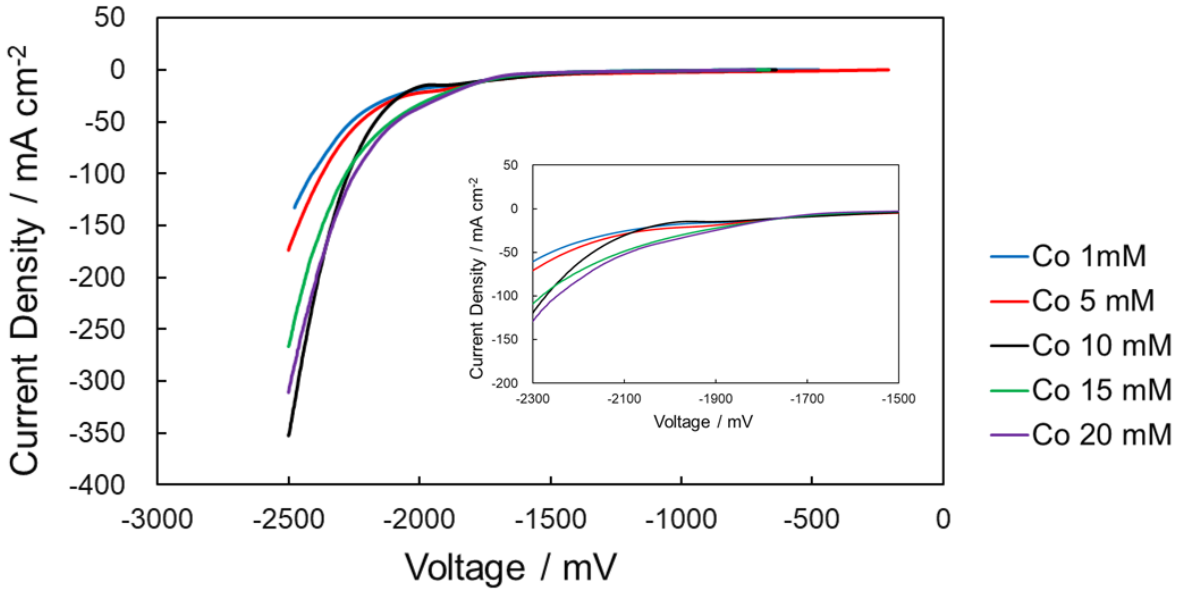

Figure 5.9 Linear sweep voltammograms of different compositional NiCoP electrodes (Inserted figure: Enlarged LSV around −1500 mV to −2300 mV)

From this LSV, the onset voltage around −1900 mV is shifted to the negative values as the Co concentration decreases. As shown in Table 5.5, lower P content affects the higher HER performance from the composition. J. J. Podestra et al. demonstrated that the amorphous alloy of Ni-Co-P with lower P content exhibited higher HER performance under strong alkaline conditions such as 6.0 mol dm^{-3} KOH solution in the alkaline water electrolysis [21]. The tendency of the onset potential is coincident with this trend. Moreover, Ni to Co ratio is another factor that affects the shift of the onset potential. Increasing the ratio of Ni to Co would influence the shift of the onset potential. In Figure

5.9, the current density tends to increase as the Co concentration increases. One possible reason to induce the different HER performance seems to come from the compositional effect. The lower P content improved HER performance as described above. Another possibility is the morphological effect. From Figure 5.8, the morphology of NiCoP changed from particle-like round shape to elongated and angular shape. Carefully focusing on Figure 5.8 (c) and (d), the surface morphology significantly changed to an elongated and angular shape. The compositional change in Table 5.5 also exhibits that the composition of Co rapidly increased when the Co concentration changed from 5 mmol dm^{-3} to 10 mmol dm^{-3}. This tendency indicates that not only the composition but also the surface structures affect HER performance. Further analysis of the effect of morphology is necessary.

To analyze the effect of structural changes on HER, the galvanostatic electrolysis at −500 mA cm^{-2} for 10 min was carried out.

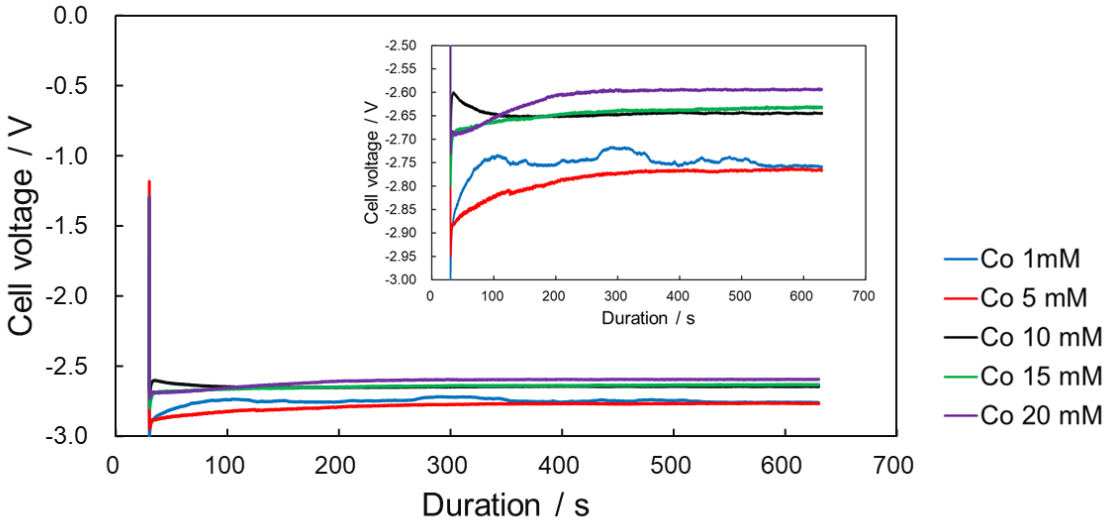

Figure 5.10 Voltage profiles of NiCoP electrodes during the galvanostatic electrolysis at −500 mA cm^{-2} for 10 min (Inserted: Enlarged view around −2.5 V to −3.0 V)

Figure 5.10 shows the voltage profiles of different compositional NiCoP electrodes during the galvanostatic electrolysis at −500 mA cm^{-2}. The trend of the value of the voltage was similar to that observed in LSV in Figure 5.9. The value was reduced when the Co

concentration increased. This trend indicates that elongated and angular morphology influenced HER performance. These structures are assumed to increase the roughness of the electrode surface from the results in 5.3.1, which results in an increase in the active surface area and maintaining the pathway for H_2O and H_2.

To analyze the effect of the morphologies on the resistances of the MEA, the electrochemical impedance spectroscopy (EIS) was measured on the membrane-NiCoP electrode assembly at REST voltage.

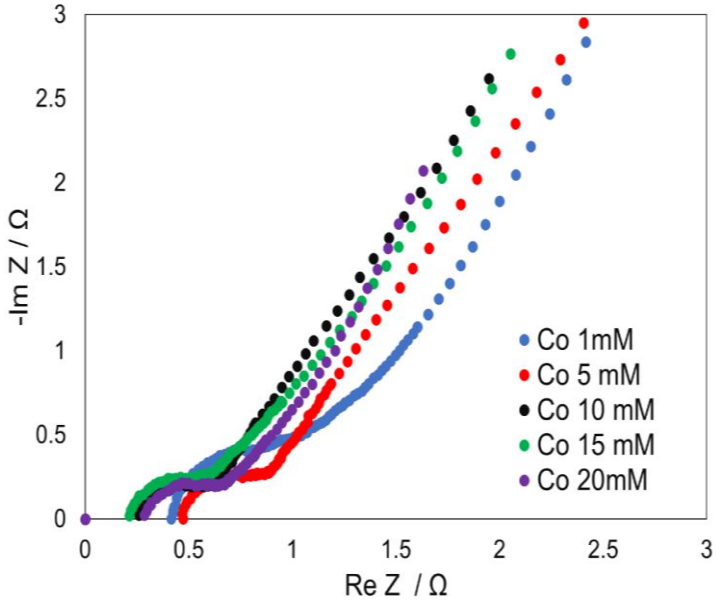

Figure 5.11 Nyquist plots measured for different compositional NiCoP electrodes in AEM electrolysis conditions

Figure 5.11 shows the Nyquist plots obtained at the frequency range from 1 MHz to100 Hz. The Nyquist plots shown in Figure 5.11 exhibited typical capacitive semicircle that corresponded to the information of the resistance of charge transfer between the electrode and electrolyte [22, 23]. At the low-frequency region, the linear response that corresponded to the information of the ion migration into the membrane [24, 25] was confirmed. These Warburg features were confirmed in the previous study as the ion migration inside the polymer membrane [24, 25]. The shape and size of the capacitive

circles could be influenced by the composition of the NiCoP electrodes, possibly because of their different compositions. Thus, it was difficult to quantitatively analyze the obtained result. The point of −Im Z=0 corresponded to the total resistance of the cell and MEA [24]. This information contains the effect of surface structures of NiCoP electrodes on the resistance of the MEA. This behavior was coincident with the trend shown in Figure 5.10. From Figure 5.11, higher Co composition electrodes, the resistance tended to be smaller, suggesting that the elongated and angular shape may influence the interaction to H_2O.

Nevertheless, it is difficult to quantitatively perform the fitting of the obtained Nyquist plots because there is a lack of the understanding of the capacitive semicircles derived from the various compositions of NiCoP and the Warburg impedance that may correspond to ion migration in AEM based on the characteristics of AEM. To compare the resistances derived from the structures of NiCoP electrodes, fitting was conducted with the frequency range from 1 MHz to 100 Hz based on the equivalent circuit shown in Figure 5.12.

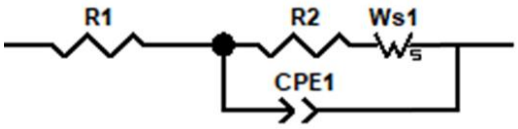

Figure 5.12 Equivalent circuit composed of L1, R1, R2, CPE, and Ws1

CPE was employed instead of the capacitor to consider the different compositions of NiCoP electrodes. Based on this equivalent circuit, the R1, R2, and Ws1 correspond to the internal resistance, charge transfer resistance, and Warburg impedance. To consider the internal resistance, R1 was calculated. The value of R1 in each Co concentration is shown in Table 5.6.

Table 5.6 Value of R1 with different Co concentration

Sample	R1 / Ω
Co 1 mM	0.411
Co 5 mM	0.434
Co 10 mM	0.239
Co 15 mM	0.153
Co 20 mM	0.238

From the calculated results, assuming that the resistance derived from the cell was the same, it could be suggested that the elongated and angular shape influence the resistance of MEA.

From the collective results, the catalytic electrodes on AEM fabricated by the new process successfully function as the cathode of AEM water electrolysis. It is also suggested that the morphological change of prepared electrode influences HER performance during the electrolysis by interaction to H_2O, which could be analogous to surface wettability in Chapters 2 and 3. Considering the optimized structures of the electrode on AEM, a future study may achieve a high-performance electrode fabricated by this electroless deposition process by controlling the porous morphologies with the elongated and angular structures that may be suitable for the supply of H_2O.

5.3.3. Cost analysis of the AEM water electrolysis process fabricated by electroless deposition process

As described in the previous chapters, water electrolysis process is one of the key processes to realize the large-scale energy storage system using hydrogen as the energy carrier. AEM electrolysis process is expected as the next-generation water electrolysis process because of the availability of non-precious material as the catalyst and high efficiency of the process [1,7]. The new fabrication process for the catalytic electrode, as described in chapter 4, and this chapter will contribute to establishing the AEM water electrolysis process. Simultaneously, the cost of the process is one of the

critical issues to widely utilize this process. Therefore, this section describes the material cost analysis of the AEM water electrolysis process using the new electrode fabrication process described in Chapter 4, and a comparison with PEM electrolysis process [10], the most conventional process, was carried out.

Prior to analyzing the cost of AEM water electrolyzers employing the new fabrication process, based on the PEM electrolysis system [26], the process components were assumed, as shown in Figure 5. 13.

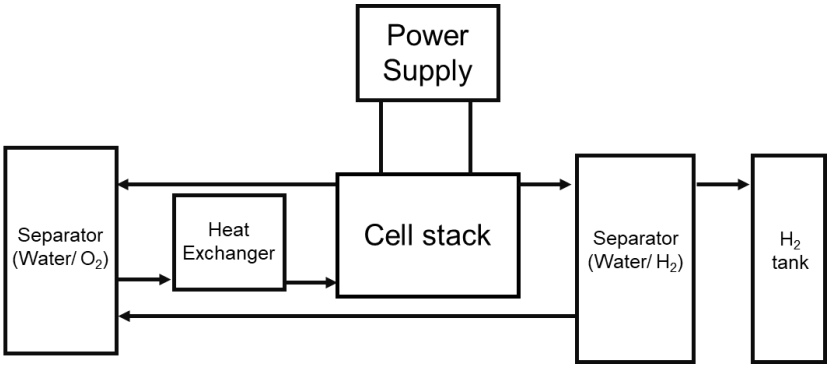

Figure 5.13 Schematic of the electrolysis system

Based on this schematic, the cost analysis was carried out. The electrolysis system was divided into two parts; the cell stack part and the balance-of-plant. The former part mainly consists of the cell stack containing the membrane-electrode assembly. The later part mainly consists of the other systems which are necessary for the process, such as power supply and gas-liquid separator. In this material cost analysis, the size of the system is assumed as the 100 kW electrolyzer system. This cost analysis mainly focused on the cost of the cell stack, including the MEA.

The material cost analysis was carried out when the new fabrication process was carried out. The cost analysis result and the parameters for calculation are shown in Table 5. 6 and 5.7. Prior to analyzing the cost, the cost of the cell stack of the PEM electrolyzer was calculated. The assumption cost of the PEM electrolyzer in 100 kM was 5368.5 USD per cell stack. From Table 5.6, the cost of the catalyst was decreased from 73.6 USD (PEM electrolysis) to 58.3 USD (AEM electrolysis) per the cell stack. Moreover, the

materials of the plate could be changed from Ti or Au coated stainless steel (316L). The cost was decreased from 1048.4 USD (in the case of Au coating) to 260.0 USD. These results indicate that not only the material cost of the cathode catalyst but also the material of the cell itself can be lowered. The material cost per 1kW, one of the indicators for cost analysis of the electrolyzer, was calculated in both PEM and AEM cases. The PEM was 53.69 USD kW^{-1}, and the AEM was 45.64 USD kW^{-1}. These results suggested that NiCoP electrodes fabricated by the electroless deposition process were considered as one of the promising materials for the low-cost AEM electrolyzer system.

Moreover, the effect of this fabrication process on the cost of balance-of-plant was analyzed. From the previous study, the balance-of-plant cost was 76633 USD per 100kW electrolyzer [26]. By applying the AEM electrolyzer, the material of piping and tubing can be changed to conventional stainless-steel materials due to the lower corrosion environment [27]. The cost of piping and tubing occupies approximately 10 % of all balance-of-plant costs. It was indicated that the introduction of the new AEM cathode fabrication process influenced the balance of plant cost by changing the materials of tubes and pipes of the water electrolysis process Shown in Figure 5.13.

Table 5.6 Material cost analysis of the cell stack of AEM electrolyzer

Part	Assumptions	Cost	Cost / USD
Membrane	Anion exchange membrane (AEM)	500 USD/m^2	2440.4
CCM	Cathode : NiCoP, Anode: Pt		58.3
	Cathode Electroless deposition 2.1 mg/cm^2 Anode Pt 0.7 mg/cm^2	Pt: 1500 USD/tr.oz	128.8
PTL	Anode: Ni foam (from Nagamine) Cathode: Carbon paper(TGP-H-90)	Anode: 120USD/m^2 Cathode: 350 USD/m^2	1661.9
Frame	PPS-40GF or PEEK thermoplastics	15.40 USD/kg	15.4
Plates	Stamped Stainless steel 316L 5 mm thick	5 USD	260.0
		Total	4564.8 USD

Table 5. 7 Assumption parameters for the cell stack cost analysis

Parameter name	value	Unit
Stack power	100	kW
Gross system power	110	kW
Average H_2 production rate	15	Nm^3/hr
Average H_2 production rate	80	kg/day
Turndown rate	0-100	%
Operating pressure	1	ber
total plate area	957	cm^2
CCM coated area	748	cm^2
single cell active area	680	cm^2
gross cell inactive area	9	%
single cell amps	1156	A
current density	1.7	A/cm^2
reference voltage	1.7	V
power density	2.89	W/cm^2
cell per system	51	cells
stack per system	1	stacks
cells per stack	51	cells
water pump	5	kW
other parameter loads	7.5	kW
parastic loss	10	kW

The collective analysis data suggested that the introduction of the new fabrication method has an impact on the material cost of the AEM water electrolysis process, and this cost-effectiveness would contribute to the widespread water electrolysis process as the energy storage system using hydrogen as the energy carrier.

5.4. Conclusion

In this chapter, Pt and NiCoP electrodes on AEM were fabricated by electroless deposition process, and the effect of surface morphology on HER was analyzed. To analyze the effect of the fabrication process on HER, HER performance of electrodes Pt electrode and conventional Pt/C electrode was analyzed. The result indicated that electroless Pt electrode exhibited higher durability by suppressing the degradation of Pt catalyst derived from the dissolution of the carbon support. In addition, The elongated structures of the electrode could contribute to stronger interaction of H_2O similar to hydrophobicity. NiCoP electrodes with different surface morphology were also fabricated prior to analyzing the effect of surface structures. The electrochemical measurements indicated that a higher rough surface with the elongated structures would improve HER performance. From these collective results, it was suggested that control the surface structures to improve the interaction to H_2O will enhance the HER performance in AEM water electrolysis process.

References

[1] I. Vincent, D. Bessarabov, Low cost hydrogen production by anion exchange membrane electrolysis: A review, *Renewable Sustainable Energy Rev.* **81** (2018) 1690.

[2] S. Marini, P. Salvi, P. Nelli, R. Pesenti, M. Villa, M. Berrettoni, G. Zangari, Y. Kiros, Advanced alkaline water electrolysis, *Electrochim. Acta* **82** (2012) 384.

[3] C. C. Pavel, F. Cecconi, C. Emiliani, S. Santiccioli, A. Scaffidi, S. Catanorchi, M. Comotti, Highly Efficient Platinum Group Metal Free Based Membrane-Electrode Assembly for Anion Exchange Membrane Water Electrolysis, *Angew. Chem. Int. Ed.* **53** (2014) 1378.

[4] L. Xiao, S. Zhang, J. Pan, C. X. Yang, M. L. He, L. Zhuang, J. T. Lu, First implementation of alkaline polymer electrolyte water electrolysis working only with pure water, *Energy Environ. Sci.* **5** (2012) 7869.

[5] Y. Leng, G. Chen, A. J. Mendoza, T. B. Tighe, M. A. Hickner, C. Y. Wang, Solid-state water electrolysis with an alkaline membrane, *J. Am. Chem. Soc.* **134** (2012) 9054.

[6] B. K. Kakati, D. Sathiyamoorthy, A. Verma, Electrochemical and mechanical behavior of carbon composite bipolar plate for fuel cell, *Int. J. Hydrogen Energy* **35** (2011) 4185.

[7] H.A. Miller, K. Bouzek, J. Hnat, S. Loos, C.I. Bernäcker, T. Weißgärber, L. Röntzsch, J. Meier-Haack, Green hydrogen from anion exchange membrane water electrolysis: A review of recent developments in critical materials and operating conditions, *Sustain. Energy Fuels.* **4** (2020) 2114.

[8] H. Ito, N. Miyazaki, S. Sugiyama, M. Ishida, Y. Nakamura, S. Iwasaki, Y. Hasegawa, A. Nakano, Investigation on electrode configurations for anion exchange membrane electrolysis, *J. Appl. Electrochem.* **48** (2018) 305.

[9] X. Wu and K. Scott, A Li-doped Co3O4 oxygen evolution catalyst for non-precious metal alkaline anion exchange membrane water electrolyzers, *Int. J. Hydrogen Energy* **38** (2013) 3123.

[10] M. Carmo, D.L. Fritz, J. Mergel, D. Stolten, A comprehensive review on PEM water electrolysis, *Int. J. Hydrogen Energy* **38** (2013) 4901.

[11] A. Zadick, L. Dubau, N. Sergent, G. Berthome, M. Chatenet, Huge Instability of Pt/C in Alkaline Medium, *ACS Catal.* **5** (2015) 4819.

[12] V. S. Sumi, M. A. Sha, S. R. Arunima, S. M. A. Shibli, Development of a novel method of NiCoP alloy coating for electrocatalytic hydrogen evolution reaction in alkaline media, *Electrochim. Acta* **303** (2019) 67.

[13] Y. Wang, G. Li, S. Wu, Y. Wei, W. Meng, Y. Xie, Y. Cui, X. Lian, Y. Chen, X. Zhang, Hydrogen generation from alkaline NaBH4 solution using nanostructured Co–Ni–P catalysts, *Int. J. Hydrogen Energy* **42** (2017) 16529.

[14] JP Patent 2018-3108.

[15] T. Homma, Y. Sezai, T. Osaka, Y. Maeda, D. M. Donnet, Compositional inhomogeneity in electroless-deposited CoNiP films studied by spin-echo 59Co nuclear magnetic resonance, *J. Magn. Magn. Mater.* **173** (1997) 314.

[16] K. N. Srinivasan, T. Selvaganapathy, R. Meenakshi, S. John, Electroless deposition of nickel–cobalt–phosphorus nanoalloy, *Surf. Eng.* **27** (2011) 65.

[17] H. Ito, N. Kawaguchi, S. Someya, T. Munakata, Pressurized operation of anion exchange membrane water electrolysis, *Electrochim. Acta*, **297** (2019) 188.

[18] Q. Zhenga, F. Dierrea, V. Corregidorbc, J. Croccoa, H. Bensalaha, J. L. Plazaa, E. Alvesbc, E. Diegueza, Electroless deposition of Au, Pt, or Ru metallic layers on CdZnTe, *Thin Solid Films* **525** (2012) 56.

[19] C. Lafforgue, M. Chatenet, L. Dubau, D. R. Dekel, Accelerated Stress Test of Pt/C Nanoparticles in an Interface with an Anion-Exchange Membrane -An Identical-Location Transmission Electron, Microscopy Study, *ACS Catal.* **8** (2018) 1278.

[20] J. R. Varcoe, P. Atanassov, D. R. Dekel, A. M. Herring, M. A. Hickner, P. A. Kohl, A. R. Kucernak, W. E. Mustain, K. Nijmeijer, K. Scott, T. Xu, L. Zhuang, Anion-exchange membranes in electrochemical energy systems, *Energy Environ. Sci.* **7** (2014) 3135.

[21] Y-H. Cho, H-S. Park, Y-H. Cho, D-S. Jung, H-Y. Park, Y. E. Sung, Effect of platinum amount in carbon supported platinum catalyst on performance of polymer electrolyte membrane fuel cell, *J. Power Sources* **172**(1) (2007) 89.

[21] J. J. Podestra, R. C. V. Piatti, A. J. Ariva, P. Ekdunge, K. Juttner, G. Kreysa, The behaviour of Ni-Co-P base amorphous alloys for water electrolysis in strongly alkaline solutions prepared through electroless deposition, *Int. J. Hydrogen Energy* **17** (1992) 9.

[22] M. Huang, F. Li, Y. X. Zhanga, B. Li, X. Gao, Hierarchical NiO nanoflake coated CuO flower core-shell nanostructures for supercapacitor, *Ceram. Int.* **40** (2014) 5533.

[23] H. Liu, P He, S. Wang, J. Gao, L. Zhou, C. Li, Y. Zhang, D. Yang, M. He, L. Jia, F. Dong, H. Liu, Facile one-step fabrication of bimetallic CoNiP hollow nanospheres anchored on reduced graphene oxide as highly efficient electrocatalyst for hydrogen evolution reaction, *Int. J. Hydrogen Energy* **44** (2019) 24140.

[24] J.C. Garcia-Navarro, M. Schulze, K.A. Friedrich, Measuring and modeling mass transport losses in proton exchange membrane water electrolyzers using electrochemical impedance spectroscopy, *J. Power Sources*, **431** (2019) 189.

[25] S. Siracusano, C. Oldani, M. A. Navarra, S. Tonella, L. Mazzapioda, N. Briguglio, A. S. Aricò, Chemically stabilised extruded and recast short side chain Aquivion® proton exchange membranes for high current density operation in water electrolysis, *J. Membr. Sci.*, **578** (2019) 136.

[26] A. Mayyas, M. Ruth, B. Pivovar, G. Bender, K. Wipke, A. Mayyas, M. Ruth, B. Pivovar, G. Bender, K. Wipke, Manufacturing Cost Analysis for Proton Exchange Membrane Water Electrolyzers Manufacturing Cost Analysis for Proton Exchange Membrane Water Electrolyzers, *Natl. Renew. Energy Lab.* (2019) 65.

[27] M. Wei, T. Lipman, A. Mayyas, J. Chien, S. H. Chan, D. Gosselin, H. Breunig, M. Stadler, T. McKone, P. Beattie, P. Chong, W. G. Colella, B. D. James, A Total Cost of Ownership Model for Low Temperature PEM Fuel Cells in Combined Heat and Power and Backup Power Applications, *LBNL Technical Report*, (2014) LBNL-6772E.

Chapter 6:

General Conclusion

Hydrogen production by water electrolysis using renewable energy is of extreme importance for utilizing hydrogen as an energy carrier. Especially alkaline and (AEM) water electrolysis have been paid attention to as the large-scale process with low-cost and the small-scale high-performance process, respectively. Despite the potential of these processes in hydrogen production, their applications are limited. The main issue lies in the lower efficiency of the entire process. Focusing on the catalytic electrode for HER, a crucial reaction for hydrogen generation, highly efficient electrodes in both alkaline and AEM water electrolysis processes are required. One of the main factors for improving the efficiency of the electrode is the surface structure of the electrodes. The objective of this thesis was to propose a strategy for highly efficient surface structures of the electrode for both alkaline and AEM water electrolysis processes.

In the case of the electrodes in the alkaline electrolysis process, many researchers have reported that the bubble behavior on the electrode surface influences the HER performance, and the surface nano/microstructures govern the bubble behavior. However, the effect of the surface nano/microstructures on the bubble behavior is still unclear. Thus, in Chapters 2 and 3, the effect of surface microstructures on bubble behavior was analyzed using Ni micropatterned electrodes and Pt microfacet electrodes as surface-modified electrodes.

In the case of electrodes in the AEM water electrolysis process, the control of surface structures by the conventional fabrication process is challenging. In Chapter 4, a new fabrication process that can modify the surface structures was investigated using the electroless deposition process. In Chapter 5, the effects of the electrodes fabricated by the new process and the surface structures on the HER performance were analyzed.

In this chapter, the results obtained in this thesis are briefly summarized, and the possibility of highly efficient catalytic electrodes for the HER in alkaline and AEM water electrolysis processes is discussed.

In Chapter 2, the bubble nucleation and growth on the electrode surface were analyzed using Ni micropatterned electrodes in alkaline water electrolysis, and the effects of the microstructures and surface wettability modified by these structures on the bubble nucleation and growth were elucidated. The Ni micropatterned electrodes were selected

as the model electrode surface because they can systematically control their own structures and wettability.

From the *in situ* bubble behavior observations on the electrode surface under different conditions, the effect of the Ni micropatterned structures (in terms of parameters such as diameter and height) on bubble behavior during HER was investigated. At the microscopic level, lower surface wettability enhanced bubble growth on the electrode surface because of the stabilizing effect derived from the larger interface between bubbles and electrodes. Moreover, the height and intervals of microstructures strongly influenced bubble nucleation; bubble nucleation preferentially occurred on the sidewall region in the intervals, whose structures were similar to defect structures. These structures may behave as nucleation sites for bubbles.

In Chapter 3, the effect of introducing a well-defined region on bubble nucleation and growth was investigated by *in situ* bubble behavior analysis. The well-defined surface, such as the microfacet, is one of the critical factors that consist of the surface characteristics of the single microdot. For the analysis of bubble behavior, Pt (111) microfacet electrodes were employed as the model electrodes, and the bubble behavior on the (111) microfacet was intensively analyzed.

From the *in situ* observation, bubble nucleation was suppressed on the (111) microfacet under smaller overpotentials. This result indicated that both low HER activity on the (111) surface and smooth surface morphology of the microfacet influenced bubble nucleation on the microfacet. Moreover, bubble generation preferentially proceeded on the edge rather than the center of the microfacet, indicating that the step-edge sites behaved as bubble nucleation sites because of the introduction of the microfacet on the electrode surface. This introduction of the microfacet suppressed the overpotential increase during electrolysis, suggesting that the existence of the step-edge as the bubble nucleation sites due to microfacet introduction could inhibit the site's occupation of evolved bubbles, leading to the suppression of the overpotential increase.

From the discussion in Chapters 2 and 3, the guideline for the suggested efficient surface microstructures is shown in Figure 6.1.

For early bubble detachment from the surface, the decrease in the area of the interface between the bubble and microstructures is important to destabilize bubble adsorption on the surface. For the bubble nucleation sites, the defect-like structures such as the sidewall of the microdot in Figure 6.1 facilitate early bubble formation and detachment, which suppresses the occupation of the reaction sites by bubbles.

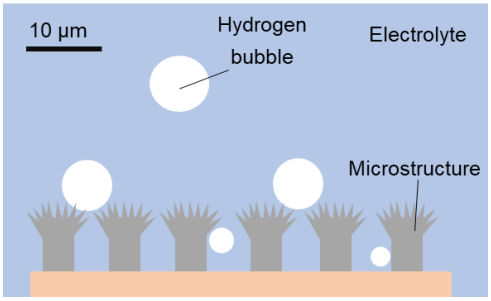

Figure 6.1 Bubble behavior on the microstructure surface.

In Chapter 4, a new direct fabrication process for the electrode used in AEM water electrolysis by utilizing an electroless deposition process is proposed.

The catalytic electrode was directly electrolessly deposited on the AEM surface without using any ionomers, which was achieved by controlling the catalyzation process that introduced the catalyst particle on the AEM surface. Compared with the conventional process using Sn and Pd solutions (i.e., the sensitizing–activation process), the subsequent electroless deposition proceeded on the AEM when AEM was immersed into the Pd solution as the catalyzing process. DFT analysis indicated that the SnO_3^{2-} species formed during the catalyzation process inhibited the electroless deposition process because of the stronger interaction with AEM by suppressing the formation of Pd catalyst particles on AEM. SEM observation also confirmed that the catalytic electrode was uniformly fabricated on AEM by this electroless deposition process. To the best of our knowledge, this is the first report that achieved the fabrication of the electrode directly on an AEM without using any ionomers.

In Chapter 5, to analyze the performance of the catalytic electrodes fabricated by

the electroless deposition process described in Chapter 4 and the effect of surface structures on HER performance, electroless Pt catalytic electrodes, one of the benchmark electrodes, and NiCoP catalytic electrodes were fabricated for the analyses.

Electrochemical measurements revealed that the electroless Pt electrode exhibited higher durability than the conventional Pt/C catalyst prepared by spraying, indicating that the degradation of Pt/C derived from the dissolution of the carbon support was suppressed on the electroless-deposited Pt electrodes because of the lack of carbon-based materials. Moreover, the NiCoP electrodes with different surface morphologies were successfully fabricated by this electroless deposition process. The electrochemical measurements indicated that a larger rough surface would improve the HER because of the increase in the affinity to H_2O molecules, which might be similar to the effect of wettability.

From the results in Chapters 4 and 5, the importance of improving the HER efficiency of the electrode in the AEM process is discussed as follows.

The electrode fabricated by the proposed electroless deposition method exhibits improved durability for water electrolysis because of the strong adhesion to the AEM surface in the absence of an ionomer. The surface structures that supply the pathway for H_2O and H_2, such as the elongated microstructures, are the key factor for HER performance.

This thesis focused on the effect of surface structures on HER performance in alkaline and AEM water electrolysis processes and the guidelines for designing highly efficient surface structures on the basis of the analyses of the effect of surface structures on the interfacial processes. The guidelines suggest that the efficiency of the alkaline water electrolysis process could be further improved by suppressing the bubble effect, thereby becoming acceptable for other processes that involve gas bubble evolution, such as the OER. The guideline for the electrode in AEM process could contribute to the development of new catalytic electrodes with improved durability and surface structures. Both improved processes for these analyses could enable a wider utilization of H_2 produced using renewable energy.

List of Achievements

1. Original Articles

"Direct formation of metal layer on anion exchange membrane using electroless deposition process"
Tatsuki Fujimura, Masahiro Kunimoto, Yashiro Fukunaka, Hiroshi Ito, Takayuki Homma
Electrochemistry, in press
(https://doi.org/10.5796/electrochemistry.20-00158)

"Analysis of the hydrogen evolution reaction at Ni micro-patterned electrodes"
Tatsuki Fujimura, Masahiro Kunimoto, Yasuhiro Fukunaka, Takayuki Homma
Electrochimica Acta, **368***,* 137678 (2021).
(https://doi.org/10.1016/j.electacta.2020.137678)

"Analysis of the effect of surface wettability on hydrogen evolution reaction in water electrolysis using micro-patterned electrodes"
Tatsuki Fujimura, Wakana Hikima, Yasuhiro Fukunaka, Takayuki Homma
Electrochemistry Communications, **101**, 43-46 (2019).
(https://doi.org/10.1016/j.elecom.2019.02.018)

2. Presentations

[International Conference]

"The Effect of Surface Nano and Microstructures on Hydrogen Gas Evolution Behavior on Ni Patterned Electrodes"
Tatsuki Fujimura, Masahiro Kunimoto, Yasuhiro Fukunaka, Takayuki Homma
Pacific Rim Meeting on Electrochemical and Solid-State Science 2020 (PRiME 2020), Hawaii, U. S. A., 2020 October.

"Hydrogen Gas Bubble Behaviors on Ni Micro-Patterned Electrode during Alkaline Water Electrolysis"
Tatsuki Fujimura, Wakana Hikima, Yasuhiro Fukunaka, Takayuki Homma
8th World Hydrogen Technologies Convention 2019 (WHTC2019), Tokyo, Japan, 2019 June.

"Analysis of Hydrogen Gas Evolution Phenomena on Micro-Patterned Ni Electrode during Alkaline Water Electrolysis"
Tatsuki Fujimura, Wakana Hikima, Yasuhiro Fukunaka, Takayuki Homma
6th DGIST-WASEDA Workshop on Electrochemistry, Degue, Korea, 2018 November.

"Analysis of Hydrogen Gas Evolution Phenomena on Micro-Patterned Ni Electrode during Alkaline Water Electrolysis",
Tatsuki Fujimura, Wakana Hikima, Yasuhiro Fukunaka, Takayuki Homma
The 12th International Symposium on Electrochemical Micro & Nano System Technologies (EMNT2018), Milano, Italy, 2018 August.

[Domestic Conferences]

"Fabrication of Micro-Patterned Electrodes for Analysis of Effect of Electrode Surface on Hydrogen Evolution Reaction"
Shogo Sakuma, Wakana Hikima, Tatsuki Fujimura, Yasuhiro Fukunaka, Takayuki Homma
The 87th ECSJ Spring Meeting, Nagoya, Japan, 2020 March

"Analysis of Hydrogen Bubble Evolution during Alkaline Water Electrolysis using Micro Patterned Electrode"
Tatsuki Fujimura, Wakana Hikima, Masahiro Kunimoto, Yasuhiro Fukunaka, Takayuki Homma
The 43rd Meeting of the Electrolytic Science and Technology, Kyoto Japan, 2019 November.

"Analysis of Effect of Surface Wettability on Hydrogen Evolution Reaction Using Micro-Patterned Electrodes"
Wakana Hikima, Tatsuki Fujimura, Yasuhiro Fukunaka, Takayuki Homma
The 85th ECSJ Meeting, Tokyo, Japan, 2018 March.

"Analysis and Fabrication of Catalytic Electrodes for Water Electrolysis Process based on Bubble Behaviors"
Tatsuki Fujimura, Wakana Hikima, Yasuhiro Fukunaka, Takayuki Homma
7th CSJ Chemical Festa, Tokyo, Japan, 2017 October.

3. Others

[Academic Papers]

"Experimental Measurement of Overpotential Sources during Anodic Gas Evolution in Aqueous and Molten Salt Systems"
Brian Chmielowiec, Tatsuki Fujimura, Tomohiro Otani, Keigo Aoyama, Toshiyuki Nohira, Takayuki Homma, Yasuhiro Fukunaka, Antoine Allanore
Journal of the Electrochemical Society, **166**(10), E323-329 (2019).

"Analysis of Cathodic Reaction Process of $SiCl_4$ during Si Electrodeposition Process in Ionic Liquids"
Yasuhiro Tsuyuki, Tatsuki Fujimura, Masahiro Kunimoto, Yasuhiro Fukunaka, Piero Pianetta, Takayuki Homma
Journal of the Electrochemical Society, **164**(14), D994-D998 (2017),

[International Conferences]

"Electrodeposition of Si Thin Films in Ionic Liquid with Growth Control from Initial Stages",
Hidenori Takai, Yasuhiro Tsuyuki, Tatsuki Fujimura, Masahiro Kunimoto, Yasuhiro Fukunaka, Piero Pianetta, Takayuki Homma
5th DGIST-WASEDA Workshop on Electrochemistry, Tokyo, Japan, 2018 December.

"Electrodeposition of Si Thin Films in Ionic Liquid with Growth Control from Initial Stages",
Hidenori Takai, Yasuhiro Tsuyuki, Tatsuki Fujimura, Masahiro Kunimoto, Yasuhiro Fukunaka, Piero Pianetta, Takayuki Homma
The 27th Photovoltaic Science and Engineering Conference, Shiga, Japan, 2017 November.

"Connecting Anodic Gas Evolution in Aqueous and High Temperature Molten Electrolyte Systems Via the Current Interrupt Technique"
Brian Chmielowiec, Tatsuki Fujimura, Tomohiro Otani, Keigo Aoyama, Toshiyuki Nohira, Takayuki Homma, Yasuhiro Fukunaka, Antoine Allanore
68th International Meeting of the International Society of Electrochemistry, Rhode Island, U. S. A., 2017 September.

"Theoretical Analysis of $SiCl_4$ Reaction Mechanism for Si Electrodeposition Process in TMHA-TFSI as Ionic Liquids"
Tatsuki Fujimura, Yasuhiro Tsuyuki, Masahiro Kunimoto, Yasuhiro Fukunaka, Takayuki Homma
231st ECS Meeting, New Orleans, U. S. A., 2017 May.

"Analysis of Cathodic Reaction Process of $SiCl_4$ in Ionic Liquids"
Yasuhiro Tsuyuki, Tatsuki Fujimura, Masahiro Kunimoto, Yasuhiro Fukunaka, Piero Pianetta, Takayuki Homma
231st ECS Meeting, 2017 May, New Orleans, U. S. A.,

"Theoretical Analysis of $SiCl_4$ Reaction Mechanism for Si Electrodeposition Process in Ionic Liquids"
Tatsuki Fujimura Masahiro Kunimoto, Takayuki Homma
Nucleation & Growth Research Conference 2016, Kyoto, Japan, 2016 September.

"Reduction Mechanism Analysis of $SiCl_4$ during Si Electrodeposition in Ionic Liquids"
Yasuhiro Tsuyuki, Tatsuki Fujimura, Masahiro Kunimoto, Yasuhiro Fukunaka, Piero Pianetta, Takayuki Homma
Nucleation and Growth Research Conference 2016, Kyoto, Japan, 2016 September

4. Awards

CSJ Poster Presentation Award 2017 for Excellent Research, 7th CSJ Chemical Festa, 2017 November.

Acknowledgments

First of all, I would like to express my appreciation to my thesis supervisor Professor Dr. Takayuki Homma. Since I joined the laboratory in 2015, he has been supporting my laboratory activity. He taught me a lot about not only how to consider and organize scientific researches and how to write scientific findings, but also the attitude with joy and enthusiasm for the research and electrochemistry. I would like to appreciate his thoughtful instructions and warm supports that help me to grow as a researcher. Moreover, he gave me precious opportunities such as research activity abroad, collaborative research, and so on. From these experiences, I gained fundamental skills to become a researcher or an engineer in the global world.

I would also like to express my appreciation to Professor Dr. Kenich Oyaizu, Professor Dr. Toshiyuki Momma, Professor Dr. Kenji Miyataka (Yamanashi University), and Dr. Kenich Uemura (NIPPON STEEL Chemical & Material CO., LTD.) for my thesis review. Their comments and suggestions are very helpful for a deeper understanding of my thesis work.

I also want to thank Professor Dr. Yasuhiro Fukunaka and Professor Dr. Mikiko Saito for their advice on the thesis and encouragement toward the doctor course. Their insightful suggestions always help me to proceed with the research.

Professor Dr. Masahiro Kunimoto always gives me valuable advice and suggestion from a wider viewpoint. Discussion with him gave me a deeper insight into the thesis work and an enlarged viewpoint of chemistry.

In the work of fabrication Pt microfacet electrodes and their analyses, I would like to appreciate Professor Dr. Daniel A. Scherson at Case Western Reserve University and colleagues in his lab for their kind helps and valuable suggestions. Without their helps, the research in chapter 3 would not have been possible. Especially, I would like to thank Professor Dr. Daniel Scherson for his kind acceptance and preparation of my research internship at Case Western Reserve Univ.

The detailed discussion of the performance of AEM water electrolysis process in chapter 4 and 5 would have been impossible without valuable suggestions and kind help from the group of Professor Dr. Hiroshi Ito at the National Institute of Advanced Industrial Science and Technology (AIST), and Professor Dr. Mikito Ueda and Professor Dr. Hisayoshi Matsushima at Hokkaido University. I would also like to express my

sincere appreciation for their collaborations and valuable advice on my thesis research.

I would like to express my appreciation to my collaborators and colleagues for spending my time in the laboratory enjoyable. I would like to thank the senior and junior colleagues in the doctoral course; Dr. Siggi Wodarz, Dr. Yasuhiro Tsuyuki, Dr. Tomohiro Otani, Mr. Yelchur V. Akash, Mr. Yusuke Onabuta, Ms. Tanyanyu Wang, and Mr. Kohei Ide. Their joy and enthusiasm for research and kind suggestions for my thesis research encouraged me in tough experiences in the lab. I am also grateful to Ms. Wakana Hikima, Mr. Shintaro Gonda, Mr. Yukihiro Okamura, Mr. Shogo Sakuma, Mr. Shunya Kihira, and Ms. Ayaka Hirai for collaborative work and engagement in the research relating to water electrolysis process. Without their contributions, this thesis work has not been completed.

I also would like to express my thank to Dr. Brian Chmielowiec (Massachusetts Institute of Technology) for kind suggestions for the research and valuable opportunities for the interaction with him. During his stay in Waseda University, his joy and enthusiasm for the research and kindness for daily communications gave me lots of things necessary for the researcher in the world.

Lastly, I would like to express my appreciation to my parents and my sister for their warm supports during the 5-years doctoral course. Without their understandings and patient, this thesis would be not achieved.

February, 2021
Tatsuki Fujimura